uOttawa

L'Université canadienne
Canada's university

FACULTÉ DES ÉTUDES SUPÉRIEURES ET POSTOCTORALES

u Ottawa

L'Université canadienne
Canada's university

FACULTY OF GRADUATE AND POSDOCTORAL STUDIES

Catherine Grgicak

AUTEUR DE LA THÈSE / AUTHOR OF THESIS

Ph.D. (Chemistry)

GRADE / DEGREE

Department of Chemistry

FACULTÉ, ÉCOLE, DÉPARTEMENT / FACULTY, SCHOOL, DEPARTMENT

Anodes for solid oxide fuel cell (SOFC) systems operating in multiple fuel environments: Effects of microstructure and composition

TITRE DE LA THÈSE / TITLE OF THESIS

Javier Giorgi

DIRECTEUR (DIRECTRICE) DE LA THÈSE / THESIS SUPERVISOR

CO-DIRECTEUR (CO-DIRECTRICE) DE LA THÈSE / THESIS CO-SUPERVISOR

EXAMINATEURS (EXAMINATRICES) DE LA THÈSE / THESIS EXAMINERS

Robert Burke

Kunal Karan

Christian Detellier

Paul Mayer

Gary W. Slater

Le Doyen de la Faculté des études supérieures et postdoctorales / Dean of the Faculty of Graduate and Postdoctoral Studies

Anodes for solid oxide fuel cell (SOFC) systems operating in multiple fuel environments: Effects of microstructure and composition

Catherine Grgicak

Thesis submitted to the
Faculty of Graduate and Postdoctoral Studies
In partial fulfillment of the requirements
for the PhD degree in the Ottawa-Carleton Chemistry Institute

Department of Chemistry
Faculty of Science
University of Ottawa

Your file Votre référence
ISBN: 978-0-494-49352-6
Our file Notre référence
ISBN: 978-0-494-49352-6

Abstract

This work examined several cermet materials as possible anode materials for solid oxide fuel cell (SOFC) systems operating in multiple fuel environments. In particular, these materials consisted of two phase M-YSZ (M=Ni, Cu or Co, YSZ= yttria stabilized zirconia) cermets synthesized via the gel-precipitation method. Relations between synthesis conditions and cermet structure/performance dominated the first section of this work. SOFC anode performance was correlated back to original synthesis conditions, whereby d_M/d_{YSZ} was controlled via the production of a crystalline intermediate.

Electrochemical characterization of Ni- and Co-YSZ anodes in H_2 and H_2S/H_2 fuels was performed and each arc observed in the impedance curves was ascribed to a specific process. The high- and mid-frequency arcs were related to transport and charge transfer processes respectively. Non-traditional relationships between inverse Tafel (Lefat) slopes and temperature were observed. This resulted in a change in charge transfer coefficients with respect to temperature. By evaluating this dependence, a charge transfer coefficient of 1.5 for hydrogen oxidation on Ni-, Co- and NiS- anodes was determined. CoS- anodes resulted in a charge transfer coefficient of 0.2.

NiS- and CoS- anodes were stable in sour gas environments and selective towards the electrochemical oxidation of H_2 over H_2S as suggested by open circuit voltage and mass spectrometry.

Cell performances of and CoS- anodes in sour gas environments were stable over a 6 day period and showed no signs of deterioration. However, H_2S was required in the fuel stream to maintain optimal performance of these anodes. Once H_2S was removed, the CoS- anodes reverted to Co-YSZ. For CoS- based anodes, optimum cell performance was maintained at a H_2S content >1v/v%.

Investigations of bimetallic NiCu- and NiCo- anodes were also performed. The addition of Cu to Ni- based anodes resulted in larger metal particle sizes and decreased anode activity for hydrogen oxidation. Small additions of Co to Ni- based anodes showed a marked improvement in hydrogen oxidation activity. The bimetallic anodes were also tested in H_2S/CH_4 mixtures and showed good activity for all anodes tested over a 15 hour period.

Table of Contents

List of Figures

List of Tables

List of Abbreviations and Symbols

A- pre-exponential factor

AC - alternating current

ATR-FTIR – attenuated total reflectance fourier transform infrared spectroscopy

α_a - anodic charge transfer coefficient

α_c - cathodic charge transfer coefficient

Abs - Absorbance

b^{-1} - inverse Tafel slope or Lefat slope

B - BET constant

BET - Brauner-Emmett-Teller model used to calculate surface area

β - barrier symmetry factor

C - capacitance

CE – counter electrode

CPE – constant phase element

CV- cyclic voltammetry

$C_{i\vartheta}$ - concentration of all species at the surface

d – particle size

D - diffusion coefficient

DC - direct current

D_B and D_V - diffusion coefficients for grain-boundary and volume diffusion, respectively

$\frac{\Delta d}{d}$ - microstrain

δ - diffusion layer thickness

$\widetilde{E}$ - oscillating voltage

$\overline{E}$ - amplitude of voltage

E_a - activation energy

E^o - standard potential

E^o_{FC} - open circuit potential at conditions other than standard state

EDX – energy dispersive x-ray spectroscopy

ε - molar absorbtivity

ε_H - heating efficiency

ε_i - current efficiency

ε_T - theoretical efficiency at temperature T

ε_V - voltage efficiency

ξ - statistical thickness of an adsorbed layer

F - Faraday constant - 96485 C/mol

δ - grain boundary thickness

G - mean grain size

$\Delta G^{o\neq}$ - free energy of activation at OCV

$\Delta_r G^o$ - standard Gibbs energy of reaction

$\Delta G_\eta^{\neq}$ - free energy of activation at $\eta \neq 0$

$\Delta_r G_T^o$ - Gibbs energy of reaction at temperature T

γ - surface area

γ_f - number of electrons transferred follwing rate-determining step

γ_p - number of electrons transferred during rate determining step

f - void fraction

$\Delta_r H_T^o$ - enthalpy of reaction at temperature T

i - current

$\widetilde{i}$ - oscillating current

$\vec{i}$ - current in forward direction

$\overleftarrow{i}$ - current in reverse direction

i_f - Faradaic current

i_L - limiting current

i_o - exchange current density

iR - potential drop

I_i - calculated profile intensity of a data point in XRD k_o - rate constant

j - imaginary unit

K - Boltzmann constant

$K_C = \frac{k_{ca}}{k_{cd}}$ - ratio of adsorption and desorption rate constants

κ - effective conductivity

κ_c - bulk conductivity

L – length

LSV – linear sweep voltammetry

λ – wavelength

n - number of electrons

η - overpotential

OCV - open circuit voltage

Ω - atomic volume

P/P_o - partial pressure of adsorbate

ϕ - phase shift

q - charge

r - Lorentzian component (mixing/tailing factor) in the pseudo-Voigt

R - ideal gas constant - 8.3145 J/K•mol

R_{ct} - charge transfer resistance

R_p - polarization resistance

R_s - series resistance

SEM – scanning electron microscopy

SOFC - solid oxide fuel cell

[S] – concentration

S - skewness

$\Delta 2\theta = 2\theta_i - 2\theta_p$

$2\theta_p$ - peak position

$2\theta_i$ - calculated peak position

θ_i - surface coverage of species i

t - crystallite size

t - time

T - temperature

Γ_B and Γ_V - scaling factors for volume and grain-boundary diffusion, respectively

UV-VIS – ultra violet – visible

V - volume of gas adsorbed

V_M - volume of gas adsorbed constituting a monolayer of surface coverage

ν - number of times the rate-determining step occurs

WE – working electrode

$\omega=2\pi f$ - angular frequency

$W_{1/2}$ - the width at half height

XRD – x-ray diffraction

XRF – x-ray fluorescence

X_c - capacitive reactance

YSZ – yttria stabilized zirconia

Y_o – admittance

Z – impedance

z_{rds} - number of electrons transferred during rate determining step

Publications

Peer reviewed articles have been published as a result of my work during these past few years. Some of the work described in the present thesis has already been published or submitted for publication. Most of them are described in this thesis, but I have also participated in other aspects of research within the group.

C.M. Grgicak, R.G. Green, J.B. Giorgi. *SOFC Anodes for Direct Oxidation of Hydrogen and Methane Fuels Containing H_2S.* J. Power Sources., in preparation.

This article summarizes the results found in Chapters 5 and 6. It emphasizes the performance aspect of each anode in H_2, CH_4, H_2S/H_2 and H_2S/CH_4 environments.

C.M. Grgicak, J.B. Giorgi. *Improvement of SOFC Anode Performance via Sulfidation of Metal (Ni, Co) Yttria Stabilized Zirconia electrocatalysts: A Kinetic Analysis.* J. Phys. Chem. C., submitted.

This paper is a combination of results found in Chapters 4 and 5. It describes the improvement in SOFC anode performance once metal sulfidation is complete and the variations in kinetic parameters (α) with respect to temperature for hydrogen oxidation on Ni-, Co-, NiS- and CoS-YSZ anodes.

M.M. Pakulska, C.M. Grgicak, J.B. Giorgi. *The effect of metal and support particle size on NiO/CeO_2 and NiO/ZrO_2 catalyst activity in complete methane oxidation.* Journal of Applied Catalysis A, 322, 124-129 (2007).

This article describes the catalytic activity of CeO_2 and ZrO_2 supported NiO catalysts. This work was not part of my main project and therefore is not included in this thesis. My contribution to this work was to provide material characterization and analysis.

C. Poulin, M.A. Brown, Y.A. Wasslen, C.M Grgicak, K. Fagnou and J.B. Giorgi. *Reactivity of Mesoporous Palladium Yttria-Stabilized Zirconia for Solution Phase Reactions.* Canadian Journal of Chemistry, 84, 1-9 (2006).

This article describes the use of mesoporous Pd-YSZ materials for organic reaction catalysis. This work was not part of my main project and therefore it is not part of my thesis. My contribution to this work was to provide help with material characterization and analysis.

C.M. Grgicak, R.G. Green and J.B. Giorgi. *Control of Microstructure, Sinterability and Performance in Co-Precipitated NiYSZ, CuYSZ and CoYSZ SOFC Anodes.*. Journal of Materials Chemistry, 16, 885-897 (2006).

This article describes the relationship between synthesis conditions, microstructure and SOFC performance for Ni-, Cu- and Co-YSZ anodes. (Chapter 3) The Cu- and Co-YSZ co-precipitated anodes were compared to Ni-YSZ.

C.M. Grgicak and J.B. Giorgi. *YSZ Phase Purity and Stability in Chemically Prepared SOFC Anodes*. Proceedings of the Ninth International Symposium on Solid Oxide Fuel Cells, Quebec City, Quebec, **2005-07**, 1200-1209 (2005).

This article describes the issues related to $mZrO_2$ formation that occurred during co-precipitation. It emphasized the differences between Ni- and Cu-YSZ precipitation and the effects of pH, metal content and yttria content on powder characteristics. (Chapter 3)

C.M. Grgicak, R.G. Green, W.F. Du and J.B. Giorgi. *Synthesis and Characterization of NiO-YSZ Anode Materials: Precipitation, Calcination and the Effects on Sintering.* Journal of the American Ceramic Society, **88**, 3081-3087 (2005).

This article describes the relationship between synthesis conditions and microstructure for Ni-YSZ anodes. (Chapter 3)

Summary

This work examined several cermet materials as possible anode materials for solid oxide fuel cell (SOFC) systems operating in multiple fuel environments. In particular, these materials consisted of two phase M-YSZ (M=Ni, Cu or Co, YSZ= yttria stabilized zirconia) cermets synthesized via the gel-precipitation method. Relations between synthesis conditions and cermet structure/performance dominated the first section of this work. SOFC anode performance was correlated back to original synthesis conditions, whereby d_M/d_{YSZ} was controlled via the production of a crystalline intermediate.

Electrochemical characterization of Ni- and Co-YSZ anodes in H_2 and H_2S/H_2 fuels was performed and each arc observed in the impedance curves was ascribed to a specific process. The high- and mid-frequency arcs were related to transport and charge transfer processes respectively. Non-traditional relationships between inverse Tafel (Lefat) slopes and temperature were observed. This resulted in a change in charge transfer coefficients with respect to temperature. By evaluating this dependence, a charge transfer coefficient of 1.5 for hydrogen oxidation on Ni-, Co- and NiS- anodes was determined. CoS- anodes resulted in a charge transfer coefficient of 0.2.

NiS- and CoS- anodes were stable in sour gas environments and selective towards the electrochemical oxidation of H_2 over H_2S as suggested by open circuit voltage and mass spectrometry.

Cell performances of and CoS- anodes in sour gas environments were stable over a 6 day period and showed no signs of deterioration. However, H_2S was required in the fuel stream to maintain optimal performance of these anodes. Once H_2S was removed, the CoS- anodes reverted to Co-YSZ. For CoS- based anodes, optimum cell performance was maintained at a H_2S content >1v/v%.

Investigations of bimetallic NiCu- and NiCo- anodes were also performed. The addition of Cu to Ni- based anodes resulted in larger metal particle sizes and decreased anode activity for hydrogen oxidation. Small additions of Co to Ni- based anodes showed a marked improvement in hydrogen oxidation activity. The bimetallic anodes were also tested in H_2S/CH_4 mixtures and showed good activity for all anodes tested over a 15 hour period.

These results suggest metal sulfides are viable anode materials for SOFC systems in a multitude of sour gas fuel environments.

Acknowledgements

I would like to thank Professor Javier B. Giorgi, my research supervisor, for his direction, guidance and support throughout the course of my work. His door was always open and he was always willing to give professional assistance and suggestions whenever difficulties or questions arose.

I also wish to acknowledge all the Giorgi group members past and present. I would particularly like to thank Richard G. Green for helping me design and build the fuel cell reactor and running and analyzing all XPS data. This work would not have been possible without his assistance. I would also like to thank Malgosia Pakulska for synthesizing the bi-metallic powders described in Chapter 7 and Appendix C of this thesis and Ron Hartree for running and analyzing all XRF data. I also wish to acknowledge Dr. Osnat Younes-Metzler, Dr. Shiliang Wang and Dr. Wendy Pell for many fruitful discussions.

Finally, I would like to thank my family for their patience and support throughout the course of my work.

1. Introduction

1.1 Definition of a fuel cell

Fuel cells are electrochemical energy conversion devices that directly convert chemical energy from a reaction between fuel and oxidant, into electrical energy. Generally, a fuel cell produces electricity, water and heat using H_2 as fuel and oxygen in air as the oxidant.

$$\text{Hydrogen} + \text{Oxygen} \rightarrow \text{Water} + \text{electrical power} + \text{heat}$$

The construction of a fuel cell is conceptually simple and is depicted in Figure 1.1. Porous electrodes are placed on either side of a separator, which is the electrolyte. The electrolyte is in intimate contact with the anode (negative electrode) and cathode (positive electrode). The fuel fed to the anode and the oxidant fed to the cathode react electrochemically to generate a current and voltage. Unlike a battery which must be either discarded or recharged once the chemicals originally present are consumed, a fuel cell can theoretically produce electrical energy for as long as fuel and oxidant flow to their respective electrodes. However, the degradation of fuel cell components tends to limit its lifespan. Hence to make fuel cells a realistic and commercially viable power generator, developments in both materials and manufacturing of fuel cell components is a necessity.

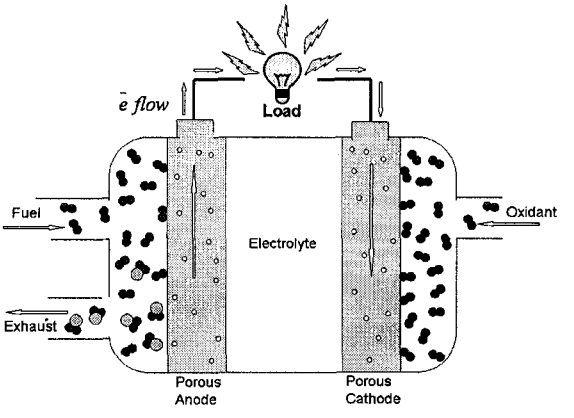

Figure 1.1 Schematic of a fuel cell

1.2 Historical Background

Despite the recent intense activity in fuel cell research, they are not a new technology. The concept of the fuel cell was first demonstrated by William Grove. While investigating

the electrolysis of water, Grove observed that when the current was switched off a small current flowed in the opposite direction. Grove confirmed this by exposing two platinum electrodes to hydrogen and oxygen which resulted in current flow and water production.[1]

The development of solid or ceramic fuel cells began with the breakthrough from Nernst at the end of the 19th century, when Nernst discovered that zirconia, which is an insulator at room temperature, became ionically conductive at temperatures above 600°C. The conductivity was intensified when other oxides such as calcia, magnesia and yttria were used as dopants. The most promising of the mixtures included yttria combined with zirconia. This mixture is still the most widely used electrolyte in Solid Oxide Fuel Cells (SOFC).

The first working SOFC was demonstrated by Baur and Preis, using yttria-stabilized zirconia as the electrolyte, iron or carbon as the anode and magnetite (Fe_3O_4) as the cathode. Although operation of an SOFC was demonstrated, the current output was too low to be considered a viable alternative to batteries. Improvements in the electrolyte design and electrode compositions needed to be considered. Additionally, understanding of fuel reactions needed to be explored.[2]

The first period of intense research activity and subsequent use of viable fuel cell systems came in the 1960's in the space-technology sector with the use of alkaline fuel cell system in the NASA Apollo space program from 1960 to 1965[3]. The research activities continue today with the research emphasis spanning all aspects of fuel cell technology. Improvements in electrolyte conductivity, anode/cathode microstructure, fuel utilization and poison resistance have all occurred due to this widening interest in fuel cells.

1.3 Types of Fuel Cells

There are five main types of fuel cells that are usually classified by their electrolyte. Depending on the electrolyte, either protons or oxide ions are transported through. The largest difference between fuel cells lies within their operating temperatures. Table 1.1 shows a summary of the typical conditions, components and electrochemical reactions for each fuel cell.

The operating temperatures have consequences for design, manufacturing and fuel options. Generally, fuel cells that operate at elevated temperatures can be used with fuels other than hydrogen, but retain the disadvantage of losing efficiency due to their energy requirements.

1.4 Solid Oxide Fuel Cells

A solid oxide fuel cell is an electrochemical device that converts the energy of a chemical reaction directly into electrical energy. Due to the use of solid electrolytes, the operating temperatures are high (~800-1000°C).

Table 1.1: Typical conditions, components and electrochemical reactions for each type of fuel cell[4,5].

	Alkaline fuel cell (AFC)	Phosphoric Acid fuel cell (PAFC)	Polymer Electrolyte fuel cell (PEM)	Molten Carbonate fuel cell (MCFC)	Solid Oxide fuel cell (SOFC)
Anode reaction	$H_2 + 2OH^- \rightarrow 2H_2O + 2e^-$	$H_2 \rightarrow 2H^+ + 2e^-$	$H_2 \rightarrow 2H^+ + 2e^-$	$CH_3OH + H_2O \rightarrow CO_2 + 6H^+ + 6e^-$	$H_2 + 2O^{2-} \rightarrow H_2O + 2e^-$
Cathode reaction	$O_2 + 2H_2O + 4e^- \rightarrow 4OH^-$	$O_2 + 4H^+ + 4e^- \rightarrow 2H_2O$	$O_2 + 4H^+ + 4e^- \rightarrow 2H_2O$	$1.5O_2 + 6H^+ + 6e^- \rightarrow 3H_2O$	$O_2 + 4e- \rightarrow 2O^{2-}$
Electrolyte	NaOH, KOH	H_3PO_4	Proton conducting polymer (nafion™)	Molten Li_2CO_3/K_2CO_3	Y_2O_3-ZrO_2
Anode Material	Pt, Pd, Ni	Pt	Pt	Ni, Cr, Pt, Ru	Ni-YSZ, Cu-YSZ
Cathode Material	Pt, Au	Pt	Pt	Li-NiO, Pt	LSM
Temperature (°C)	70-90	200	80	650	1000
Advantages/ Disadvantages	Requires pure H_2. Poisons easily with CO and CO_2	Able to operate on H_2 contaminated with CO_2	Requires pure H_2. Poisons easily with CO	Runs on syngas which can be internally formed by hydrocarbon reforming	Can run on H_2 or internally reformed hydrocarbons. Requires high temperatures.

A SOFC has many advantages in terms of its theoretical efficiency, reliability, modularity, fuel flexibility and environmental friendliness. Due to the high operating temperatures, steam produced by SOFCs can be used with microturbines or gas turbines to produce electrical power, which enhances the system efficiency.[6,7] The principle of an SOFC is illustrated in Figure 1.1, where the oxidant (O_2) is reduced at the cathode. The resulting oxide ions (O^{2-}) are transported through the electrolyte (YSZ), and fuel (H_2, CO, H_2S, hydrocarbons) is oxidized at the anode.

The reaction occurring at the cathode is,

$$\frac{1}{2}O_{2,c} + 2e^- \rightleftarrows O_e^{2-} \quad (1.1)$$

where the subscripts c and e refer to states at the cathode and electrolyte respectively. If hydrogen is the fuel, the reaction at the anode (a) is

$$H_{2,a} + 2O_e^{2-} \rightleftarrows H_2O_a + 2e^- \quad (1.2)$$

and the overall reaction is

$$H_{2,a} + \frac{1}{2}O_{2,c} \rightleftarrows H_2O_a \quad (1.3)$$

At standard state, E^0 (standard potential) is given by

$$E^o = -\frac{\Delta_r G^o}{nF} \quad (1.4)$$

where $\Delta_r G^o$ is the standard Gibbs free energy, n the number of electrons involved in the reaction to convert a single fuel molecule and F is the Faraday constant (96485.34 C/mol). At conditions other than steady state, the potential (E_{FC}^o) depends upon the partial pressures

of gases (P_i), the stoichiometric number of the reaction (υ_i) and the temperature (T) as per the Nernst equation.

$$E_{FC}^{o} = E^{o} - \frac{RT}{nF}\ln\left(\prod P_i^{\nu_i}\right) \quad (1.5)$$

1.5 SOFC Efficiencies

In order for SOFC's to become viable energy production devices, their overall efficiency must be improved by enhancing the performance of each individual component as well as the compatibility between these components. The overall fuel cell efficiency (ε_{FC}) of a SOFC is the product of the thermodynamic (ε_T), heating (ε_H), current/Faradaic (ε_i) and voltage (ε_V) efficiencies. The following sections are a summary of each type of efficiency as described by *deBoer*.[5]

1.5.1 Theoretical Efficiency

Since the SOFC is an electrochemical device, the free energy change may be totally converted to electrical energy. Therefore, the thermodynamic efficiency is represented by

$$\varepsilon_T = \frac{\Delta_r G_T^o}{\Delta_r H_T^o} \quad (1.6)$$

where $\Delta_r H_T^o$ is the standard enthalpy and $\Delta_r G_T^o$ is the Gibbs energy of reaction at temperature T. Since the operating temperature of an SOFC is very high, variations of enthalpy and Gibbs energy cannot be ignored and are expressed in terms of Kirchoff's Law and the Gibbs-Helmholtz equation respectively.[8] Taking these changes into account, the theoretical efficiency of an SOFC operating with H_2 as fuel at 850°C is 0.77 (see Appendix A).

1.5.2 Heating Efficiency

Heating efficiency is important when the fuel contains impurities or is diluted by inert species.

$$\varepsilon_H = \frac{\Delta_r H_T^o}{\Delta_r H_{TOT,T}^o} \quad (1.7)$$

where $\Delta_r H_T^o$ is the enthalpy of fuel species available to generate electricity and $\Delta_r H_{TOT,T}^o$ is the amount of enthalpy included in all combustible species.

1.5.3 Current Efficiency

The current efficiency is the ratio of the measured current to the theoretical current, as predicted by Faraday's Law.

$$\varepsilon_i = \frac{i_{measured}}{i_{theoretical}} \quad (1.8)$$

$$i_{theoretical} = nF\frac{\partial f}{\partial t} \quad (1.9)$$

where n is the number of transferred electrons, F is the Faraday constant and $\frac{\partial f}{\partial t}$ is the molar flow rate of the fuel.

1.5.4 Voltage Efficiency

As current is drawn from a cell to obtain electrical work, the equilibrium cell potential is reduced. The voltage efficiency is given by

$$\varepsilon_V = \frac{E}{E_{FC}^o} \quad (1.10)$$

where E is the potential under load and E_{FC}^o is the Nernstian potential, or open circuit potential (OCV) of the cell.

For the voltage efficiency to remain high, the absolute difference between E and E_{FC}^o must remain small. The difference between these values is defined as the polarization or overpotential (η)

$$\eta = E_{FC}^o - E \quad (1.11)$$

1.5.4.1 Polarization

The following is a summary of various types of polarization and their effect on electrochemical performance as described by *Conway* in his *Notes on Thermodynamic, Electrochemical and Kinetic Aspects of Battery Reactions*.[9]

The total cell polarization is made up of η_a and η_c (activation polarizations associated with the anode and cathode kinetics, respectively), iR (ohmic polarization) and η_{cp} (concentration polarization).

$$\eta_{tot} = \eta_a + \eta_c + iR + \eta_{cp} \qquad (1.12)$$

Figure 1.2 shows how the main contributions of the polarization of a battery or fuel cell depend on current density. The SOFC or battery output voltage decreases with current drain.

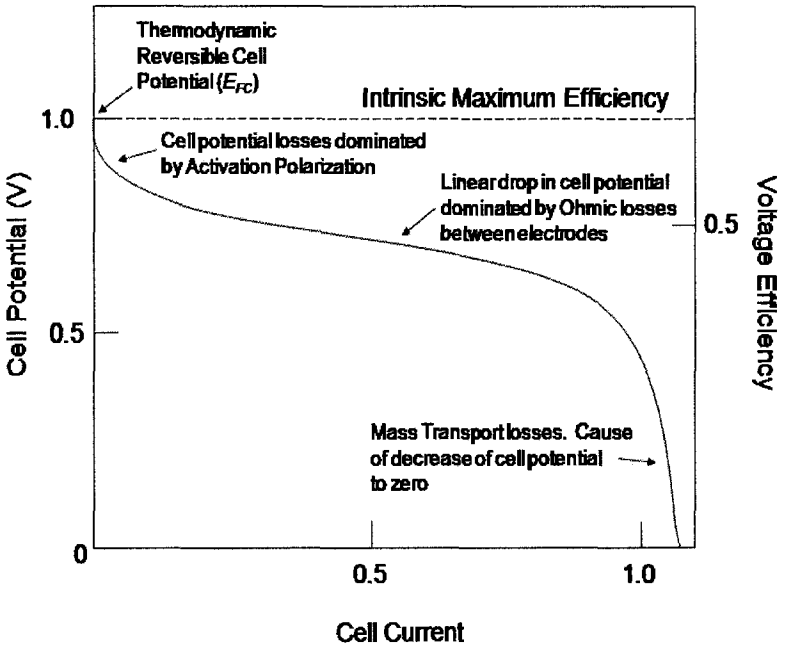

Figure 1.2 Polarization contributions as a function of cell current.

Using a reference electrode, the individual electrode polarizations may be determined. Figure 1.3 shows an example of the effects each electrode has on the total cell output. In this case, the polarization characteristics of the anode and cathode are similar. If the polarizations are large, the fuel cell will not be able to generate a significant amount of power. Therefore, polarizations of both electrodes and the electrolyte must be kept to a minimum.

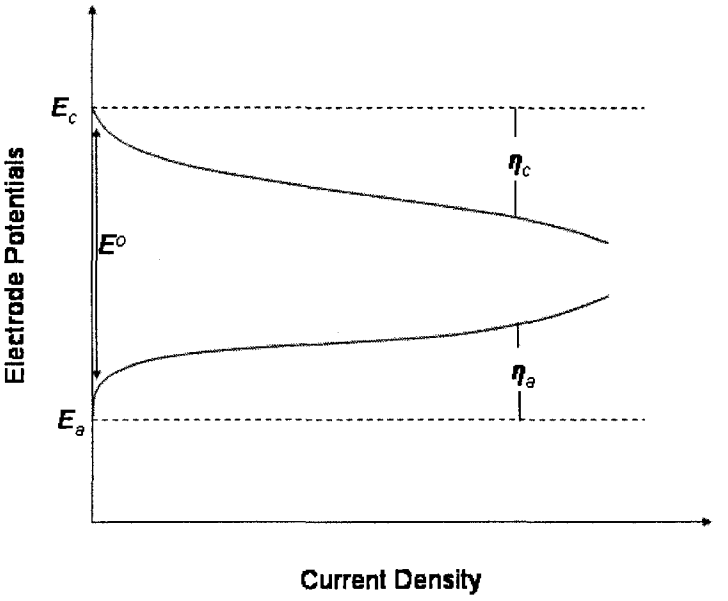

Figure 1.3 Polarization diagram with comparable anodic and cathodic contributions.

1.5.4.1.1 Activation Polarization

All electrochemical processes require a driving force (potential) to make them proceed at net rates that exceed the spontaneous reversible rate of the electrode reaction (i_o – exchange current density). An extra potential (η) is required to lower the normal free energy of activation of an electrode process, so that the net rate is greater than i_o. The overpotential required to modify the activation energy of an electrode process is called "activation polarization".

For an overpotential η, the free energy of activation $\Delta G^{o\neq}$ is lowered from its reversible value by $\beta\eta F$, where β is a charge-transfer parameter dependent on the symmetry of the energy barrier associated with activation in the reaction process and is usually assumed to be 0.5 (see Appendix B) for a one-electron process.

$$\Delta G_{\eta}^{\neq} = \Delta G^{o\neq} - \beta\eta F \quad (1.13)$$

Conceptually, the extra applied voltage makes electrons "more available" in the metal for the cathode and makes the anode more of an electron sink (electrons become "less available").

The rate constant of an electrochemical reaction at equilibrium is

$$k_o = A\exp\left(-\frac{\Delta G^{\neq}}{RT}\right)\exp\left(-\frac{\beta E^o F}{RT}\right) \quad (1.14)$$

At any potential differing from E^o, (i.e. potential E)

$$k_E = A\exp\left(-\frac{\Delta G^{\neq}}{RT}\right)\exp\left(-\frac{\beta EF}{RT}\right) \quad (1.15)$$

if

$$E = E^o + \eta \quad (1.16)$$

$$k_E = A\exp\left(-\frac{\Delta G^{\neq}}{RT}\right)\exp\left(-\frac{\beta E^o F}{RT}\right)\exp\left(-\frac{\beta\eta F}{RT}\right) \quad (1.17)$$

$$k_E = k_o\exp\left(-\frac{\beta\eta F}{RT}\right) \quad (1.18)$$

where k_o is the electrochemical rate constant for the process. Since electrochemical rates are measured by currents,

$$\vec{i} = i_o\exp\left(-\frac{\beta_c\eta_c F}{RT}\right) \text{ where } i_o = nFk_o[S] \quad (1.19)$$

where $\vec{i}$ is the net current density for the forward reaction, i_o is the exchange current density and [S] is the concentration of the reacting species, n is the number of electrons, F is the Faraday constant, η_c is the cathodic or negative overpotential and β_c ($0<\beta_c<1$) is the symmetry factor associated with the cathodic (forward) branch of the reaction. The treatment is the same for the reverse reaction ($\vec{i}$). These are the fundamental equations for the kinetic aspects of electrode processes. By measuring current density versus overpotential (in a 3-electrode system), the individual anode or cathode performances can be evaluated so the polarization behaviour of each can be determined. By plotting ln$i$ vs η, i_o (hence k_o) may be obtained. The relationships mentioned are valid only in the region of activation control, where there is no influence from concentration or adsorption polarization. Therefore changes in η are only due to activation of the electrochemical process through changes in the electrochemical free energy.

1.5.4.1.2 Ohmic Polarization

If the electrolyte between electrodes has a finite ohmic resistance R (Ω/cm^2), the passage of current introduces a potential drop (iR) in the cell. The iR drop also includes contact resistance between cell components and electrical resistance of the electrodes. Given that the ohmic polarization or "iR drop" increases linearly with current, while the activation polarization increases with ln$i$, the net polarization often increases in a complex way with i. However, over short current ranges, the total polarization often appears to increase linearly after the initial, rapid increase at the beginning of the η vs i curve.

1.5.4.1.3 Concentration Polarization

Concentration polarization is associated with the depletion of electrochemical reagents at or near the electrode surface due to their consumption by the current itself. Concentration gradients and local potential differences develop near the electrodes. The limiting current (i_L) is reached when the electrode process is dominated by mass transport effects. The concentration polarization can be expressed by

$$\eta_{cp} = \frac{RT}{nF} \ln\left(1 - \frac{i}{i_L}\right) \quad (1.20)$$

This type of polarization typically arises in porous electrodes, accentuating the importance of microstructure in SOFC electrodes.

1.6 Scope

This thesis deals with a number of issues related to SOFC anode performance. The main purpose was to design anodes exhibiting superior performance to that of Ni-YSZ by evaluating activation overpotentials (i.e. voltage efficiency) of these anodes in multiple fuel environments (H_2, CH_4, H_2S/H_2 and H_2S/CH_4). Increased resistivity to poisons and decreased anode activation polarization in various fuels were the main criteria for success.

Since overall anode performance is related to a multitude of variables such as anode microstructure, composition, processing, kinetics and fuel choice, each chapter contains a review of relevant literature related to the specific area of interest. Chapter 2 describes the experimental considerations and SOFC set-up. It emphasizes the importance of electrode geometry on solid electrolytes and various analytical considerations involved in anode characterization. Nickel, copper and cobalt electrodes obtained through precipitation are the subject of Chapter 3, where the relationship between synthesis strategies, anode morphology, processing and SOFC performance was determined. Evaluation of electrochemical data in Chapters 4 and 5 show changes in fundamental kinetic parameters at various temperatures on multiple anodes. Interpretations related to these changes are discussed.

Results pertaining to anode performance in alternative fuel environments (i.e. CH_4 and H_2S/CH_4) are discussed in Chapter 6. Both nickel and cobalt anodes showed increased exchange current densities (i_o) when H_2S was added to the fuel stream. Evaluation of post-run anodes suggests the conversion of metal to metal-sulfide was the main cause for improved performance. Chapter 7 evaluates the benefit of using bi-metallic anodes consisting of nickel-copper and nickel-cobalt mixtures in H_2, CH_4 and H_2S/CH_4 fuels. An overall evaluation of the results is given in Chapter 8.

References

(1) Grove, W. R. *Phil. Mag.* **1839**, *14*, 127.

(2) Singhal, S. C.; Kendall, K. *High temperature solid oxide fuel cells*; Elsevier Ltd: New York, 2003.

(3) Carrette, L.; Friedrich, K. A.; Stimming, U. *Chem. Phys. Chem.* **2000**, *1*, 162.

(4) Ormerod, R. M. *Chem. Soc. Rev/* **2003**, *32*, 17.

(5) Boer, B. d. SOFC Anode: Hydrogen oxidation at porous nickel and nickel/yttria stabilised zirconia cermet electrodes. PhD Thesis, University of Twente, 1998.

(6) Jiang, S. P.; Chan, S. H. *J. Mater. Sci.* **2004**, *39*, 4405.

(7) Zhu, W.; Deevi, S. *Mater. Sci. Eng.* **2003**, *A362*, 228.

(8) Atkins, P. W. *Physical Chemistry*, 5 ed.; Oxford University Press, 1994.

(9) Conway, B. E. Notes on Thermodynamic, Electrochemical and Kinetic Aspects of Battery Reactions Ottawa, 1978; pp 17.

2. Experimental/Analytical Considerations

2.1 Summary

Since the focus of this thesis was to describe the anode best suited for use in variable gas systems, it was necessary to describe the microstructure of each anode appropriately. In this chapter, a detailed analysis of each characterization technique, along with the assumptions and their relevance is discussed.

The electrochemical performance of the cells must also be well defined and understood. Inconsistencies which include, but are not limited to overlapping anodic and cathodic overpotentials, anode processing, pressure and temperature considerations are evaluated in the second half of this chapter.

This chapter evaluates the general methodologies and does not include specific procedures used to synthesize and characterize the anodes. These are detailed in subsequent chapters.

2.2 Synthesis of Anode Precursors

The anodes were precipitated via co-precipitation of metal, yttrium and zirconium ions with NH_3 gas and/or a 2M NaOH solution. The theoretical yield was 10g of MO-YSZ with varying amounts of MO. The most common ratio was 70%w/w MO and 30%w/w YSZ mixture. The appropriate amounts of M-chloride, Y_2O_3 and $ZrCl_4$ were dissolved in 165 ml of distilled H_2O. Since Y_2O_3 is insoluble in water, it was pre-dissolved in 10ml concentrated HCl, stirred and heated to approximately 70°C. To begin precipitation, a 65 sccm flow of NH_3 was introduced at room temperature via a glass tube which was inserted into the solution. The solution was stirred by a magnetic stir bar and Thermolyne Ciramec2® stir plate at a rotation set point of 7. Introduction of 2M NaOH was accomplished using a burette at a rate of ~0.5ml/sec. The pH was measured during precipitation via a Hanna Checker® pH meter. Once the desired pH was reached the precipitate was filtered and washed 3 times. Washing was accomplished by adding the full amount of filtered precipitate into 500 ml distilled H_2O, stirring as previously described and re-filtering.

The entire sample was dried at 120°C overnight and crushed manually with a mortar and pestle for approximately 1 min. The crushed sample was then weighed and a portion of this sample was separated for calcination. Calcination was performed in a Thermolyne 46100 high temperature furnace at 750°C or 950°C for 2 hours using a ramp speed of 10°C/min.

2.3 Characterization – Analytical Considerations

2.3.1 Visible Spectroscopy

Visible spectroscopy was used to determine the presence of metal-ammonia complexes in solution throughout the precipitation process because it allows for the identification of coordinated complexes in solution without actually needing to isolate each species. That is, for each metal-ligand system studied,

$$M^{x+} + nL^{y-} \rightleftarrows [ML_n]^{x-ny} \quad (2.1)$$

the n-value can be determined experimentally from the spectra of a series of solutions. Each of the absorption maxima can be used to characterize the complexes in solution as there is a shift of wavelengths with varying amounts of ammonia ligand complexation.

Because deviations from direct proportionality between absorbance and concentration are frequently encountered, quantitative analysis was not performed due to the nature of the solutions.

2.3.1.1 Concentration Limitation

Highly dilute solutions are required to ensure no deviation from the direct proportionality between absorbance and concentration.

$$Abs=\varepsilon b[S] \quad \lim c\rightarrow 0 \quad (2.2)$$

The direct proportionality is known to break down at high concentrations since

$$\varepsilon=f([S]) \quad (2.3)$$

At high concentrations (usually > 0.01M), the average distance between molecules is diminished enough for each molecule to affect the charge distribution of its neighbours and in turn alters the wavelength at which the molecule absorbs.[1]

2.3.1.2 Chemical Limitation

Apparent deviation from Beer's law will also arise when an analyte reacts in solution. As previously mentioned, the ratio of water to ammonia is variable throughout the precipitation

process; therefore a shift in absorption wavelength is expected. The chemical deviations throughout the precipitation process make calibration of each metal complex impossible.

2.3.2 Infrared Spectroscopy

Vibrational characterization of the powders was determined using Attenuated Total Reflection Fourier Transform Infrared spectroscopy (ATR-FTIR). XRD was used to probe the long-range structure of the material, ATR-FTIR was considered complimentary to XRD.

Quantification of each species was not performed due to the difficulty of monitoring the amount of sample between runs. Although this may be remedied by adding an internal standard, the continuing issue of overlapping/ broad bands was a concern. Most of the powders tested were metal hydroxides or complex basic salts that continuously exhibited overlapping broad bands which made de-convolution difficult. Additionally, previous studies of metal precipitated solutions showed the ν_{OH} band at ~3650cm^{-1} changes with respect to the crystallinity of the sample. That is, a decrease in peak height/area is not only related to concentration variations, but a change in crystallinity and/or structure.[2-5]

2.3.3 X-ray Fluorescence

X-ray fluorescence (XRF) was used as the principle quantitative technique to determine powder compositions. With carefully prepared calibration standards XRF is capable of producing quantitative analyses of complex materials with precision that equals that of classical wet chemical methods. The major concern of this analytical technique was to ensure homogeneously mixed calibration standards. This is easily accomplished with careful consideration to the mixing procedure.

Figure 2.1 shows an example of a calibration curve used to quantify metals. These standards consisted of a mixture of $NiCl_2$, Y_2O_3 and $ZrCl_2$. The powder mixtures were mechanically mixed and pelleted in Paraffin binder (Spex). Both sides of the pellet were analyzed to ensure homogeneous mixing of the sample.

The calibration curve is a comparison between the Kα peak heights of each metal with respect to metal concentration.

Quality control of the prepared anode powders was also undertaken by random XRF scans which, were used to ensure the exclusion of any alkali metals in the prepared powders since they have been linked to the deactivation of catalysts in a number of applications.[6-8]

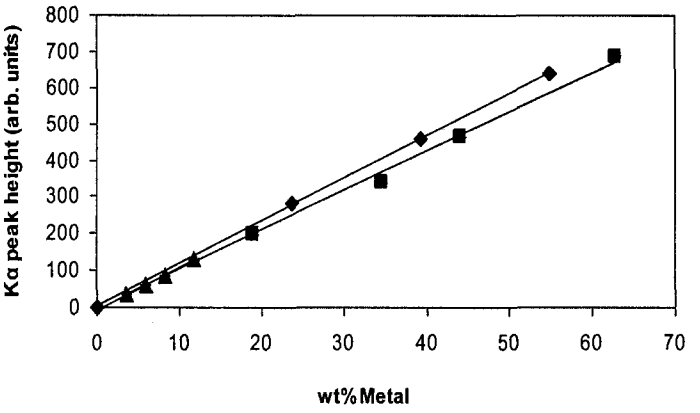

Figure 2.1. XRF calibration curve used to determine relative metal concentrations in SOFC anode precursors (♦)Ni, (■)Zr and (▲) Y.

2.3.4 Scanning Electron Microscopy and Energy Dispersive X-ray Spectroscopy

Scanning Electron Microscopy was used to examine the morphologies of the final powders and sintered materials. Despite the non-conductive nature of the mixed metal oxides, analysis of the calcined powders was performed without the aid of a sputtered coating. Thick coatings may obstruct fine surface details and are a concern when looking at powders in the nanoscale regime. Examination of the powders without sputtering was achievable since it was observed that there was a minimal build-up of charge during analysis.

However, charging due to impeded flow of electrons to ground was highly visible when sintered materials were analyzed. Therefore gold sputtering was necessary to view the morphology of these samples. Since the particle sizes of these materials were in the microscale range, loss of nanoscaled details was not a concern.

Energy Dispersive X-ray Spectroscopy (EDX) was used in conjunction with SEM to determine the elemental composition of individual particles. EDX was not used to quantify materials since XRF was deemed more suitable for this purpose.

2.3.5 X-ray Diffraction

X-ray diffraction (XRD) was an indispensable tool for materials characterization. It was possible to excise a remarkable amount of materials information from one diffractogram. XRD was used to determine phase composition, crystallite size and substitution effects by utilizing changes in lattice constants. However, to do this properly, care with respect to peak refinement and peak placement must be taken.

2.3.5.1 Peak Position and Theta Calibration

Theta calibration is a means to correct the observed pattern for significant angular deviation when instrumental and experimental imperfections exist. This is particularly significant when determining such properties as changes in lattice parameters between samples. A standard reference material (SRM) is required to provide the reference peak locations for the calibration. The SRM used as an internal standard was SRM 660 LaB_6 (National Institute of Standards and Technology). The reference material resulted in a diffractogram with well resolved peaks and was compared to the reference lines defined by NIST. The corrected 2θ peaks produced by interpolation of observed data points using the standard was the pattern used for peak refinement. The SRM was only used in samples where lattice constants were calculated since the material was unusable for other characterization techniques after internal standard was mixed into the sample.

2.3.5.2 Peak Refinement

The accuracy of any calculated property is a direct result of the appropriateness of the peak fitting. In XRD, the resultant peak intensities, areas and positions were obtained by refinement of the raw data peaks. These fitted values were subsequently used to analyze the materials properties such as crystallite size.

Prior to peak refinement, a subtraction of background noise and $K_{\alpha 2}$ peaks was performed, where the $K_{\alpha 2}$ contribution was assumed to be one half of $K_{\alpha 1}$. The ability to subtract the $K_{\alpha 2}$ component from the diffractogram is of particular interest if proper refinement is required to obtain accurate peak placement and intensity. This is particularly important for low angle peaks where the $K_{\alpha 1}$ and $K_{\alpha 2}$ peaks substantially overlap. Once the background and $K_{\alpha 2}$ contributions were removed, the peaks were refined using a pseudo-Voigt function[9]

$$I_i = I_p * \frac{r}{1 + k\Delta 2\theta^2 + (1-r)e^{-0.693\, k\Delta 2\theta^2}} \quad (2.4)$$

where I_i is the calculated profile intensity of a data point at $\Delta 2\theta = 2\theta_i - 2\theta_p$ (where $2\theta_p$ is the peak position and $2\theta_i$ is the calculated peak position), I_p is the peak height, r is the Lorentzian component (mixing/tailing factor) in the pseudo-Voigt, and

$$k = \frac{4(1 \pm S)}{W_{1/2}^2} \quad (2.5)$$

where $W_{1/2}$ is the width at half height and S is the skewness parameter (profile asymmetry) with a plus sign when $\Delta 2\theta > 0$, and a minus sign when $\Delta 2\theta < 0$.

During peak fitting, all parameters were left open for refinement except skewness which was assumed constant at 0.

2.3.5.4 Peak Widths and Crystallite Sizes

The most common mathematical relationship used to assess crystallite size is given by the Scherrer equation

$$t = \frac{0.9\lambda}{W_{1/2}^{c} \cos\theta_{\beta}} \quad (2.6)$$

where t is the crystallite size, λ is the wavelength of the incident radiation, $W_{1/2}^{c}$ is the width at half height, due to crystallite size and θ_{β} is related to the peak position.

Although there is a link between peak width and crystallite size, other sources of peak broadening must be considered. First, the peak broadening due to the instrument must be assessed. This was accomplished by acquiring a representative scan pattern from a standard reference material that does not exhibit significant specimen broadening, such as LaB_6. The $W_{1/2}$ values were representative of the instrument broadening since the specimen broadening of this sample is negligible.

Secondly, microstrain within the crystallites may also lead to peak broadening. In a material there may be strain that varies within a grain. These are known as microstrains. The effect of having a distribution of d-spacings due to microstrain may be obtained by differentiating Bragg's Law with respect to the d-spacing and solving for $d\theta$ *(or* $\Delta\theta$*)*. If Bragg's Law is

$$\frac{n\lambda}{\partial d} = \frac{2d\sin\theta}{\partial d} \quad (2.7)$$

$$0 = 2d\cos\theta \frac{\partial\theta}{\partial d} + 2\sin\theta \quad (2.8)$$

$$-\frac{2\partial d}{d}\tan\theta = 2\partial\theta \text{ or } -\frac{2\Delta d}{d}\tan\theta = 2\Delta\theta \quad (2.9)$$

Since $\Delta 2\theta$ is the change in peak width, the peak broadening due to microstrain is

$$W_{1/2}^{MS} = -2\frac{\Delta d}{d}\tan\theta \quad (2.10)$$

The total width of the peak $W_{1/2}^{tot}$ is from crystallite size and microstrain

$$W_{1/2}^{C} + W_{1/2}^{MS} = W_{1/2}^{tot} = \frac{0.9\lambda}{t\cos\theta} - 2\frac{\Delta d}{d}\frac{\sin\theta}{\cos\theta} \quad (2.11)$$

$$W_{1/2}^{tot}\cos\theta = \frac{0.9\lambda}{t} - 2\sin\theta\frac{\Delta d}{d} \quad (2.12)$$

Equation 2.12 is the Williamson-Hall equation.[10] Plotting $W_{1/2}^{tot}\cos\theta$ against sin θ (once instrument broadening is accounted for) will result in a y-intercept by which one may extract crystallite size and a slope by which the change in d-spacing or microstrain may be obtained. Despite the effort to obtain reasonable and accurate crystallite sizes, it should be noted that two major assumptions were nonetheless employed. The crystallites were assumed to be spherical and the microstrain was assumed constant throughout the crystallite.

2.3.5.5 Quantification of Phases

Although XRF can accurately determine metal concentrations, it cannot be used to determine the relative quantities of phases. For example, if a sample consisted of monoclinic, tetragonal or cubic zirconia, XRF could only determine the amount of zirconium in the sample and not the relative amounts of each crystalline phase. XRD was required for this purpose.

A calibration curve comparing peak height ratios between the YSZ (111) and mZrO_2 (-111) versus weight percent was constructed to determine the relative quantities of each (Figure 2.2).

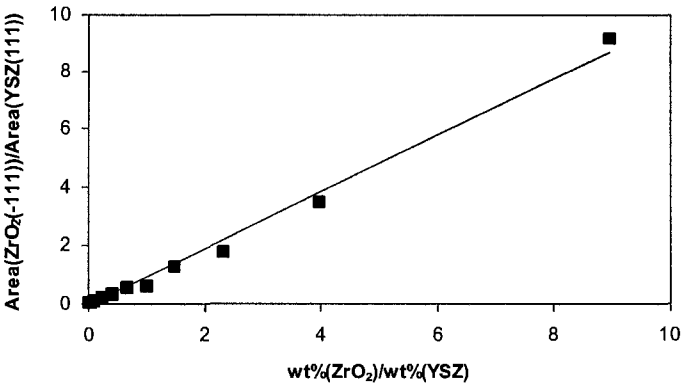

Figure 2.2 XRD calibration curve used to determine relative phase concentrations of $mZrO_2$ and YSZ in SOFC anode precursors.

In this work, the desired anode composition consisted of metal and cubic YSZ phases. The presence of a monoclinic zirconia phase ($mZrO_2$) was not desired since it has inferior oxide conductivity. Quantification of $mZrO_2$ in the anode precursors was used to determine appropriate synthesis conditions for the development of 'phase pure' anodes.

2.3.6 Gas Adsorption

Gas adsorption experiments were utilized to assess the particle sizes of the materials. Nitrogen physisorption was employed to assess materials characteristics such as specific surface area and porosity. Hydrogen chemisorption was used to determine the active metal surface area and/or particle size of the metals.

2.3.6.1 Nitrogen Physisorption

A qualitative interpretation of various characteristics associated with a material may be assessed simply by constructing and examining an adsorption isotherm obtained over a wide range of partial pressures. The adsorption isotherm was determined point-by-point by admitting successive known volumes of nitrogen and measuring the equilibrium pressure. Desorption isotherms were obtained in the same manner but by removing the gas. All adsorption isotherms may be grouped into one of five types identified as Type I to Type V. Understanding the significance of each isotherm shape was necessary to determine the kind of interaction between adsorbate/adsorbant and the appropriate mathematical model to interpret the data.

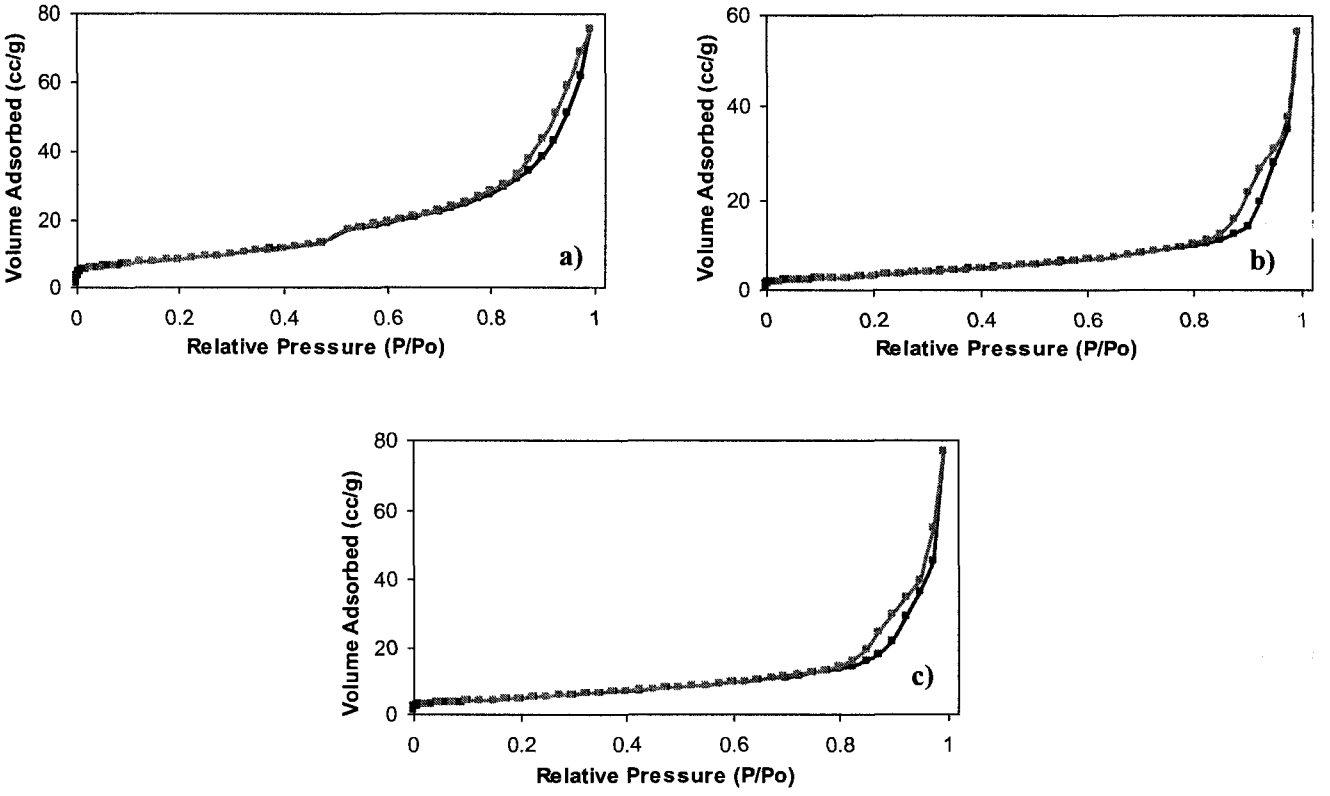

Figure 2.3 Examples of nitrogen adsorption isotherms for a) nickel-YSZ b) copper-YSZ and c) cobalt-YSZ calcined samples. ━■━ Adsorption ━■━ Desorption

Figure 2.3. shows 3 typical isotherms obtained using N_2 as the adsorbate at 77K on calcined Ni- Cu- and Co-YSZ samples used in this study. Each adsorption isotherm is Type II with hysteresis during desorption. Type II isotherms typically are obtained when the absorbent is nonporous or macroporous. The presence of hysteresis during desorption in these samples strongly suggested the presence of macropores. The region generally found at P/P_o 0-0.05 showed a fast rise in the volume of N_2 adsorbed with very little N_2 addition. This region describes the unrestricted monolayer and multilayer adsorption of the gas. The linear central region of the isotherm represents the relative pressure at which monolayer coverage was complete and multilayer coverage dominated. Finally, the instantaneous filling of the pores and condensation was observed at high partial pressures.

The isotherms of the sintered samples did not exhibit the same shape as shown in Figure 2.4.

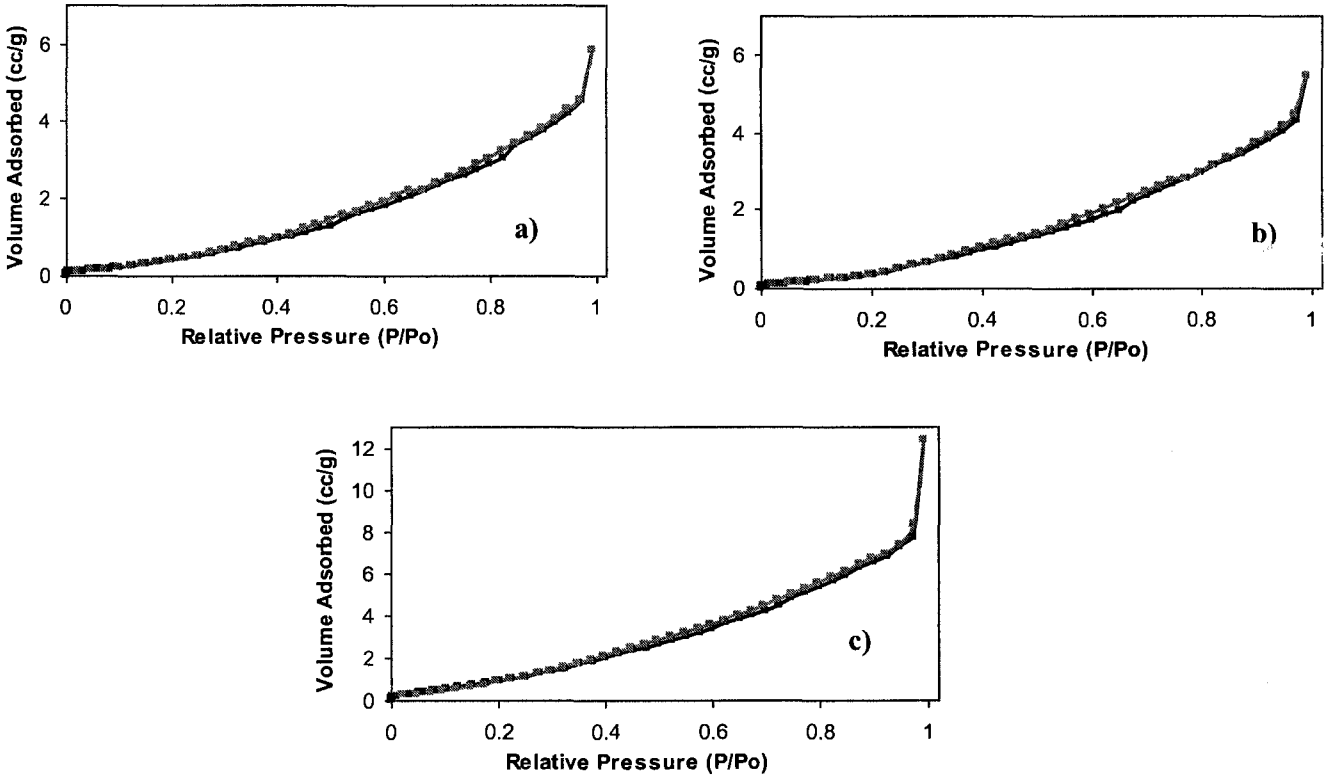

Figure 2.4 Examples of nitrogen adsorption isotherms for (a) nickel-YSZ (b) a copper-YSZ and (c) cobalt-YSZ sintered samples. —■— Adsorption —■— Desorption

The sintered samples isotherms are convex throughout the whole pressure region and therefore exhibit Type III behaviour. Also, there is no hysteresis loop, suggesting a small total pore volume. The sharp increase in adsorption at the last point is related to N_2 condensation on the sample.

Since there was a marked difference in isotherm shape between calcined and sintered samples, consideration was given to the models used to calculate material characteristics such as surface area, porosity, microporosity and particle size.

The most common relationship to determine surface area was developed by Brunauer, Emmet and Teller in 1938.[11] The BET equation,

$$\frac{1}{V\left(P_o/P - 1\right)} = \frac{1}{V_M B} + \frac{B-1}{V_M B}\left(\frac{P}{P_o}\right) \quad (2.13)$$

where V is the volume of gas adsorbed, V_M is the volume of gas adsorbed constituting a monolayer of surface coverage, P/P_o is the partial pressure of adsorbate and B is the BET constant and is related to the energy of adsorption and its value is an indication of the magnitude of adsorbate/adsorbant interactions.

$$B = e^{\frac{(\Delta H_L - \Delta H_1)}{RT}} \qquad (2.14)$$

where ΔH_L is the enthalpy of adsorption for the first layer, ΔH_1 is the enthalpy of adsorption for all subsequent multilayers, R is the gas constant and T is temperature.

The BET relationship may therefore be used to describe both Type II and Type III isotherms and is dependent on the value of B. If B is large, that is, the interaction between adsorbate and adsorbant is significant, then a Type II isotherm will emerge. However, if the interaction between the adsorbate layers are larger than the interaction between the gas and the adsorbant (i.e. $B \leq 1$), then a Type III isotherm will result. As a result the BET model may be used to describe the surface area of both calcined and sintered samples despite the dissimilar isotherm shapes and interaction profiles.

Other benefits of the BET equation are its ease and frequent use within the literature. Disadvantages are the assumptions inherent within the relationship. First, it is assumed that the enthalpies do not vary with respect to surface coverage within a monolayer. Also, except for the first layer, the heats of adsorption of the multilayers do not vary.

BET surface areas calculated using N_2 for microporous samples may not be meaningful considering the relative sizes between micropores (<20Å) and N_2 molecules (4.3Å). Since BET analysis is based on multilayer adsorption, channels/pores that only allow for the adsorption of one or two N_2 molecules will not be correctly accounted for. Based on the isotherms obtained, there is a strong indication of the absence of micropores. A t-plot based on the relationship between the statistical thickness (ξ) of the adsorbed layer and gas phase pressure was used to ensure the absence of micropores and therefore the legitimacy of the BET value.[12-15]

$$\xi = a\left[\frac{1}{\ln\left(P_o/P\right)}\right]^{1/b} \qquad (2.15)$$

where the pre-exponential term *(a)* and the exponential term *(b)* are 6.0533 and 3.0 for nitrogen at 77K respectively. Plotting volume adsorbed (V) versus ξ in the mesoporous ($0.05<P/P_o<0.3$) region will result in a straight line with a y-intercept representing the micropore size. If the intercept is 0, the BET surface area and the t-plot surface area are the same, thereby excluding the presence of micropores. For the purpose of this work, it should be noted that all of the samples tested did not show the presence of micropores.

2.3.6.1 Hydrogen Chemisorption

Characteristics of the catalytic metal on a support can be calculated from chemisorption measurements using hydrogen. By determining the amount of adsorbate needed to form a monolayer of chemisorbed gas (V_M) and by using reasonable assumptions one may calculate parameters related to the number of active sites such as the active metal surface area and dispersion. The isotherm generation follows a pattern similar to that of physisorption. The main differences between the isotherms lie in the inherent distinctions between physisorption and chemisorption. Since chemisorption includes the dissociation of H_2 and subsequently the formation of a chemical bond between the gas and metal, desorption curves are not obtained. However, physisorption contributions are observed during isotherm generation and are visualized by a deviation from the Langmuir isotherm. The ideal Langmuir isotherm would exhibit a quick rise in adsorption at low partial pressures followed by a flat portion of the curve indicating no further adsorption is taking place regardless of the pressures (i.e. there is not multilayer formation). In real systems the contribution from physisorption was observed as shown in Figure 2.5.

Physisorption contributions were exemplified by the increase in absorbed gas within the high pressure range on a freshly treated catalyst, suggesting multilayer formation. By evacuating the sample at the same temperature, thereby leaving the chemisorbed species and reintroducing gas back into the system, the resulting isotherm should represent physical adsorption and therefore fall below the original isotherm. The difference in gas adsorbed between these two curves results in a curve that represents the true chemisorption isotherm. This is the Langmuir isotherm as is evidenced by its shape.

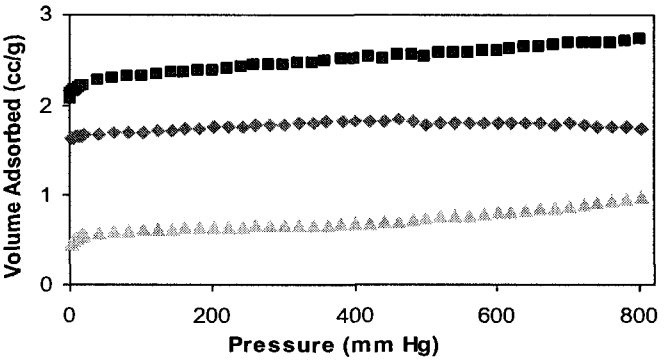

Figure 2.5 Example of hydrogen chemisorption isotherms for nickel-YSZ. (■) Isotherm obtained on freshly treated catalyst, exhibiting both chemisorption and physisorption phenomena (▲)Isotherm obtained after the first analysis and evacuation, exhibiting physical adsorption phenomenon (◆) The difference between the two isotherms, representing chemisorption of H_2 without physisorption contributions.

By using the Langmuir equation

$$\frac{1}{V} = \frac{1}{V_M} + \frac{1}{V_M K_C P^{1/2}} \quad (2.16)$$

where V is the volume of gas adsorbed, V_M is the volume required to fill a monolayer of adsorbed gas, $K_C = \frac{k_{ca}}{k_{cd}}$ is the ratio of the adsorption and desorption rate constants and P is the pressure and plotting $\frac{1}{V}$ against $\frac{1}{P^{1/2}}$ one may obtain a straight line with y-intercept $\frac{1}{V_M}$.

Relationships between V_M, metal dispersion, surface area and particle sizes follow. Like the BET method, the Langmuir model assumes that heats of adsorption are constant throughout the process, despite varying surface coverages. Additionally, particle sizes are calculated assuming spherical geometry.

2.3.7 Sinteractivity

The activation energy of shrinkage was derived from the combined-stage sintering model, which contains contributions of grain-boundary and volume diffusion[16]

$$-\frac{dL}{L}=\frac{\gamma\Omega}{kT}\left(\frac{\delta D_B\Gamma_B}{G^4}+\frac{D_V\Gamma_V}{G^3}\right) \quad (2.17)$$

where L is the actual sample length, γ the surface area, Ω the atomic volume, and δ the grain boundary thickness. Γ_B and Γ_V are each a collection of scaling factors for volume and grain-boundary diffusion, respectively. G is the mean grain size, k is the Boltzmann constant, and T is temperature. D_B and D_V are the diffusion coefficients for grain-boundary and volume diffusion, respectively.

If it is assumed that only one type of diffusion mechanism predominates and Γ and G are independent of density taking the natural logarithm of each side of the equation will result in the following Arrhenius type equation. This was used to determine the activation energy of densification

$$\ln\left(\frac{dL/L_o}{T}\right)=A-\frac{zE_a}{RT} \quad (2.18)$$

where E_a is the activation energy of densification and z is a constant which encompasses all of the values that describe the sintering behaviour of solids.

The constant z includes information on surface energy, atomic volume, grain-boundary thickness, grain size and the diffusion coefficients for grain-boundary and volume diffusion, respectively. Traditionally, the value of z has been estimated to be 0.5 for volume diffusion and 0.33 for grain-boundary diffusion.[16] The predominant mechanism in this work was assumed to be grain-boundary diffusion (n=0.33) based on the mechanism attributed to the sintering of 8% YSZ.[17] Assuming grain-boundary diffusion allowed for direct comparisons between values obtained in this work and those obtained by *Tietz et al*, who analyzed the shrinkage of multiple NiO-YSZ powders commonly used in SOFC work.[18]

2.4 Characterization – Electrochemical

2.4.1 General Electrochemical Set-up

The general experimental set-up, which includes gas control system, electrochemical measuring equipment, furnace, etc, is shown schematically in Fig 2.6. Desired fuel gas mixtures are controlled by two MKS Type 1179A Mass-Flo® Controllers and MKS Type 247D Four Channel Readout. Generally, H_2 and CH_4 were restricted by the 500sccm

controller and H_2S was constrained by the 20sccm one. Individual flow ranges were maintained between 0.4-20sccm or 10-500sccm as per performance specifications acquired from MKS Instruments[19]. The oxidant (air) flow remained constant throughout fuel cell testing.

The temperature was regulated via an Omron E5CN controller and measured with a K-type thermocouple placed outside of the shielded quartz tube. The Chromel®-shielded quartz tube was placed in the furnace around the fuel cell and connected to ground and used as a precaution to reduce any background noise introduced by the furnace.

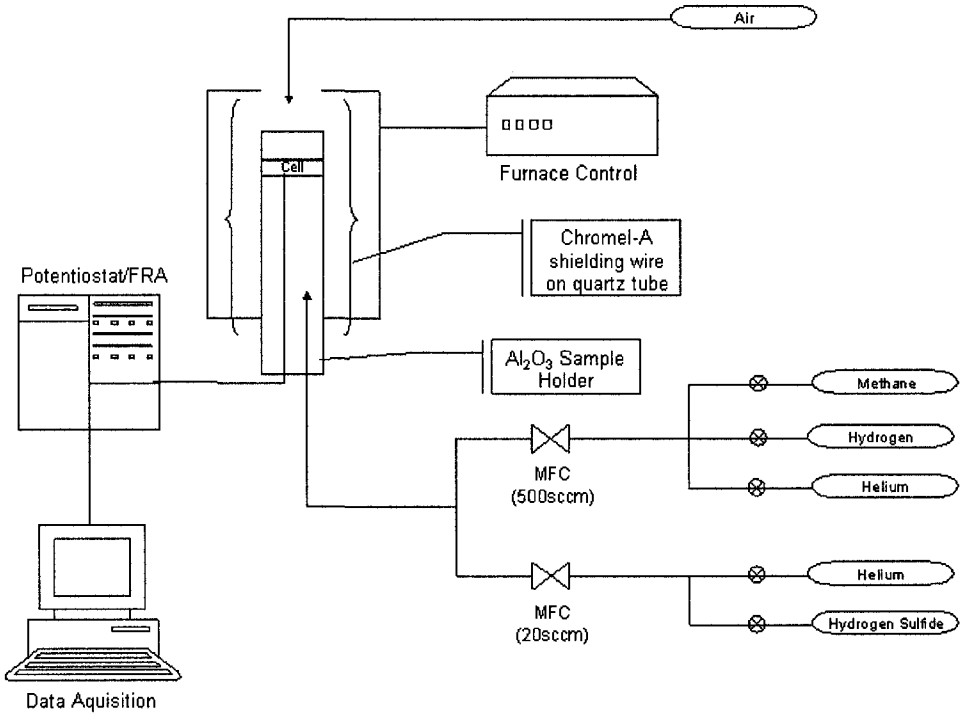

Figure 2.6 Overview of experimental set-up used in electrochemical measurements.

In this study a temperature range of 800°C to 1000°C was utilized for electrochemical measurements. However, the working condition most often used was 850°C with a total fuel flow of 50sccm. The decision to use these operating conditions will be examined in the following sections.

2.4.2 Fuel Cell Set-up and Optimization

The cell consisted of an alumina tube on which the test cell was placed. The ceramic sample holder is schematically shown in Figure 2.7.

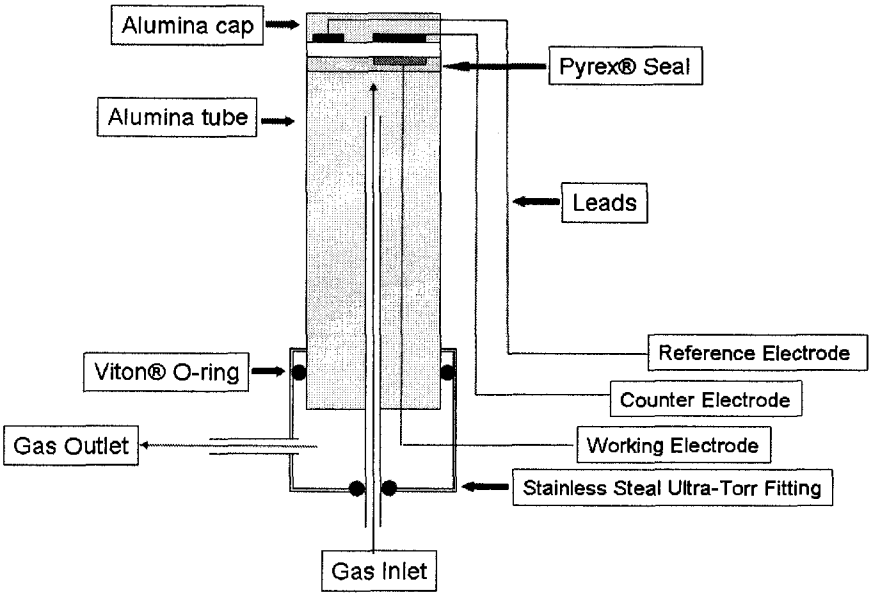

Figure 2.7 Schematic of the fuel-cell set up and holder.

Glass was used to seal the edge of the alumina tube to the YSZ surface by heating to 950°C and using an alumina cap as a weight. Platinum mesh was used as the current collector and was connected to the potentiostat via platinum wires which ran down the alumina tubing to the potentiostat.

2.4.2.1 Current Collection

The choice of current collector and its incorporation into a SOFC is important to develop systems with high power output and/or to study the electrochemical behavior of an electrode material. The current collector ideally should not participate chemically or electrochemically in the electrode reaction and the overall cell resistance should not be significantly affected by any current constriction caused by inadequate contact between electrode and current collector.

Generally two main types of current collectors are used: paste and mesh. Paste can easily be coated onto the electrode and the contact area between current collector and electrode can

be determined with accuracy. Mesh current collectors are reusable but significantly affect polarization losses, where current constriction decreased with increased mesh contacts.[20] However, paste current collectors have been shown to modify the physical structure of the electrode over time by decreasing the number of reaction sites.[21]

To address the aforementioned concerns, the current collector used in these systems was a Pt-10%Rh mesh with a 0.003 inch wire diameter (Unique Wire Weaving Co.) embedded into the electrodes. Embedding the mesh relieves the concerns associated with contact resistance however it made it difficult to ensure flat electrode surfaces across the area. Since the active thickness of fine Ni-YSZ cermet anodes have been demonstrated to be in the range of 10μm[22], while the rest of the anode acts as a current carrier, the regularity of the surface was not taken into consideration since the electrode cross-sections were consistently above 20μm prior to embedding the mesh.

To embed the mesh, 0.15g of anode paste made of a mixture of 1g anode powder, 0.2ml Triton-X ® and 0.5ml water was drop coated onto a green YSZ disk. Once the paste was dry, the mesh was placed on top of the dried anode and another layer of anode paste drop coated over the mesh and allowed to dry. This 'anode-mesh-anode' was co-sintered with the YSZ at 1400°C.

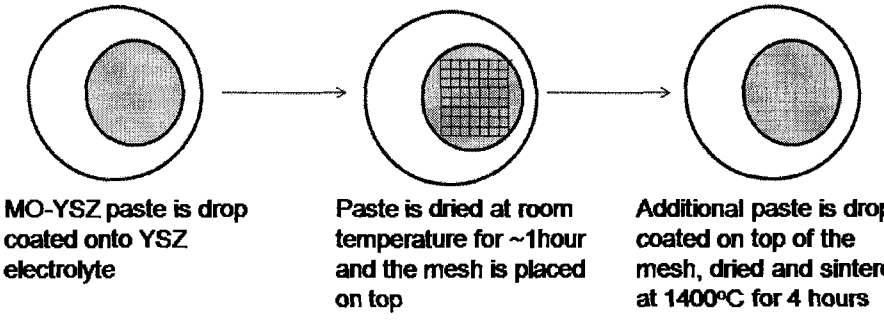

Figure 2.8 A schematic describing the general procedure for embedding the Rh/Pt current collector

Issues related to the electrochemical activation by the mesh were also addressed prior to fuel cell testing. Figure 2.9 shows the current density versus overpotential results for a commercially purchased Ni-YSZ anode (Fuel Cell Materials) and an YSZ 'blank' anode. Both had used the embedded Pt-10%Rh mesh as the current collector. Large differences in current densities are observed for each fuel cell.

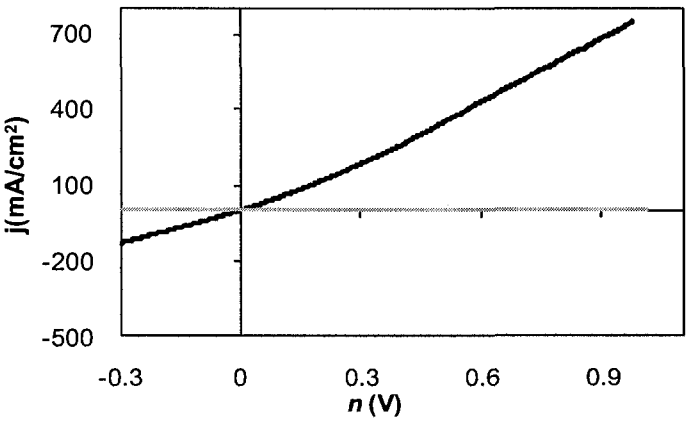

Figure 2.9 Current density versus overpotential (without iR_s compensation) curves for — Ni-YSZ electrode and ---- YSZ electrode with embedded Pt-10%Rh current collector.

The anode consisting of YSZ and Pt-10%Rh mesh exhibited a maximum current density of ~4 mA/cm^2, while the anode utilizing commercial Ni-YSZ exhibited current densities as high as 750 mA/cm^2. The low current densities observed in the 'blank' anode show the current contributions from the embedded mesh are minimal and therefore were not taken into consideration during electrochemical analysis. This is attributed to the small TPB area between mesh, gas and YSZ.

2.4.2.2 Electrolyte

The high ionic conductivity of 8mol% yttria-stabilized zirconia has resulted in its use as the most common SOFC electrolyte. Although it is not the best oxygen ion conductor, with bismuth oxide compositions showing the highest conductivity, its low cost, ease of processing and low electronic conductivity make it a very desirable electrolyte.[23]

To improve the overall efficiency of SOFC's each component must be optimized. In the case of YSZ electrolytes, the ionic and mechanical properties may be enhanced by increasing the density and decreasing grain sizes after sintering. Recent commercial materials research has focused on producing ultra-fine YSZ powders which sinter to high density

In this work, two types of commercial YSZ were used. A 200μm pre-sintered YSZ sheet (Marketech International) was initially utilized, while most of the electrochemical testing was performed with a 500μm 8mol% YSZ produced by Tosoh Corporation of Japan. This electrolyte was made by uniaxially pelleting 1.5g of the Tosoh YSZ to a pressure of 52 MPa to form 30 mm disks and sintering to a temperature of 1400°C. The Tosoh YSZ was chosen

as the preferred electrolyte since it is one of the most commonly used electrolytes in SOFC research and reaches full sintered density by 1400°C and exhibits low grain boundary resistance.[17]

2.4.2.3 Cathode and Reference Material

Strontium doped $LaMnO_3$ (LSM) is currently the preferred cathode material in SOFCs because of its high electronic conductivity in oxidizing atmospheres. In this work, a mixture of 70%w/w LSM (NexTech Materials) and 30%w/wYSZ (Tosoh) was used as the fuel cell cathode and reference electrode to ensure high electronic and ionic conductivity. The mixture also minimized thermal expansion mismatches between the electrodes and electrolyte.

Concerns regarding the chemical compatibility of LSM with YSZ exist since solid state reactions between La, Mn and Sr with ZrO_2 are prevalent at high temperatures. Fabrication temperature was limited to 1150°C in this work to minimize Mn, La and Sr migration into the YSZ.[24]

2.4.2.4 Fuel Flow and Temperature

Optimization of fuel flow was performed at 850°C using a Ni-YSZ anode sintered to 1400°C onto a pre-sintered YSZ electrolyte. Figure 2.10 shows the relationship between cell performance and changes in H_2 flow. The flow was varied from 5-60sccm and showed only a slight increase in the OCV (0.99-1.04V) and no significant change at higher current densities. Although there was no significant change in performance between high and low flows, a flow 50sccm was chosen.

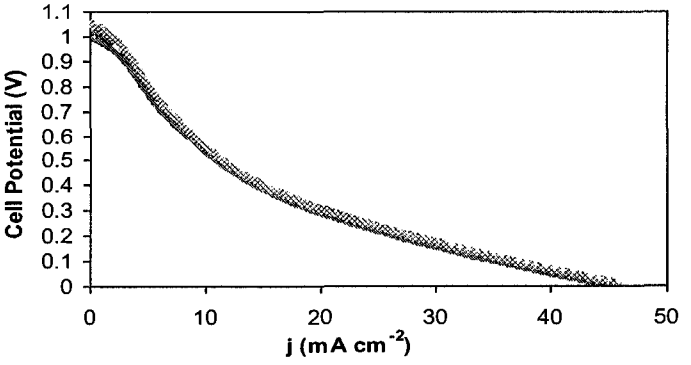

Figure 2.10 Cell potential versus current density for Ni-YSZ/YSZ/LSM-YSZ SOFC with varying H_2 flows. —— 5sccm —— 10sccm - - 15sccm - - 20sccm ····· 40sccm ····· 60sccm.

Interestingly no limiting current is observed, suggesting diffusion control process is not reached. However, at low cell potentials (high current load) the possibility of mixed control is likely. Unlike H_2 flow, temperature had a very significant affect on performance as shown in Figure 2.11. Temperature variations were tested using a standard flow of 15sccm H_2. Generally, the OCV decreased with temperature as expected. As an exception, the OCV increased slightly at 950°C and may be due to Nerstian effects. Despite the obvious increase in performance with higher temperatures, the most frequently used temperature was 850°C. This is below the optimal working temperature of the YSZ based SOFC. This lower value was chosen based on the expected stability problems of the electrodes at higher temperatures.

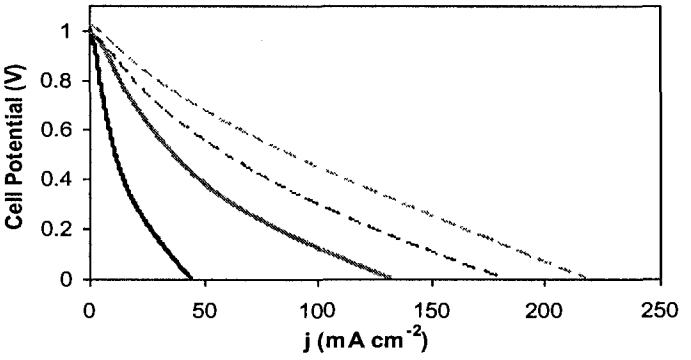

Figure 2.11 Cell potential versus current density for Ni-YSZ/YSZ/LSM-YSZ SOFC at various temperatures H_2 flowing at 15sccm. —800°C —850°C – –900°C – – 950°C.

Other temperatures were utilized during the kinetic studies. These tests were conducted between 800°C to 1000°C in intervals of 50°C.

2.4.2.5 Electrochemical History

When comparing the performance of various anodes, the electrochemical history of the system may change the electrode kinetics, particularly after long polarizations. Figure 2.12 shows the observed increase in performance for a fuel cell run continuously under load for various amounts of time. The fuel cell performance was enhanced, suggesting a dependence on electrochemical history.

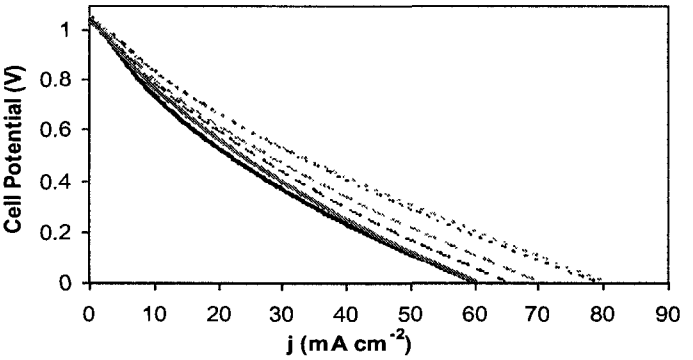

Figure 2.12 Cell Potential versus current density for Ni-YSZ/YSZ/LSM-YSZ system at various times under load. —— t=0hrs —— t=1hr – – t=3hrs – – t=5hrs ····· t=10hrs ····· t=15hrs

The enhancement of the electrode kinetics has tentatively been described as the spill-over effect. Adsorbed layers of oxide ions on the electrode surface change the catalytic properties of the metal surface. Due to the applied potential the oxide ions are pumped from the electrolyte to the surface where a layer of adsorbed ions is formed. This phenomenon is expressed in two ways: in the increase in overall reaction rate and in an increased capacitance.[25]

Due to the time/electrochemical history dependence on SOFC performance each fuel cell was required to undergo the equivalent electrochemical history. That is, each fuel cell was run using the exact same sequence of programs with each program lasting at least 15hrs.

2.4.2.6 Geometric Requirements

To study the performance and characteristics of a single electrode, such as the anode, the individual overpotential must be measured independently by performing half-cell measurements. This is accomplished by utilizing a reference electrode. This requires a cell with three-electrode geometry, where the working electrode is the electrode under study, the counter electrode is a current carrying electrode and the reference electrode is used for controlling and measuring the potential of the working electrode and does not carry any appreciable current. During an electrochemical experiment, it is necessary to monitor the potential of the working electrode versus the reference electrode. This is performed by the potentiostat. A potential difference is applied between the working and reference electrodes and the potentiostat adjusts the potential of the counter electrode to maintain this potential

difference. Current is measured between the working and counter electrodes. A general schematic is shown in Figure 2.13.

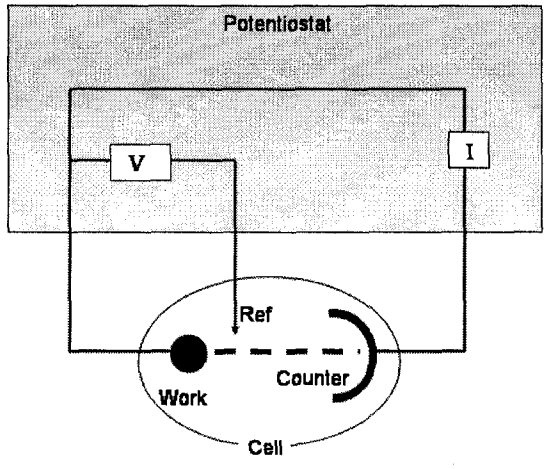

Figure 2.13 Schematic representation of the working, counter and reference electrode connections to the potentiostat.

Positioning of the electrodes on solid electrolytes to isolate the working electrode from the counter electrode is particularly important. To measure specific area resistances of the working electrode a uniform current density at this electrode is assumed.

$$R_p \equiv \frac{\eta}{i} = \frac{\phi_{WE} - \phi_{RE}}{i - R_s} \qquad (2.19)$$

where R_p is polarization resistance, η is overpotential, i is current and R_s is the series resistance. If a uniform current density is not present, different regions will experience different polarizations and the measured overpotential will be either over- or underestimated. Placement of the reference electrode as far from the working electrode as possible should also be considered to ensure no lines of equipotential enter the reference electrode.[26-28] In this work, the reference electrode was placed 4mm from the cathode, approximately 8 times the electrolyte thickness.

Both numerical and experimental findings suggest that ideal SOFC three-electrode geometry would include a symmetric cell where the counter and working electrodes are symmetrically opposed to one another with the reference electrode as far away from them as

possible. Furthermore, by increasing the electrolyte thickness, errors associated with electrode misalignment would be minimized. However, a compromise regarding electrolyte thickness is needed since it must be thin enough to allow reasonable current densities and thick enough to keep electrode alignment errors minimal.

Numerical evaluations suggest there is very little room for error when it comes to electrode alignment. Misalignment of the working and counter by as little as 0.5 electrolyte thicknesses resulted in a 20% error in polarization resistances.[29] Therefore, for an electrolyte thickness of 500μm, only a 50μm misalignment is endurable. Other numerical studies found similar results, where a misalignment of working and counter electrodes of 1mm on a 500μm electrolyte led to errors as high as 70%.[30]

However, experimental findings show a significant amount of misalignment can be tolerated as long as the electrolyte is thicker than 200μm. *Jiang et al.* found that a misalignment of 0.5mm on a 200μm electrolyte resulted in separation of anodic and cathodic overpotentials with minimal error and only cells with YSZ electrolytes <200μm in thickness exhibited significant error.[31]

Since this work concentrated on obtaining electrochemical information regarding the anode, a three-cell test geometry was used. Based on the aforementioned findings the fuel cell was fabricated based on a planar cell set-up where the cathode was coated on the YSZ disk symmetrically opposite the sintered anode, while the reference electrode was approximately 4mm to the side of the cathode (Figure 2.7). After sintering, the YSZ electrolyte was 0.5mm thick and the area of the electrodes were 0.4cm^2 for the anode and cathode and 0.2cm^2 for the reference electrode. H_2 flowed at a rate of 50sccm and air was used as the oxidant. Impedance spectra obtained for the anode, cathode and whole cell at OCV are given in Figure 2.14.

Although impedance spectra cannot fully examine the errors with accuracy issues associated with over- or underestimations of specific resistances, a survey of the ohmic resistance between cathode to reference and anode to reference can assess the split in this resistance, which ideally is 50-50%. In our case the split is 57-42% between cathode-reference and anode-reference. Additionally, the area specific resistance of the anode ($R_p^A = 2.0\Omega \cdot cm^2$) is similar to that of the cathode ($R_p^A = 1.5\Omega \cdot cm^2$) suggesting cross-talk from the cathode will introduce relatively small errors in the anode overpotential measurements. Sizable discrepancies between area specific resistances of the electrodes are

undesirable since the electrode with the smallest resistance can be considered a 'problem' electrode. Measurements on this electrode cannot be performed without affecting the performance of the whole cell.[32]

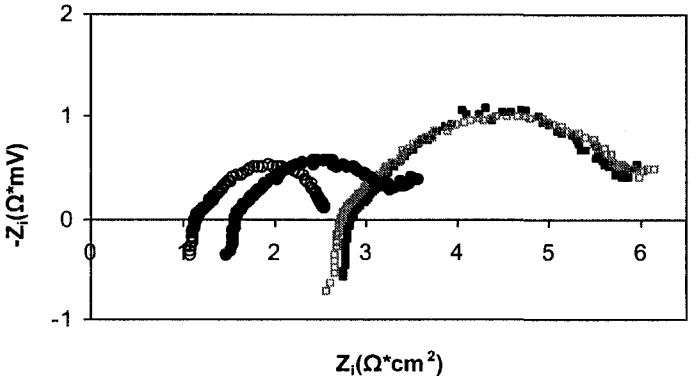

Figure 2.14 Impedance spectra at OCV for (○)anode (Ni-YSZ), (●)cathode (LSM), (■)whole cell and (□)sum of working & counter at 850°C for the three-cell test geometry typically used in this work.

To further examine the reliability of the cell design, DC experiments where the anode and cathode responses versus the reference electrode were compared to that of the full cell response. The measured full cell potential was compared to the calculated cell potential which was calculated according to the following equation

$$E_{cell} = E_{OCP} - (\eta_a + \eta_c) - i(R_a + R_c) \quad (2.20)$$

Where E_{cell} is the calculated cell potential, E_{OCP} is the open circuit voltage, η_a is the measured anodic overpotential of the anode and η_c is the measured cathodic overpotential of the cathode at a particular current i. R_a and R_c are the series resistances related to the anode and cathode respectively. All these measurements were obtained at 850°C in 50 sccm H_2 using a three electrode geometry.

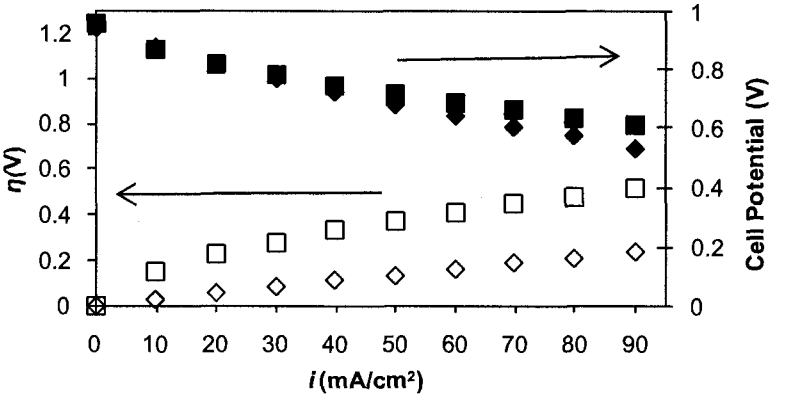

Figure 2.15 η_a and η_c measured against reference electrode and the comparison of the measured cell potential and those calculated based on measured iR_s and η losses at 850°C. (□)η_a (◊)η_c (■) measured E_{cell} (♦) calculated E_{cell}.

Figure 2.15 shows η_a and η_c measured against the reference and the comparison of the measured (using a two-electrode geometry) and calculated cell potentials. The calculated cell potential versus the real cell potential was within 15% relative error at anode overpotentials of 400mV.

2.4.2 Electrochemical Analysis

Two types of measurements are considered; direct current and alternating current measurements. After initial preparation and mounting of the single cell, a minimum OCV of 1.0V was required to continue electrochemical testing. All electrochemical measurements were taken using a VoltaLab 40 or 80 (Radiometer Analytical). Impedance measurements were taken over a frequency range of 100kHz-250mHz or 10mHz from OCV to an overpotential of 400mV at 100mV intervals. DC current-voltage measurements were conducted using a potential scan rate of 0.25mV/s or 2mv/s. The slower rate was used to allow the system to reach quasi-steady state conditions for kinetic analysis.

2.4.2.1 Direct Current (DC) Analysis

Rates of electrochemical reactions are influenced by potential and are measured in terms of current densities. For a simple electrochemical reaction:

$$O + ne^- \underset{\leftarrow}{\rightarrow} R$$

A potential negative to equilibrium potential will push the reaction left where oxidation is favoured, resulting in a positive (cathodic) net current. A positive potential will push the

reaction right, resulting in a negative (anodic) net current. At equilibrium, the rates of the forward and back reaction are equal, resulting in no net current.

$$i_{net} = \overleftarrow{i} + \vec{i} \quad (2.21)$$

$$i_{net} = nF\overleftarrow{k}_o[R]\exp\left(\frac{\alpha_a nFE}{RT}\right) + nF\vec{k}_o[O]\exp\left(\frac{-\alpha_c nFE}{RT}\right) \quad (2.22)$$

$$i_o = nF\overleftarrow{k}_o[R]\exp\left(\frac{\alpha_a nFE^o}{RT}\right) = -nF\vec{k}_o[O]\exp\left(\frac{-\alpha_c nFE^o}{RT}\right) \quad (2.23)$$

By combining Equations 2.22 and 2.23 we obtain

$$i_{net} = i_o\left\{\exp\left(\frac{\alpha_a F\eta}{RT}\right) - \exp\left(\frac{-\alpha_c F\eta}{RT}\right)\right\} \quad \text{where } \eta = E_{FC} - E^o \quad (2.24)$$

Therefore we acquire a term that relates current to the exponential of ovepotential (η) and is the generalized kinetic equation proposed by Erdey-Gruz and Volmer and Butler (See Chapter 2).[33-36] This equation takes into account both the forward and backward reaction directions corresponding to net *i* and the exponential potential dependence of the forward and backward current components through the transfer coefficients (α) and is valid in the region of activation control, where there are no mass transport effects and changes between E and E^o are due only to activation overpotential. The charge transfer coefficient relates the portion of overvoltage that aids in the cathodic and anodic reactions.

From Equation 2.24, for appreciable positive polarizations, the second term becomes negligible and the expression simplifies to

$$i = i_o\left\{\exp\left[\frac{\alpha_a \eta F}{RT}\right]\right\} \quad (2.25)$$

or

$$\ln i = \ln i_o + b^{-1}\eta \text{ where } b^{-1} = \frac{\alpha_a F}{RT} \quad (2.26)$$

By plotting ln*i* vs η, one may obtain both the anodic exchange current density for a particular reaction and the inverse Tafel slope (referred to as the Lefat slope). Similarly the exchange current density and inverse Tafel for the cathodic reaction may be obtained at appreciable negative polarizations.

Although much information can be gathered by using the above relationship, care must be taken when choosing an appropriate linear region. If it is assumed that the first electron-transfer step of a reaction is rate determining, the high-field region is expected to commence at about 52mV at room temperature. Therefore, at SOFC operating temperatures (~800°C) Tafel at approximately 190mV according to $\frac{RT}{\alpha F}$, and change accordingly at different temperatures. Additionally, passivation and mass transport effects must also be excluded. For the purposes of this study, the linear region began at overvoltages >190mV and spanned approximately 150mV.

2.4.2.2 Alternating Current (AC) Analysis/Impedance Spectroscopy

Impedance may be regarded as a "generalized resistance" and is the term given to $\widetilde{E}/\widetilde{i}$ for systems other than metallic resistors. Impedance contains two kinds of information; a magnitude (resistance) and a phase angle (the angle by which current leads or lags behind the voltage).

If there is an excitation of an electrochemical cell by a sinusoidal signal (usually voltage)

$$\widetilde{E} = \bar{E}\sin(\omega t) \quad (2.27)$$

the current generated is typically also sinusoidal and of the same frequency however, different in amplitude and phase.

$$\widetilde{i} = \bar{i}\sin(\omega t + \phi) \quad (2.28)$$

where $\widetilde{E}$ and $\widetilde{i}$ are the oscillating voltage and current, $\bar{E}$ and $\bar{i}$ are the amplitude of voltage and current, $\omega = 2\pi f$ is the angular frequency, ϕ is the phase shift and t is time.

2.4.2.1.1 Resistor

For a resistor,

$$\phi = 0 \quad (2.29)$$

$$Z = \bar{E}/\bar{i} \quad (2.30)$$

and we obtain Ohm's law such as we see when describing the impedance (resistance) of metals.

2.4.2.1.2 Ideal Capacitor

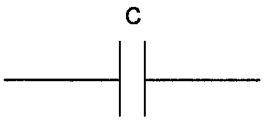

Since an electrode interface exhibits a capacitance, one may relate the charge, q, residing on the plates of the capacitor to the potential across the plates:

$$q = CE \quad (2.31)$$

$$\tilde{i} = \partial q/\partial t = C\partial\tilde{E}/\partial t \quad (2.32)$$

$$\tilde{i} = \omega C\bar{E}\cos(\omega t) = \frac{\bar{E}}{X_c}\sin\left(\omega t + \frac{\pi}{2}\right) \text{ where } X_C = \frac{1}{\omega C} \quad (2.33)$$

Since $\tilde{E}$ and $\tilde{i}$ are regarded as phasors (rotating vectors) the introduction of complex notation is useful. For a capacitive circuit, the $\tilde{E}$ phasor has a $\phi = -\frac{\pi}{2}$ compared to the current

$$\tilde{i} = \frac{\tilde{E}\sin\left(\omega t + \frac{\pi}{2}\right)}{\sin(\omega t)X_c} \quad (2.34)$$

$$\tilde{E} = -jX_c\tilde{i} \quad (2.35)$$

Thus for an ideal capacitor, where the current and potential are out of phase by 90°, replacing $\frac{1}{\omega C}$ by X_c (capacitive reactance) gives an equation similar to Ohm's law, where $-jX_c$ is akin to R and is dependent on frequency and capacitance.

2.4.2.1.3 Ideal Polarizable Electrode

For a resistor and capacitor in series, the circuit representing an ideal polarizable electrode, only capacitive current is flowing upon the change in potential.

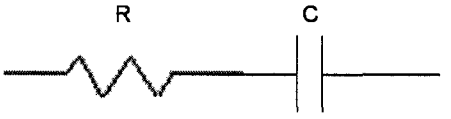

The sum of the voltage drop across each element must sum to the total E.

$$\tilde{E}_{tot} = \tilde{E}_R + \tilde{E}_C \quad (2.36)$$

$$\tilde{E}_{tot} = iR - jX_C\tilde{i} \quad (2.37)$$

$$\tilde{E}_{tot} = \tilde{i}(R - jX_C) \quad (2.38)$$

$$\tilde{E}_{tot} = \tilde{i}Z_{tot} \quad (2.39)$$

where $Z_{tot} = R - jX_C$ is the impedance and has a real and imaginary component ($Z_{tot} = Z_r + Z_i$). The real part of the impedance is frequency independent and the imaginary part approaches zero at high frequencies. If the imaginary component of impedance was plotted against the real component, the following Nyquist plot would result.

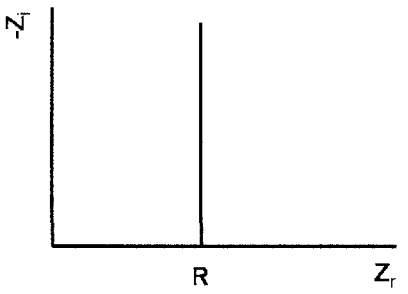

Figure 2.16 Nyquist impedance representation for a series RC connection for an ideally polarized electrode.

2.4.2.1.4 Irreversible Oxidation-Dependant on Potential

In real electrode processes, both capacitive and faradaic currents are involved. The general expression for Faradaic current is

$$i_f = f(E, C_{i\vartheta}, \theta_i) \quad (2.40)$$

where Faradaic current is a function of potential (E), concentration of all species at the surface, ($C_{i\vartheta}$) and surface coverage of species i (θ_i).

The general expression for oscillating Faradaic current is

$$\tilde{i}_f = \left(\frac{\partial f}{\partial E}\right)\tilde{E} + \sum_i \left(\frac{\partial f}{\partial C_{i\theta}}\right)_{E, C_{j,j\neq i}, \theta_k} \tilde{c}_{i,\theta} + \sum_i \left(\frac{\partial f}{\partial \theta_k}\right)_{E, c_j, \theta_{j,j\neq k}} \tilde{\theta}_k \quad (2.41)$$

where the first term represents potential dependence, the second term mass transfer dependence and the third surface coverage dependence.

For an irreversible reaction dependant only on potential, the oscillating Faradaic current is expressed as

$$\tilde{i}_f = \left(\frac{\partial f}{\partial E}\right)\tilde{E} \quad (2.42)$$

Since the steady state current density is

$$\bar{i}_f = nFk\exp\left(\frac{\alpha_a F\bar{E}}{RT}\right) \quad (2.43)$$

the oscillating current density is

$$\tilde{i}_f = \frac{\alpha_a F^2 nk}{RT}\exp\left(\frac{\alpha_a F\bar{E}}{RT}\right)\tilde{E} \quad (2.44)$$

$$R_{ct} = \frac{\tilde{E}}{\tilde{i}_f} = \frac{1}{\frac{nk\alpha_a F^2}{RT}\exp\left(\frac{\alpha_a F\bar{E}}{RT}\right)} \quad (2.45)$$

where the charge transfer resistance for an irreversible reaction is dependent on $\bar{E}$ and T. To calculate impedance, the sum of the faradaic and charging currents is taken into account.

$$\tilde{i}_{tot} = \tilde{i}_f + j\omega C\tilde{E} \quad (2.46)$$

$$\tilde{i}_{tot} = \tilde{E}\left(\frac{1}{R_{ct}} + j\omega C\right) \quad (2.47)$$

$$\frac{\tilde{E}}{\tilde{i}_{tot}} = \frac{R_{ct}}{1 + j\omega R_{ct} C} \quad (2.48)$$

Therefore the total drop in potential across each element, including uncompensated resistance from the electrolyte is

$$\tilde{E}_{tot} = \tilde{i}_{tot} R_e + \tilde{E} \quad (2.49)$$

$$Z_{tot} = \frac{\widetilde{E}_{tot}}{\widetilde{i}_{tot}} = R_e + \frac{R_{ct}}{1 + j\omega R_{ct} C} \qquad (2.50)$$

represented by the following equivalent circuit (Figure 2.17.a) and Nyquist diagram (Figure 2.17.b).

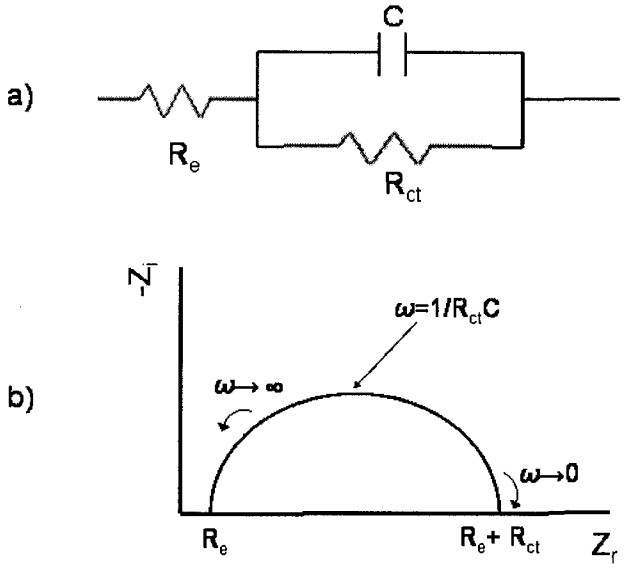

Figure 2.17 (a) Equivalent Circuit and (b) Nyquist impedance representation for an electrode reaction with double layer capacitance in parallel with a Faradaic charge transfer resistance.

For an irreversible reaction with no mass transport limitations, the impedance is described by an uncompensated/electrolyte resistance as well as a charge transfer resistance in parallel with a capacitance.

2.4.2.1.5 Irreversible Oxidation-Dependant on Potential and Mass Transfer

The same treatment can be applied in the case of an irreversible reaction dependant on potential and mass transfer where the resulting impedance is represented by the following equation,

$$Z_{tot} = \frac{\widetilde{E}_{tot}}{\widetilde{i}_{tot}} = R_e + \frac{R_{ct} + Z_d}{1 + j\omega C\left(R_{ct} + Z_d\right)} \qquad (2.51)$$

equivalent circuit (Figure 2.18.a) and Nyquist plot (Figure 2.18.b).

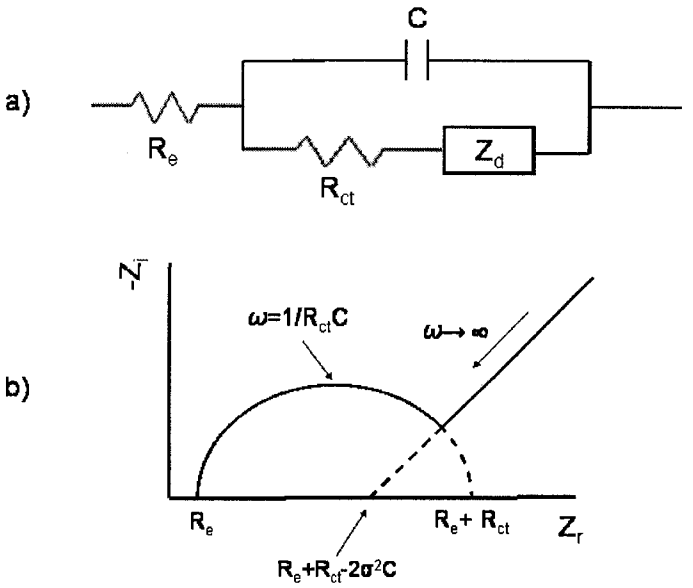

Figure 2.18 (a) Equivalent Circuit and (b) Nyquist impedance representation for an electrode reaction with double layer capacitance in parallel with a Faradaic charge transfer resistance and a diffusional impedance.

where

$$Z_d = \frac{R_{ct} k\delta}{D\hat{\theta}'(0)} \exp\left(\frac{\alpha F\bar{E}}{RT}\right) \qquad (2.52)$$

is the diffusion impedance and is obtained using Ficks first law of diffusion, where D is the diffusion coefficient, $\hat{\theta}'(0)$ is the surface coverage and δ is the diffusion layer thickness.

2.4.2.1.6 Impedance of SOFC Anodes

Figure 2.19 shows a typical impedance curve obtained during the course of these experiments on Ni-YSZ anodes. There are two distinct arcs at the high- and mid- frequency range and a third element at low-frequencies. The Ni-YSZ impedance spectra are similar to that expected for an irreversible reaction with potential and mass transfer effects examined in the previous section, with one additional arc at high-frequencies. Co-YSZ anodes also exhibited the same spectra except the low frequency element in the impedance spectra were observed as a third arc as opposed to a straight line. Interpretation of these responses to temperature and overpotential will be discussed in subsequent chapters.

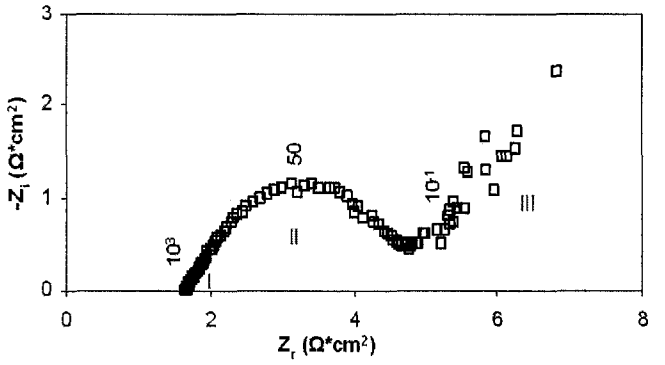

Figure 2.19 Typical impedance spectra obtained for Ni-YSZ system at 850°C and 50sccm flow H_2 at OCV.

The model most commonly used to describe each arc/electrode process in SOFC anodes is a serial equivalent circuit (EC) model ($LR_s(RQ)_1(RQ)_2(RQ)_3...(RQ)_n$) where L is the inductance, R is a resistance, and Q is a constant phase element (CPE) given as $Q = Y_o(j\omega)^n$, where Y_o is the admittance, j the imaginary unit, ω the angular frequency and n is the frequency power (Figure 2.20.a). In the case of inhomogeneous surfaces, such as porous surfaces, the capacitive line shows deviation from an ideal response which is related to the inhomogeneous distribution of current caused by surface irregularities. Furthermore, when a CPE is present in an equivalent circuit resulting in a semicircle, the inhomogeneties are expressed as a depressed arc.[37,38]

In the serial equivalent circuit model it is assumed that each relaxation process in a spectrum is related to exactly one transport or reaction process. Such simple serial analysis implicitly assumes the current passes identical sample regions for all frequencies thereby assuming the current lines are frequency independent. However, the frequency dependence of current lines may result in additional semicircles in the spectrum and therefore cannot simply be understood in terms of serial EC models. As a result, an equivalent circuit for interpreting impedance data was proposed by *Fleig et al.* and included the possibility of considerable current constriction which would be observable in the spectrum (Figure 2.20.b). A simplified EC was proposed for conditions similar to those found in SOFC set-ups and is a parallel EC consisting of an electrode impedance ($R_u[C_2 (R_3(Z_{elect})]$) and an uncompensated resistance (Figure 2.20.c). The simplified model proposed by *Fleig et al.* was used to model impedance data obtained in this work.[39-42] Z_{elect}, the impedance due to electrode kinetics, is expected to be dependent on voltage and mass transfer and may be represented by the EC

shown in Figure 2.18.a, with a CPE instead of an ideal capacitor, to account for the porous anode structure.

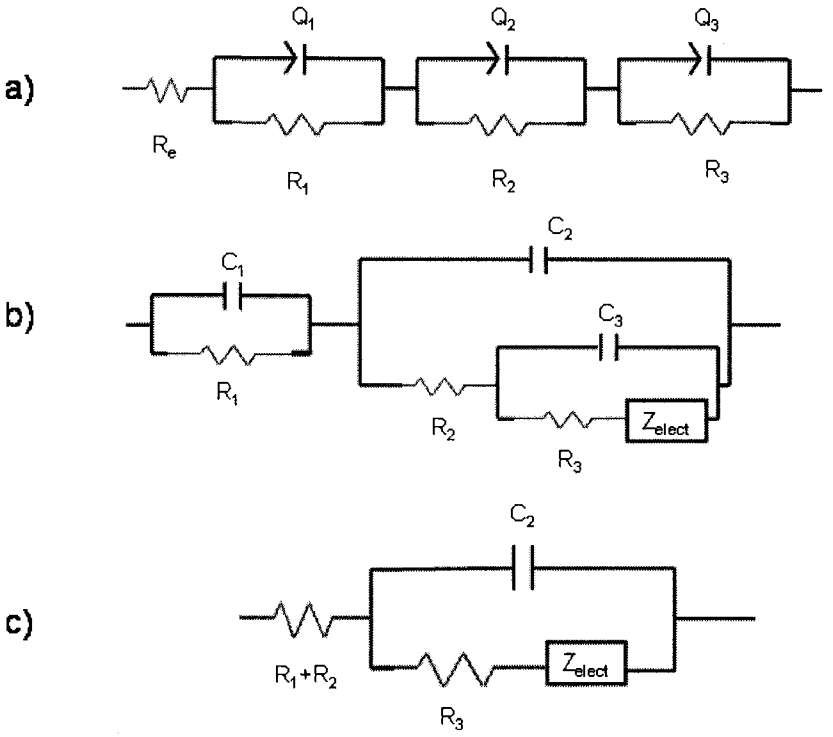

Figure 2.20 a) Serial Equivalent Circuit model. EC's proposed by *Fleig et al.* describing impedance spectra obtained from b) solid electrodes c) simplified EC for solid electrodes.

2.5 SOFC Reproducibility

Reproducibility of electrode performance was analyzed using 6 different anode materials. The anodes consisted of a metal or metal mixture of Ni/Co or Ni/Cu and YSZ. Each of the materials was used to fabricate 3 identical fuel cells, for a total of 18 test runs. The anodes were run in H_2 with a flow rate of 50sccm at 850^{O}C and exchange current densities were determined by using the high field approximation of the Butler-Volmer equation (see Chapter 4). The DC current-voltage measurements were conducted using a potential scan rate of 2mV/s. The linear segment used to determine i_o was between $\eta = 400 - 550mV$ and generally ranged 0.5 decades of current. Figure 2.21 shows an example of iR_s corrected DC measurement for a Ni-YSZ anode and the Tafel fit.

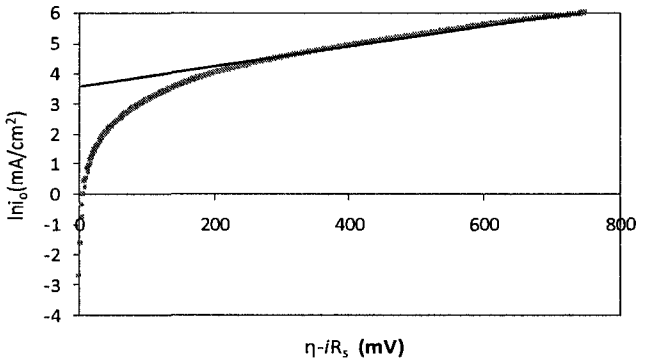

Figure 2.21 Example ln(current)-potential relations on sample Ni-YSZ used to determine exchange current densities for samples in H_2 atmospheres. The potential scan rate was 2mV/s.

The i_os for each type of fuel cell was compared to gauge the reproducibility of fuel cell fabrication. Figure 2.22 shows the average i_o calculated from the three runs and the standard deviation of this value.

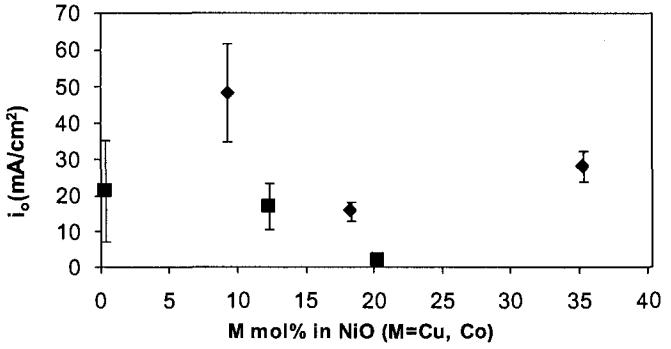

Figure 2.22 Exchange current densities for (■) $Ni_{1-x}Cu_x$-YSZ mixtures and (♦)$Ni_{1-x}Co_x$-YSZ mixtures.

The average relative standard deviation was 33% for all anodes. The smallest deviation is observed with anodes containing higher levels of Co or Cu in the metallic phase of the composite. Anodes where the metallic phase consisted mostly of Ni showed low concordance between tests. It is yet unclear whether the low reproducibility of the anodes containing a large amount of Ni was a direct result of inherent inhomogeneities at the atomic/molecular scale, pore/particle scale, electrode thickness or a combination thereof. Due to these results, a difference of at least 50% was deemed significant when comparing between anode materials.

When testing anode responses in various fuel streams, the fuel cell was first tested in H_2 and a ratio of i_o's were employed (i_{ogas}/i_{oH2}), where the ratio represented the increase in performance of this fuel cell in a gas with respect to its performance in hydrogen.

2.6 Conclusions

In this chapter a detailed analysis of each characterization technique along with the assumptions and their appropriateness was discussed. Quantification was performed by XRF and XRD due to the concentration and chemical limitations associated with Visible and IR spectroscopy.

XRD and gas adsorption were used to calculate crystallite and particle sizes of individual phases in the composites. Since both these techniques assume spherical geometry, SEM was used to elucidate general particle shapes and sizes. The information gathered from all three techniques is necessary to examine particle morphologies in composite materials.

Fuel cell operating conditions, including temperature and flow rates were set to optimize electrode performance. The current collector was embedded into the electrodes without any appreciable addition to electrode performance. Electrolyte and cathode/reference materials were not changed throughout the course of experimentation.

To ensure accuracy during polarization measurements, a symmetric test design with the reference electrode far away from the cathode and anode and a 500um thick electrolyte was used. AC and DC experiments show reasonable separation between electrode polarizations for this symmetric planar cell design.

References

(1) Skoog, D. A.; Holler, F. J.; Nieman, T. A. *Principles of Instrumental Analysis*, 5 ed.; Harcourt Brace & Company: Orlando, 1998.

(2) Burattin, P.; Che, M.; Louis, C. *J. Phys. Chem.* **1997**, *101*, 7060.

(3) Burattin, P.; Che, M.; Louis, C. *J. Phys. Chem.* **1998**, *102*, 2722.

(4) Soler-Illia, G. J. d. A. A.; Jobbagy, M.; Regazzoni, A. E.; Blesa, M. A. *Chem. Mater.* **1999**, *11*, 3140.

(5) Song, Q.; Tang, Z.; Guo, H.; Chan, S. *J. Power Sources* **2002**, *112*, 428.

(6) Rostrup-Nielsen, J.; christiansen, L. *App. Catal. A.* **1995**, *126*, 381.

(7) Tatsumi, T.; Koyano, K. A.; Shimizu, Y. *App. Catal. A* **2000**, *200*, 125.

(8) Friebe, P.; Bogdanoff, P.; Alonso-Vante, N.; Tributsch, H. *J. Catal.* **1997**, *168*, 374.

(9) Inc, M. D. MDI Jade 6.1; Material Data Inc., 2002.

(10) Williamson, G.; Hall, W. *Acta Metall.* **1953**, *1*, 22.

(11) Brunauer, S.; Emmett, P.; Teller, E. *J. Am. Chem. Soc.* **1938**, *60*, 309.

(12) Shull, C. *J. Am. Chem. Soc.* **1948**, *70*, 1405.

(13) Boer, J. d.; Linsen, B.; Plas, T. V. d.; Zondervan, G. *J. Catal.* **1965**, *4*, 649.

(14) Boer, J. d.; Lippens, B.; Linsen, B.; Broekhoff, J.; Heuvel, A. v. d.; Osinga, T. J. *J. Coll. Interface Sci.* **1965**, *21*, 405.
(15) Halsey, G. *J. Chem. Phys.* **1948**, *16*, 931.
(16) Su, H.; Johnson, D. L. *J. Am. Ceram. Soc.* **1996**, *79*, 3199.
(17) Gibson, I.; Dransfield, G.; Irvine, J. *J. Mater. Sci.* **1998**, *33*, 4297.
(18) Tietz, F.; Dias, F. J.; Simwonis, D.; Stover, D. *J. Eur. Ceram. Soc.* **2000**, *20*, 1023.
(19) Instruments, M. "MKS Type 1179A and 2179A Mass-Flo$^{(R)}$ Controller and Type 179A Mass-Flo Meter Instruction Manual," MKS Instruments, 2000.
(20) Jiang, S.; Love, J.; Apateanu, L. *Solid State Ionics* **2003**, *160*, 15.
(21) Guillodo, M.; Vernoux, P.; Fouleier, J. *Solid State Ionics* **2000**, *127*, 99.
(22) Brown, M.; Primdahl, S.; Mogensen, M. *J. Electrochem. Soc.* **2000**, *2*, 475.
(23) Singhal, S. C.; Kendall, K. *High temperature solid oxide fuel cells*; Elsevier Ltd: New York, 2003.
(24) Mihn, N. Q. *J. Am. Ceram. Soc.* **1993**, *76*, 563.
(25) Kek, D.; Mogensen, M.; Pejovnik, S. *J. Electrochem. Soc.* **2001**, *148*, A878.
(26) Nagata, M.; Itoh, Y.; Iwahara, H. *Solid State Ionics* **1994**, *67*, 215.
(27) McIntosh, S.; Vohs, J.; Gorte, R. *J. Electrochem. Soc.* **2003**, *150*, A1305.
(28) Krishnan, V. V.; McIntosh, S.; Gorte, R. J.; Vohs, J. M. *Solid State Ionics* **2004**, *166*, 191.
(29) Winkler, J.; Hendriksen, P.; Bonanos, N.; Mogensen, M. *J. Electrochem. Soc.* **1998**, *145*, 1184.
(30) Chan, S.; Chen, X.; Khor, K. *J. App. Electrochem.* **2001**, *31*, 1163.
(31) Jiang, S. *J. Appl. Electochem.* **2004**, *32*, 1045.
(32) Boer, B. d. SOFC Anode: Hydrogen oxidation at porous nickel and nickel/yttria stabilised zirconia cermet electrodes. PhD Thesis, University of Twente, 1998.
(33) Erdey-Gruz, T.; Volmer, M. *Z. Phys. Chem. A.* **1930**, *150*, 203.
(34) Erdey-Gruz, T.; Wick, H. *Z. Phys. Chem. A.* **1932**, *162*, 53.
(35) Butler, J. *Trans. Faraday Soc.* **1923**, *19*, 729.
(36) Butler, J. *Trans. Faraday Soc.* **1932**, *28*, 379.
(37) Armstrong, R.; Burnham, R. *J. Electroanal. Chem.* **1976**, *72*, 257.
(38) Leibig, M.; Halsey, T. C. *Electrochim. Acta* **1993**, *38*, 1985.
(39) Fleig, J.; Maier, J. *J. Electrochem. Soc.* **1997**, *144*, L302.
(40) Fleig, J.; Pham, P.; Sztulzaft, P.; Maier, J. *Solid State Ionics* **1998**, *113-115*, 739.
(41) Fleig, J.; Maier, J. *J. Electroceram.* **1997**, *1*, 73.
(42) Fleig, J. *J. Electroceram.* **2004**, *13*, 637.

3. Chemically Prepared SOFC Anodes

Abstract

Preparation of metal-electrolyte precursors for solid oxide fuel cells represents a highly complex chemical process in which a metal may form oxides, hydroxides and various complex basic salts as intermediates. In this work, a direct relationship between the precipitation agent, calcination process, final composition, particle sizes, sinterability and solid oxide fuel cell (SOFC) performance for nickel, copper and cobalt based anode materials was established. Nickel, copper and cobalt yttria stabilized zirconia (Ni-YSZ, Cu-YSZ and Co-YSZ) anode materials were synthesized via hydrolysis of the corresponding chloride solutions with NH_3, NH_3 + NaOH and NaOH as precipitation agents. The formation pathway for the various products by the direct observation of intermediate species throughout the synthesis process was determined. A comparison of the powders indicates the choice of precipitation agent greatly influences the final characteristics. The anodes with a crystalline precursor showed a significant improvement in performance.

3.1 Introduction

SOFC anode microstructure and its affect on polarization is a continuous object of study. Since activation depends on the area of the electrode/electrolyte/gas triple phase boundaries (TPB), the material properties of the anode are of particular interest.[1] Increasing the TPB by decreasing particle sizes of the phases present in the anode is one way to minimize activation polarization.

There are two conduction pathways through the Ni-YSZ anodes: An electronic path through Ni and an ionic one through YSZ. Since the conductivity of Ni is more than five orders of magnitude greater than the conductivity of YSZ at 1000°C, the dominant type of conduction will be electronic, provided the Ni phase is continuous throughout the anode. The electrical conductivity of the Ni-YSZ anode is strongly dependant on nickel content. The threshold between ionic and electrical conductivity is at a Ni content of ~30-40 v/v%.[1-4] For an anode to be electrically conductive the relative amounts of Ni and YSZ must be taken into account. Although the electrical conductivity is influenced by Ni content, other variables such as porosity and grain size have a significant effect on conductivity, influencing polarization losses within the anode.

The threshold between ionic and electronic conductivity is influenced by the contiguity of each constituent component thereby rendering variables such as porosity, pore sizes and particle size distributions important facets of total anode conductivity. For fixed Ni content, electrical conductivity is affected by initial size ratio between YSZ and Ni particles

(d_{YSZ}/d_{NiO}) and increases as the ratio increases.[2,3] Increased conductivity is directly related to surface area of the YSZ component. YSZ with smaller surface area allows Ni particles to more easily cover the surface of YSZ thus, improving Ni particle-to-particle contact.

The electrical behavior of Ni-YSZ anodes is also a function of porosity and pore size distributions.[2,5,6] Increasing the dead volume within the cermet decreases electrical conductivity and may be adequately described by the Bruggeman equation[7]

$$\kappa = \kappa_c (1-f)^{3/2} \quad (3.1)$$

where κ is the effective conductivity of the cermet, κ_c is the bulk conductivity of the conducting phase, and f is the void fraction. By decreasing total pore volume, power generation of SOFC's would be expected to increase.[8] However, a compromise between conductivity and gas permeability must be established since adequate porosity is required so the fuel can reach the TPB.

Anode microstructure not only influences electrical conductivity, but electrochemical reaction rates as well. Physical transport resistances of ions or gas diffusion restrictions due to inadequate porosity are also affected by microstructure. The reaction rate for electrochemical oxidation of hydrogen has been demonstrated to directly correlate with the length of the TPB.[9-11] Increasing the TPB is accomplished by finding appropriate metal, electrolyte and pore content. Numerical analysis by *Tanner et al.* showed that charge transfer resistance is small for relatively thick electrodes with a 'fine' microstructure. The 'fine' microstructure was comprised of fine homogeneously distributed pores with small YSZ features.[11] The TPB can be increased by manipulating the d_{YSZ}/d_{NiO}. *Brown et al.* tested four types of Ni-YSZ electrodes and found the fine structured cermet with the smallest d_{YSZ}/d_{NiO} exhibited the largest TPB and smallest electrode resistance.[9] The work was corroborated by *de Boer.*[12] *Fukui et al.* found anodes with homogeneously dispersed NiO and YSZ particles, where sub-micron NiO particles were covered with finer YSZ particles also resulted in high electrochemical current densities.[13]

Although the final cermet consists of metal and ceramic phases (i.e. Ni-YSZ), the anode precursors are usually in the form of mixed metal oxides (i.e. NiO-YSZ). These precursors are sintered to the electrolyte by high temperature firing and the NiO-YSZ is reduced in the SOFC by hydrogen to make the anode. Since electrochemical performance of M-YSZ

depends so strongly on anode microstructure, preparation of anode precursor powders is particularly important.

Due to the high temperatures required to fire the electrodes to the electrolyte, variables introduced during fabrication must be considered. Firing of electrodes to the electrolyte must be performed to ensure good contact between the two materials. If there is no significant difference between sintering behaviour of the electrolyte and electrode, this technique can produce an anode/electrolyte interface with improved mechanical adherence and conductivity, leading to lower polarization losses at the anode.[3,14] The optimal sintering temperatures of electrolyte and electrodes can vary significantly causing mechanical stresses such as cracking or bending of the electrolyte and anode, rendering the fuel cell unproductive. For electrolyte supported stacks, mechanical stress of the electrolyte is derived from length difference caused by shrinkage variations between the electrolyte and anode.[15] Stress in the electrolyte can be reduced by decreasing this difference, thereby improving anode/electrolyte properties.

Traditionally, mixed metal oxides have been obtained by mechanical mixing of the components or by impregnation of the metal salts in a porous matrix.[6,16] These are simple methods that allow for accurate chemical composition but may lead to inhomogeneities within the anode microstructure, causing separation of metal oxide and YSZ particles during anode processing.[17] Co-precipitation of nickel, yttrium and zirconium by ammonia or buffer solution methods were described as assuring homogeneity and uniform distribution of NiO particles within the matrix by controlling NiO and YSZ particle size distributions, but have been found to have a negative effect on the accuracy of composition.[18,19] The low yield of NiO within the final precipitate was attributed to the formation of nickel-ammonia complexes. Synthesis with NaOH resulted in all of the Ni^{2+} precipitating out as $Ni(OH)_2$ albeit with a large particle size distribution of the final NiO product ranging from nanometer to micrometer scale. Precipitation with NH_3 up to pH 11 followed by NaOH up to pH 13 resulted in complete Ni^{2+} precipitation and particle sizes at the nanometer level for both YSZ and NiO phases.[19] The ability to control particle size at the nanometer level in nickel-based anodes encouraged us to use this methodology to explore other metals which would add complementary properties to the anode. In particular, copper and cobalt which are better suited for hydrocarbon fuels due to their resistance to carbon formation[20,21] have been synthesized by co-precipitation.

Since precipitation of metal hydroxides represents a very complex chemical process in which a metal may form oxides, hydroxides and various complex basic salts[22,23] a detailed study to determine the relationship between synthesis strategies, YSZ phase purity, morphology, sinteractivity and SOFC performance is a necessity. The objective of the work presented in this chapter was to determine the mechanism of precipitation, morphology and SOFC anode performance of Ni-YSZ, Cu-YSZ and Co-YSZ anodes synthesized by gel-precipitation using various precipitation agents. Particle size changes of metal and YSZ before and after sintering were examined and related to SOFC anode performance.

3.2 Experimental

3.2.1 Sample Preparation

YSZ supported metal (M-YSZ) (8-71 wt%) anode materials were prepared by dissolving appropriate amounts of $ZrCl_4$, Y_2O_3 (dissolved in 10ml of 37 wt% HCl) and $NiCl_2 \cdot 6H_2O$, $CuCl_2 \cdot 2H_2O$ or $CoCl_2 \cdot 6H_2O$ (Aldrich) in 165ml of distilled water. The precipitation was achieved through the introduction of a base. Gaseous ammonia (Praxair) was introduced at a constant flow of 65 sccm. Sodium hydroxide (Aldrich) was introduced dropwise as a 2*M* solution. Following precipitation, the product was filtered, washed three times in 500ml of water and dried at 120°C overnight. A portion of dried product was then calcined at either 750°C or 950°C for 2h.

3.2.2 Characterization

The quantities of each metal were obtained using a Philips PW2400/00 X-ray fluorescence (XRF) instrument that was calibrated with a concentration gradient of $NiCl_2$, CuO or Co_3O_4 in a mixture of $ZrCl_4$ and Y_2O_3. Visible spectroscopy (Varian IE) was used to determine the presence of metal-ammonia complexes in solution throughout the precipitation process. Powder composition and crystallite sizes were determined by X-ray diffraction (XRD) (Phillips PW1830) using CuKα radiation with a wavelength of 1.54 Å. The scan range was measured from $2\Theta = 20°$ to 90° at a rate of 0.02°/sec. Crystallite sizes were measured using the Williamson-Hall relationship. Crystalline phases were assigned using the Powder Diffraction File (PDF) database (ICCD, 2001, Dataset 1-51). In addition, a variable temperature XRD attachment (Anton Parr) was used to determine the order of crystallization for the powders. Vibrational characterization of the powders before calcination was determined using ATR-FTIR (Bruker Equinox 55).

Sintering experiments were performed by uniaxially pelleting 500mg of the calcined (750°C) oxide powders with a pressure of 37MPa to form 13mm disks. The green densities of each powder were determined by dividing the mass by the cylindrical volume of the pellet. All of the disks were sintered in air to a temperature of 1500°C at 100°C or 50°C intervals. At each interval, the change in length of diameter of the pellet was recorded with digital calipers at four points on the pellet, approximately every 30°. Sinteractivites were determined by using the general combined-stage sintering model for volume and grain boundary diffusion (Equation 2.16).

BET surface area and average particle sizes of the calcined (750°C) powders were determined after reduction in flowing H_2 (99.9%, Praxair) at 600°C for 2h using a Quantachrome Autosorb 1-C instrument. Average metal particle size was measured by obtaining the active metal surface area via chemisorption experiments with H_2 as vector gas. YSZ particle sizes were obtained by taking the difference between the BET surface area and active metal surface areas and assuming spherical geometry.

Particle size and morphology of the mixed oxide powders were also assessed using scanning electron microscopy (Hitachi S-4800). Low resolution imaging of the electrode/electrolyte cross-section was obtained using a NanoLab7 SEM with Kevex EDX for elemental analysis.

3.2.3 Electrochemical testing of synthesized anodes

The fuel cell was prepared by painting a mixture of 0.2ml Triton X-100 (Research Chemical Ltd) and 0.25g of anode powder onto pre-sintered YSZ sheet (Marketech International) and heating to the anodes' sintering temperature (the temperature of maximum shrinkage) for 4h in air. A 70wt%LSM / 30wt%YSZ mixture was used as the cathode and reference electrode material. The cathode was prepared by painting a mixture of 70wt%LSM / 30wt%YSZ and Triton X-100 onto the electrolyte and sintering to 1100°C.

Open circuit potential and electrochemical impedance measurements were performed in pure hydrogen at 800°C. All electrochemical impedance spectra (EIS) were taken using a VoltaLab 40 (Radiometer Analytical) over a frequency range of 100kHz-10mHz at OCV and using AC sine wave amplitude of 10mV. Equivalent circuit modeling of the data was performed with Zview software.

3.3 Results and discussion

3.3.1 YSZ Stabilization and Co-precipitation with Ni^{2+}, Cu^{2+} and Co^{2+}

Initial attempts to synthesize a dual phase metal oxide-8mol%YSZ (M=Ni, Cu, Co) via co-precipitation resulted in a three phase mixture consisting of metal oxide (M=Ni, Cu or Co), YSZ and monoclinic zirconia ($mZrO_2$). Since a two phase system is desirable, analyses to elucidate the cause of $mZrO_2$ phase separation from YSZ were performed. A discussion comparing phase separation to metal content, pH and yttria content for each metal system is presented below.

The amount of $mZrO_2$ formed during synthesis was studied as a function of metal concentration (Figure 3.1). The figure shows the percent stabilization of YSZ (%w/w YSZ:%w/w $mZrO_2$) with respect to metal content for samples precipitated at pH 13 with 2*M* NaOH and calcined to 950°C.

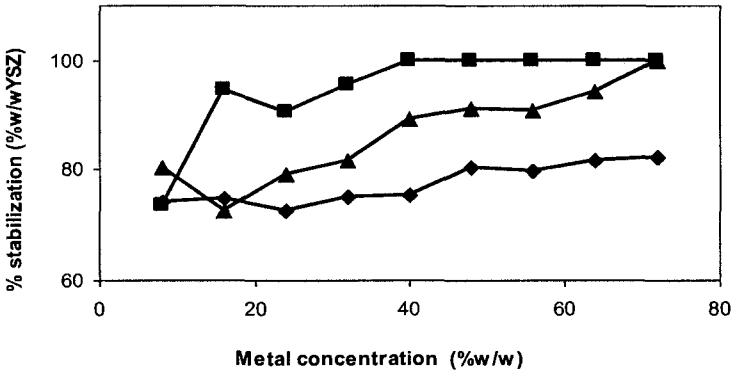

Figure 3.1 Percent stabilization of YSZ to monoclinic zirconia as a function of metal content for (■) NiO-YSZ, (♦) CuO-YSZ and (▲) Co_3O_4-YSZ anode precursors at pH 13.

At low metal concentrations, the percent stabilization was low at approximately 65%. With increasing Ni content stabilization increased and reached 100% at a metal content of 40%w/w. Stabilization of YSZ also increased with increasing amounts of Cu and Co. The CuO-YSZ samples did not reach full stabilization; instead they plateaued at approximately 75%, while the Co_3O_4-YSZ samples reached full stabilization, but only at high metal contents (72%w/w).

Percent stabilization with respect to final pH was also measured for low metal concentration (8wt%) MO-YSZ mixtures. Figure 3.2 shows this dependence for all metal oxide samples.

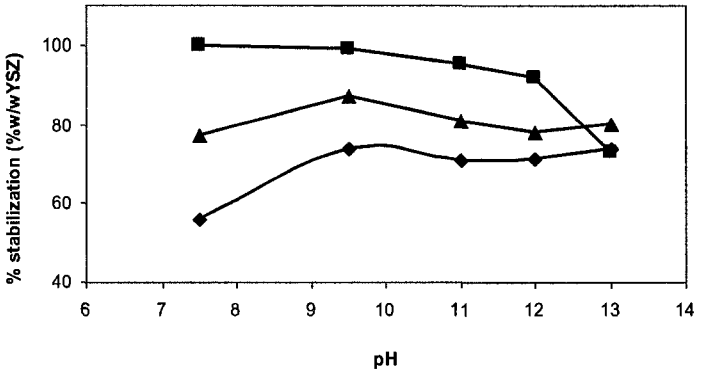

Figure 3.2 Percent stabilization of YSZ to monoclinic zirconia as a function of pH for (■) NiO-YSZ, (♦) CuO-YSZ and (▲) Co_3O_4-YSZ anode precursors with metal content of 8%w/w.

At pH<6 full stabilization of zirconia did not occur due to incomplete precipitation of yttria out of solution. Above pH 7, stabilization for the NiO-YSZ-$mZrO_2$ system was pH dependant. Complete stabilization occurred at pH 7 but rapidly decreased with increasing OH^- concentrations. The CuO-YSZ-$mZrO_2$ system showed the opposite trend, increasing stabilization for increasing pH, while Co_3O_4-YSZ-$mZrO_2$ showed little change in $mZrO_2$ content over the pH range tested.

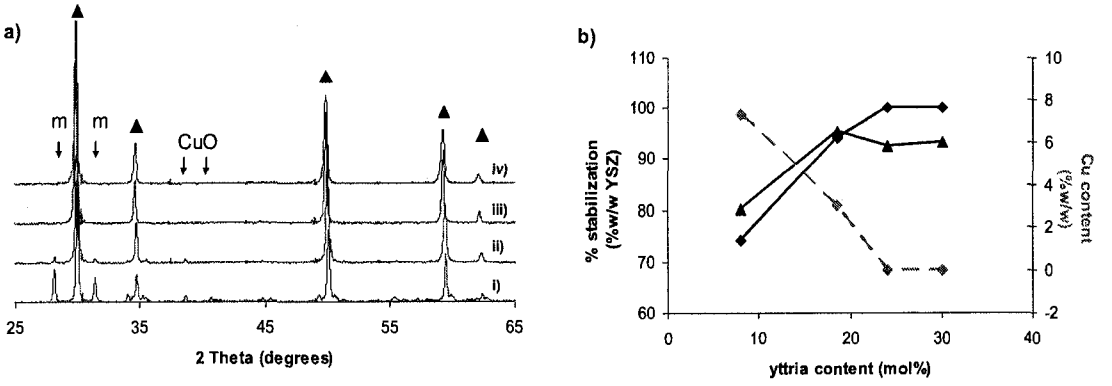

Figure 3.3 a) XRD patterns of 8%w/w Cu sample with differing yttria contents calcined to 950°C; i) 8.5 mol% YSZ; ii) 19 mol% YSZ; iii) 24 mol% YSZ; and iv) 29 mol% YSZ. b) Relationship between YSZ stabilization for (♦) CuO-YSZ and (▲) Co_3O_4-YSZ and yttria content. (◈) Loss of copper with increasing yttria content.

Although full stabilization of YSZ was achieved for a wider range of metal content and pH values for the NiO system, complete YSZ stabilization for CuO-YSZ was only accomplished with increasing amounts of yttria. However, as stabilization of YSZ increased,

Cu was lost during calcinations. Figure 3.3.a shows XRD patters of CuO-YSZ-$mZrO_2$ precipitated at pH 9.5 with increasing amounts of yttrium. The absence of Y_2O_3 peaks indicated the complete solubility of yttria in the zirconia lattice for all concentrations studied. However, at a yttria content of 8.5mol%, the monoclinic zirconia phase was clearly visible. As yttria content increased, YSZ became fully stabilized but CuO content decreased as shown by XRF. Figure 3.3.b shows the relationship between the gain of stabilization and the loss of Cu, which occurs during calcination. Increasing the pH from 9.5 to ~13 was required to negate the loss of Cu since XRD showed that at low pH the precipitate was the volatile copper hydroxychloride ($Cu_2(OH)_3Cl$). As pH increases, the formation of CuO is expected and has been documented for many copper salts, including $Cu(NO_3)_2$ through the formation of $Cu_2(OH)_3NO_3$ and $CuSO_4$ through the formation of $Cu_4(OH)_6SO_4$.[22,24] YSZ never became fully stabilized regardless of yttria content for the Co_3O_4-YSZ-$mZrO_2$ system. Maximum stabilization (95%) was reached at a yttria content of 19mol% without any Co loss during calcination.

Figure 3.4 shows the crystallization pathway of CuO-(8.5 mol%) YSZ (8 wt% metal content). The dried powder showed no peaks, indicating amorphous structures for both copper and yttrium/zirconium phases.

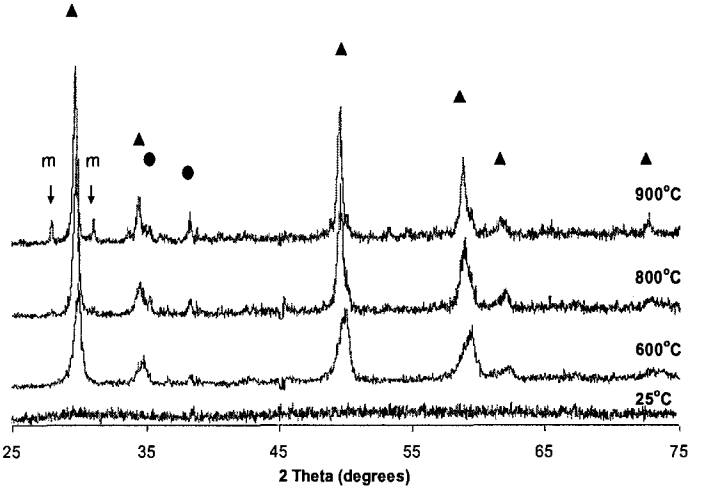

Figure 3.4 Crystallization pathway of CuO-(8.5 mol %) YSZ. ▲:YSZ, ●: CuO.

As temperature increased, formation of YSZ crystals occurred at approximately 400°C, while CuO crystallization occurred at 600°C. At temperatures above 600°C the full width at half maximums of YSZ and CuO peaks continued to narrow, indicating a growth in

crystallite size. At elevated temperatures, the monoclinic crystalline phase of zirconia appeared.

Formation of monoclinic zirconia could occur as a phase transformation of YSZ into $mZrO_2$ or as an independent crystallization. The area of YSZ peaks remained constant during the appearance of the $mZrO_2$ peaks. Therefore, the fraction of YSZ/$mZrO_2$ was not temperature dependant, suggesting the $mZrO_2$ phase did not segregate from stabilized YSZ but was crystallizing independently. The same crystallization pathway is evident for all samples tested on the variable temperature XRD.

The coexistence of monoclinic and cubic forms of zirconia has been extensively studied in the literature. A recent review by *Yashima et al.* shows phase diagrams that suggest co-existence of both phases is expected at 950°C and complete stabilization at 1000°C occurs at approximately 20 mol% $YO_{1.5}$ and not 14.8 mol $YO_{1.5}$.[25] Additionally, it is possible to stabilize zirconia into the cubic phase by introducing CuO or NiO into the lattice. The addition of NiO and CuO to zirconia by sol-gel technique resulted in fully stabilized zirconia at concentrations above 10mol% Ni and Cu.[26,27]

Formation of monoclinic zirconia in the presence of low concentrations of metal suggested it was not the interaction between the metals and zirconia that caused destabilization, but the relative concentrations of metals with respect to hydroxide concentration that played the major role in YSZ phase purity. To obtain phase pure NiO-YSZ, precipitation to pH 9.5 ensures full precipitation of all components with complete phase purity of the YSZ regardless of metal content. CuO- and Co_3O_4-YSZ phase pure substances must have a higher yttria content to obtain stabilized YSZ.

3.3.2 Control of microstructure, sinterability and performance in Ni-, Cu- and Co-YSZ anodes

To achieve a more meaningful discussion, the results have been separated into three sections; formation of metal-oxide-YSZ materials, microstructure and sintering properties and finally an evaluation of performance. Within each section, three metal-YSZ materials are discussed in detail and comparative comments are provided. To ensure YSZ phase purity, the Ni anode powder consisted of 9 mol% YSZ, while copper and cobalt materials were synthesized with 21 mol% YSZ.

3.3.2.1 Formation of anode precursors

Table 3.1 defines the conditions for precipitation and the amount of metal in the final powder product in comparison with predicted metal content based on reactant quantities.

Table 3.1 Compositions of prepared anode precursor powders using various precipitation agents and summary of intermediate species present after drying at 120°C.

Sample	Precipitation agent	pH reached by NH_3 and/or NaOH	Intermediate Species[a]	Theoretical metal content (wt%)	Real metal content (wt%)
NiYSZ-1	NH_3	11	n/a	45	9
NiYSZ-2	NH_3+NaOH	11 + 13	$Ni(OH)_2$ (crys)	45	36
NiYSZ-3	NaOH	13	$Ni(OH)_2$ (amorph)	45	33
CuYSZ-1	NH_3	6	$Cu_2Cl(OH)_3$ (crys)	45	38
CuYSZ-2	NH_3	11	n/a	45	6
CuYSZ-3	NH_3+NaOH	6 + 13	$Cu(OH)_2$ (crys)	45	61
CuYSZ-4	NH_3+NaOH	11 + 13	CuO (crys)	45	50
CuYSZ-5	NaOH	13	CuO (crys)	45	60
CoYSZ-1	NH_3	11	n/a	45	12
CoYSZ-2	NH_3+NaOH	11 + 13	Co+3O(OH) (amorph)	45	45
CoYSZ-3	NaOH	13	Co+3O(OH) (crys)	45	52

[a]n/a – not measured; amorph – amorphous phase present as shown by XRD; crys – crystalline phase present as shown by XRD

The nickel and cobalt samples prepared with ammonia as the precipitation agent (NiYSZ-1 and CoYSZ-1) resulted in low metal yield. However, the copper sample precipitated with ammonia to pH 6 showed complete precipitation of copper out of solution. Increasing the amount of ammonia to pH 11 reintroduced copper back into solution, resulting in low metal yield for this sample. All samples precipitated to pH 13 by addition of NaOH resulted in metal yields similar to expected amounts. Final copper yields were larger than expected when the final pH of solution was 13, indicating re-dissolution of zirconium and yttrium was relatively high compared to the copper precipitate. Unlike copper samples, nickel and cobalt powders never reached a state in which ammonia precipitated all of the metal from solution. NaOH was required to attain predicted compositions of Ni-YSZ and Co-YSZ.

3.3.2.1.1 Nickel –YSZ

The complexation of ammonia to Ni^{2+} occurred in a stepwise fashion throughout the precipitation process. Figure 3.5.a shows the $[Ni(H_2O)_{6-n}(NH_3)_n]^{2+}$ complexes of n = 0, 1, 2, 5 and 6 which were identified at different stages of the precipitation process as a function of pH of solution.

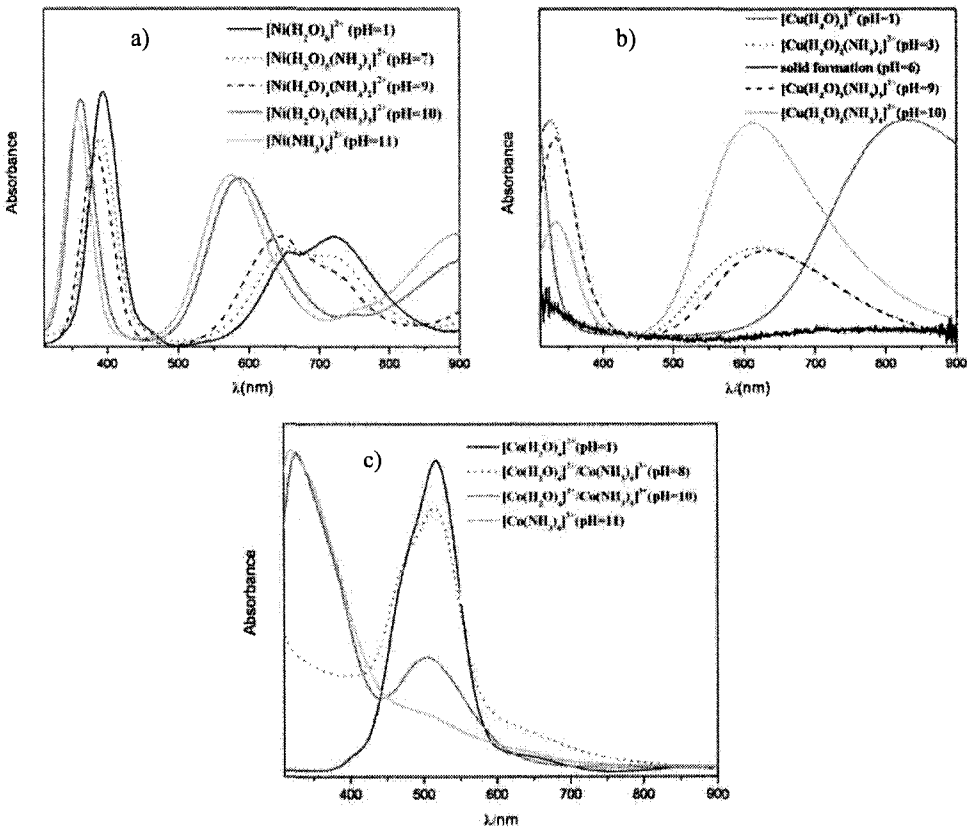

Figure 3.5 Visible spectra of ammine complexes synthesized during ammonia co-precipitation. a) $[Ni(H_2O)_{6-n}(NH_3)_n]^{2+}$ (n=0-6); b) $[Cu(H_2O)_{6-n}(NH_3)_n]^{2+}$ (n=0-4) and c)$[Co(H_2O)_6]^{2+}/[Co(NH_3)_6]^{3+}$

Each absorption maxima can be used to characterize the complexes in solution as there is a shift towards shorter wavelengths as increasing amounts of NH_3 are introduced into solution.[28,29] At the final stages of ammonia precipitation, all six of the coordinated H_2O have been displaced by NH_3, resulting in a $[Ni(NH_3)_6]^{2+}$ complex which exhibited a λ_{max} at 355 and 570 nm. Since $[Ni(NH_3)_6]^{2+}$ is soluble and stable in water, only a fraction of the Ni^{2+} precipitated out as $Ni(OH)_2$. As a result, the real composition of Ni in the Ni-YSZ powder mixture (NiYSZ-1) was significantly lower than the theoretical 45wt% as predicted by reactant concentrations. When ammonia precipitation was followed by addition of 2*M* NaOH to pH 13, the composition of Ni in the final product (NiYSZ-2) increased to a value closer to the predicted composition, indicating that most of the ammonia-nickel complex was transformed to a nickel precipitate. The precipitation performed solely with 2*M* NaOH

(NiYSZ-3) resulted in a product with final nickel content similar to NiYSZ-2. Because of the low nickel yield of NiYSZ-1, only NiYSZ-2 and -3 were studied further.

The solid precipitate formed after addition of base is characterized as $Ni(OH)_2$ by the sharp peak at 3650cm^{-1} observed in the FTIR spectrum (Figure 3.6.a.1).

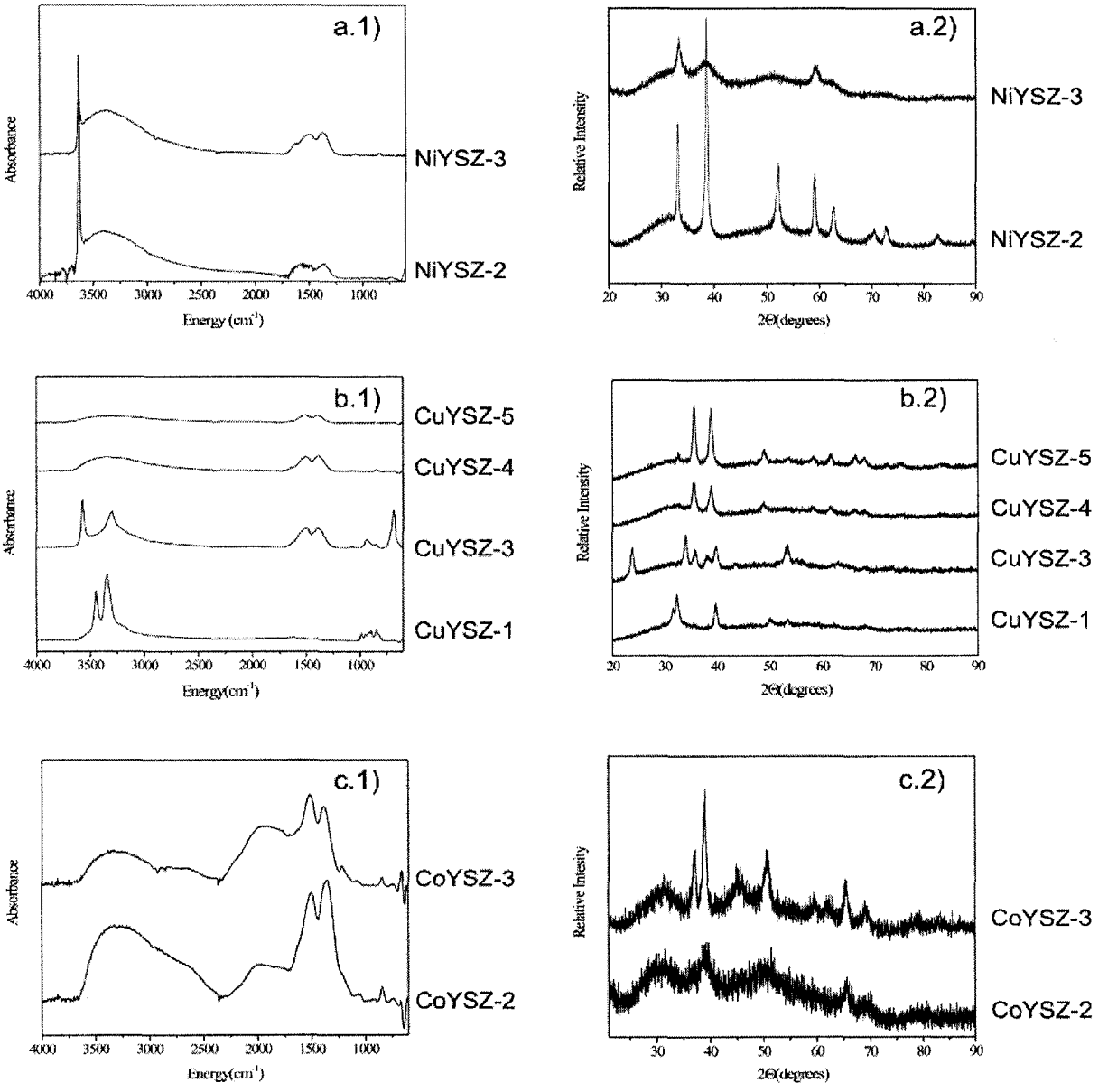

Figure 3.6 ATR-FTIR and XRD patterns of dried powders prepared with NH_3 + NaOH and NaOH. a) nickel samples; b) copper samples; c) cobalt samples

Ni^{2+} precipitated in the hydroxide form for both NiYSZ-2 and NiYSZ-3. The broad peaks at 1365, 1535 and 1630cm^{-1} were present in all samples and were attributed to the bending modes of bound water and zirconium/yttrium precipitates formed during synthesis. XRD patterns of nickel powders synthesized by NH_3 + NaOH and NaOH are shown in Figure 3.6.a.2. The dried power prepared with NH_3 + NaOH (NiYSZ-2) shows seven peaks representing a crystalline $Ni(OH)_2$ phase with no other crystalline phases present. After calcination to 750°C, crystalline NiO (PDF# 47-1049) and YSZ (PDF# 30-1468) phases were present with crystallite sizes of 36±3 and 15±1 nm respectively. Figure 3.6.a.2 shows the $Ni(OH)_2$ phase of NiYSZ-3 lacked a significant crystalline structure within the prepared powder and was better described as amorphous. After calcination, crystalline NiO and YSZ were present with sizes of 28±2 and 24±1 nm respectively.

Although both synthesis techniques resulted in a $Ni(OH)_2$ phase, only the powder synthesized with NH_3 + NaOH led to a significant amount of crystalline $Ni(OH)_2$ prior to calcination, indicating the following mechanism represents the synthesis pathway for NiO in NiYSZ-2:

$$Ni^{2+}_{(aq)} \xrightarrow{NH_{3(g)}(pH11)} [Ni(H_2O)_{6-n}(NH_3)_n]^{2+}_{(aq)} \xrightarrow{OH^-_{(aq)}(pH13)} Ni(OH)_{2(crys)} \xrightarrow[-H_2O_{(g)}]{} NiO_{(crys)} \qquad n = 0\text{-}6 \quad (3.1)$$

In contrast, crystallization of $Ni(OH)_2$ did not occur under the preparation conditions of NiYSZ-3 and FTIR and XRD data suggested the following precipitation and calcination process:

$$Ni^{2+}_{(aq)} \xrightarrow{OH^-_{(aq)}(pH13)} Ni(OH)_{2(amorph)} \xrightarrow[-H_2O_{(g)}]{} NiO_{(crys)} \qquad (3.2)$$

The degree of crystallinity of nickel hydroxide was improved with ammonia synthesis, regardless of pH. This is in contrast to findings of *Song et al*, where the degree of crystallinity was regarded as a function of pH,[30] suggesting crystalline defect formation may be the result of mechanistic variables.

3.3.2.1.2 Copper –YSZ

Figure 3.5.b shows the visible spectra of copper species during precipitation with ammonia at various points in the process. Although complexation of ammonia to Cu^{2+} is similar to that of Ni^{2+} and occurs in a stepwise fashion, not all of the water ligands are substituted by ammonia. The visible spectra of copper(II) ammonia solutions display maxima in the range of 900-500nm, which corresponds to the 'd-d' transitions of the complexes $[Cu(NH_3)_n(H_2O)_{6-n}]^{2+}$, n = 0-4.[31] Furthermore, copper was fully precipitated out of solution using ammonia. FTIR of the dried precipitate indicated the presence of a copperhydroxychloride basic salt for samples precipitated with NH_3 to pH 6 (CuYSZ-1). More specifically the x-ray diffraction pattern of this substance showed the resultant precipitate was monoclinic $Cu_2Cl(OH)_3$ (PDF# 50-1559). Calcination to 750°C resulted in the final precursor powder containing crystalline CuO (PDF# 48-1548) and YSZ phases with crystallite sizes of 39±5 and 30±1 nm respectively. The following mechanism represents the synthesis pathway for CuO in CuYSZ-1:

$$Cu^{2+}_{(aq)} \xrightarrow{NH_{3(g)}(pH0-5)} [Cu\,(H_2O)_{6-n}(NH_3)_n]^{2+}_{(aq)} \xrightarrow{NH_{3(g)}(pH6)} Cu_2Cl(OH)_{3(crys)}$$

$$\xrightarrow[-H_2O_{(g)}+HCl_{(g)}]{} CuO_{(crys)} \qquad n = 0\text{-}4 \quad (3.3)$$

When an excess of ammonia (pH 11) was added, most of the $Cu_2Cl(OH)_3$ precipitate returned to solution as $[Cu(H_2O)_{6-n}(NH_3)_n]^{2+}$, n = 0-4. This complex was stable in solution and resulted in a low final yield of Cu in the final product. For this reason CuYSZ-2 was not studied further.

When the ammonia precipitation was followed by an addition of 2*M* NaOH to pH 13, the composition of Cu in the final product reached a value closer to the predicted composition, demonstrating that most of the ammonia-copper complex was transformed to a solid precipitate. NaOH was added to the copper-ammonia solution at two distinct points during precipitation, at pH 6 (CuYSZ-3) and 11 (CuYSZ-4). Although both samples resulted in full precipitation of copper from solution, FTIR and XRD (Figure 3.6.b.1 and 3.6.b.2) showed the resulting dried powders were not equivalent. CuYSZ-3 precipitate consisted of an orthorhombic $Cu(OH)_2$ crystalline phase (PDF# 13-0420), while CuYSZ-4 had monoclinic CuO. Both powders resulted in crystalline CuO and YSZ phases after

calcination. The following equations represent the mechanisms of copper precipitation for copper samples synthesized with NH_3 + NaOH.

$$Cu^{2+}_{(aq)} \xrightarrow{NH_{3(g)}(pH5)} [Cu(NH_3)_n(H_2O)_{6-n}]^{2+}_{(aq)} \xrightarrow{NH_{3(g)}(pH6)} Cu_2Cl(OH)_{3(crys)}$$
$$\xrightarrow{OH^-_{(aq)}(pH13)} Cu(OH)_{2(crys)} \xrightarrow[-H_2O_{(g)}]{} CuO_{(crys)} \qquad n = 0\text{-}4 \qquad (3.4)$$

or

$$Cu^{2+}_{(aq)} \xrightarrow{NH_{3(g)}(pH11)} [Cu(NH_3)_n(H_2O)_{6-n}]^{2+}_{(aq)} \xrightarrow{OH^-_{(aq)}(pH13)} CuO_{(crys)} \quad n = 0\text{-}4 \qquad (3.5)$$

The precipitation performed solely with 2*M* NaOH (CuYSZ-5) resulted in a product with final copper content similar to CuYSZ-1, 3 and 4. FTIR and XRD analysis demonstrated the dried product was similar to that of CuYSZ-4 and contained crystalline CuO. Calcination to 750°C produced a final product containing CuO and YSZ.

$$Cu^{2+}_{(aq)} \xrightarrow{OH^-_{(aq)}(pH13)} CuO_{(crys)} \qquad (3.6)$$

Unlike Ni-YSZ samples, which resulted in $Ni(OH)_2$ precipitates for both methods, the conditions by which copper precipitated out of solution modified the intermediate species contained in the dried powder. Calcination of these intermediates resulted in the same final product (CuO-YSZ), but with different structural properties. Additionally, the nickel samples required calcination to obtain NiO from the hydroxide precursors, causing the particle size to increase. However, both CuYSZ-4 and -5 did not require calcination to obtain crystalline CuO, though calcination was required to obtain crystalline YSZ. Transformation from intermediate copper species to CuO in solution with excess hydroxide has been previously documented.[22] Interestingly, CuYSZ-3 did not show this transformation to CuO, regardless of pH. The formation of $Cu(OH)_2$ was observed instead.

3.3.2.1.3 Cobalt –YSZ

Complexation of ammonia to Co^{2+} is particularly interesting because oxidation of fully complexed cobalt-ammonia species occurs in air.[32] Although ammonia can substitute complexed water in Co^{2+} species, its addition must be performed in an inert atmosphere to

maintain a 2+ oxidation state.[33] When ammonia complexation occurs in air, as in this case, oxidation to Co^{3+} occurs. Fig 3.5.c demonstrates the successive addition of ammonia to cobalt did not occur. Instead, there was a decrease in the first band $\lambda_{max}([Co(H_2O)_6]^{2+})$/515nm, while the intensity of the second band ($\lambda_{max}([Co(NH_3)_6]^{3+})$/320nm) increased with rising amounts of ammonia. Since $[Co(NH_3)_6]^{3+}$ is very stable in water, only a fraction of the cobalt was precipitated out of solution, leading to a cobalt composition significantly lower than the theoretical 45wt%. Similar to the nickel species, $[Co(NH_3)_6]^{3+}$ was fully extracted out of solution by addition of 2*M* NaOH to pH 13 and resulted in a final composition similar to the predicted value. Likewise, precipitation performed solely with 2*M* NaOH (CoYSZ-3) resulted in a product with acceptable metal composition (Table 3.1). Due to the low yield of CoYSZ-1, only CoYSZ-2 and -3 were studied further.

XRD patterns of powders synthesized by NH_3 + NaOH and NaOH are shown in Fig 3.6.c.2. The dried power prepared with NH_3 + NaOH (CoYSZ-2) showed amorphous structures for both the YSZ and cobalt precipitates. After calcination to 750°C, crystalline Co_3O_4 (PDF# 07-0169) and YSZ phases were present with sizes of 41±4 and 23±1 nm respectively. CoYSZ-3 showed that precipitation with NaOH to pH 13 led to crystalline Co+3O(OH) (PDF# 07-0169). After calcination, crystalline Co_3O_4 and YSZ were present with crystallite sizes of 28±2 and 14±1 nm respectively.

Both synthesis techniques led to a Co_3O_4-YSZ precursor powder with comparable crystallite sizes. As with the nickel samples, NH_3 precipitation resulted in cobalt-ammine complexes which limited metal yield. Synthesis with a strong base was needed to completely precipitate cobalt from solution. The following mechanism represents the synthesis pathway for Co_3O_4 in CoYSZ-2:

$$Co^{2+}_{(aq)} \xrightarrow{NH_{3(g)}(pH11)} [Co(NH_3)_6]^{2+}_{(aq)} \xrightarrow{air} [Co(NH_3)_6]^{3+}_{(aq)} \xrightarrow{OH^-_{(aq)}(pH13)}$$
$$Co{+}3O(OH)_{(amorph)} \xrightarrow[-H_2O_{(g)}]{} Co_3O_{4(crys)} \qquad (3.7)$$

In contrast, crystallization of cobalt oxyhydroxide species occurs under the preparation conditions of CoYSZ-3 where the XRD data suggest the following precipitation and calcination process:

$$Co^{2+}_{(aq)} \xrightarrow{OH^-_{(aq)}(pH13)} Co{+}3O(OH)_{(crys)} \xrightarrow[-H_2O_{(g)}]{} Co_3O_{4(crys)} \quad (3.8)$$

Unlike the NiYSZ samples, in which a crystalline hydroxide phase formed when ammonia was used to induce precipitation, cobalt resulted in an oxyhydroxide crystalline phase when NaOH was used as the precipitation agent. Calcination of the dried powders resulted in the same final product (Co_3O_4-YSZ).

Overall, we have identified different mechanisms of formation for each of the metal oxide – YSZ precursors. Not only did each metal behave differently, but the choice of base changed the mechanism of precipitation. As will be shown in the following section, this had a pronounced effect on the material's microstructure. The effect of base on YSZ crystallites is more restricted.

3.3.2.2 Powder morphology and sintering

3.3.2.2.1 Nickel –YSZ

Specific surface area measured by the BET method and particle sizes of the metal and YSZ before and after sintering are shown in Table 3.2.

Table 3.2 Surface area of reduced anode powder and average particle sizes of metal and YSZ prior to and following sintering to 1200°C.

Sample	BET surface area (m^2/g)	d_{Metal} (nm)	d_{YSZ} (nm)	d_{Metal}/d_{YSZ}	E_a sintering (kJ/mol)
NiYSZ-2					
Calcined	23.3	38	38		
Sintered	6.7	1458	98	15	190±30
NiYSZ-3					
Calcined	22.7	294	30		
Sintered	5.7	2543	119	38	330±20
CuYSZ-1					
Calcined	14.5	14320	42		
Sintered	14.9	14090	27	522	1300±300
CuYSZ-3					
Calcined	8.4	5874	47		
Sintered	20.8	142	22	6	840±20
CuYSZ-4					
Calcined	10.8	861	47		
Sintered	4.8	9062	103	88	150±70
CuYSZ-5					
Calcined	18.2	769	22		
Sintered	19.9	5223	20	261	300±80
CoYSZ-2					
Calcined	15.8	1571	35		
Sintered	10.1	9628	54	178	300±30
CoYSZ-3					
Calcined	19.0	1005	26		
Sintered	6.9	11810	72	164	780±90

Nickel particle sizes of the calcined powders vary significantly for samples prepared with NH_3 + NaOH versus NaOH. However, this difference became less obvious after sintering to 1200°C. The nickel particle size of NiYSZ-2 increased by a factor of 40, while the Ni component of NiYSZ-3 grew to 9 times its original size. Differences in particle size within each powder were also observed by SEM imaging. The nanosized nature of the NiYSZ-2 powder was observed with SEM (Fig 3.7.a) and showed a homogeneous distribution of NiO within the YSZ matrix. The agglomerates were composed of near spherical particles that ranged from approximately 70-90*n*m in diameter. In contrast, an inhomogeneous NiO-YSZ distribution was observed with powders synthesized solely with NaOH (Fig 3.7.b). Two types of morphologies were present in this sample: small oval-shaped particles approximately 70-90 *n*m, and larger crystallites, up to 2μm in length. EDX measurements showed these large crystallites consisted of a single NiO phase, while the "meshy" part of the sample was a NiO-YSZ mixture.

The difference in NiO:YSZ size ratio between the respective phases had a significant effect on the materials' behaviour, particularly on their sinteractivity. Sintering behaviour was significantly different between powders despite them having identical green densities (3.0 ± 0.1 g/cm^3) and is illustrated by observing the shrinkage as a function of temperature (Fig 3.8).

Tietz et al. have shown the temperature of maximum shrinkage for eight commercial mechanically mixed NiO-YSZ samples was approximately 1200°C; a value comparable to the sintering temperature of both nickel samples prepared in this study. Although the sintering temperature was approximately the same for both powders, where the temperature of largest change in length was between 1100°C and 1200°C, the actual change in length was significantly different. These changes were related to the activation energy of shrinkage derived from the combined-stage sintering model described in Section 2.3.7. The insets of Fig 3.3.8 show the rate of shrinkage for each metal within the linear region. Fitting the curves to equation (2.16), a small activation energy for NiYSZ-2 of 190 +/- 30 kJ/mol and a relatively large one for NiYSZ-3 of 330 +/- 10 kJ/mol were calculated. The predominant mechanism was assumed to be grain boundary diffusion (n=0.33) based on the mechanism attributed to the sintering of 8%YSZ.[34] For NiYSZ-3 the activation energy of densification fell just outside those reported previously (380-530 kJ/mol) for mechanically combined NiO-

YSZ. Unlike NiYSZ-3, NiYSZ-2 had an activation energy significantly smaller than those reported.[6]

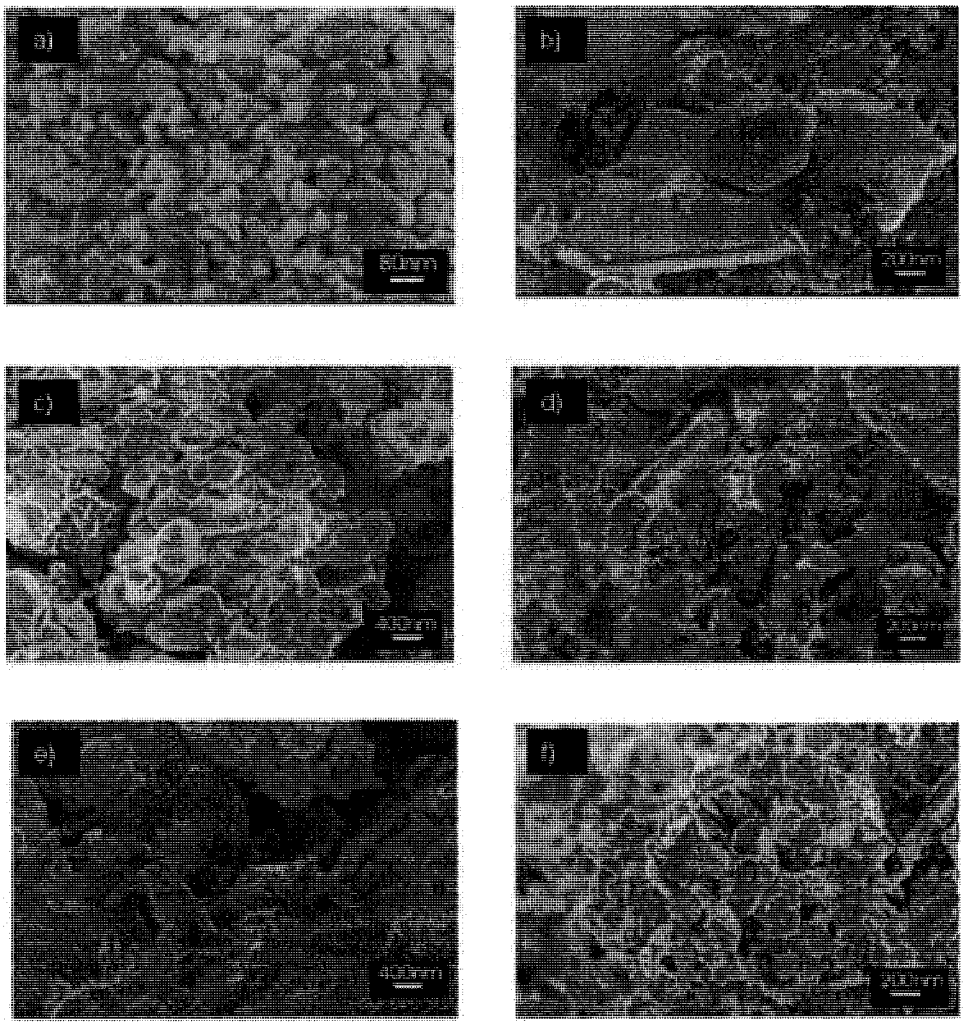

Figure 3.7 SEM images of calcined powders prepared under various synthesis conditions a)NiYSZ-2; b) NiYSZ-3; c) CuYSZ-3; d) CuYSZ-5; e) CoYSZ-2; f)CoYSZ-3.

Although both final precursor powders consisted of appropriate amounts of NiO and YSZ, the NiO distribution and average particle size of NiO was affected by synthesis conditions. The presence of a well ordered $Ni(OH)_2$ crystalline phase in the pre-calcined powder limited NiO mobility within the YSZ matrix, resulting in NiO crystallites that were small, homogeneously dispersed with a narrow size distribution. Calcination of amorphous $Ni(OH)_2$

(in NiYSZ-3) allowed NiO aggregation into large particles resulting in a solid solution with wider particle size distribution and inhomogeneities between the two phases.

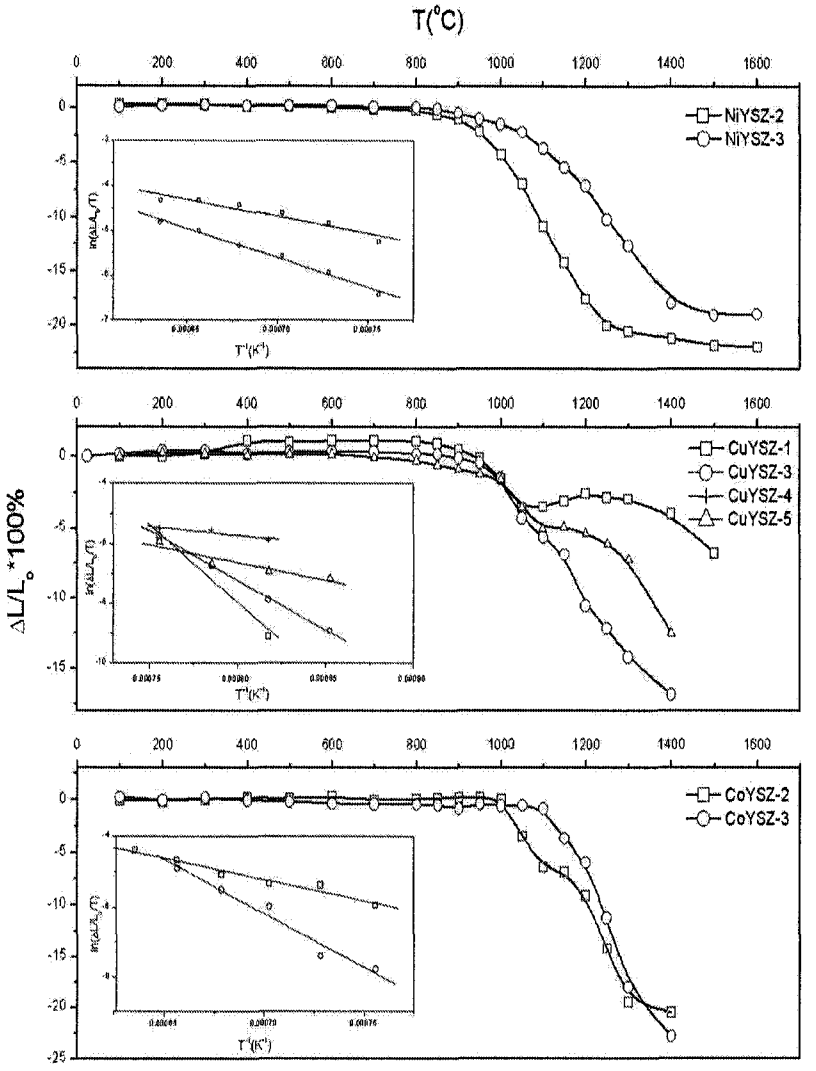

Figure 3.8 Shrinkage characteristics of each sample as a function of temperature. Inset: Determination of the activation energy of sintering for each sample using the Arrhenius relationship.

The difference in NiO phases between powders directly affected the activation energies of sintering of the NiO-YSZ mixtures. Since there was no significant difference between YSZ calcination, particle size, morphology or green densities, the difference in sinteractivity is a direct result of the sinterability of the NiO phase. The presence of sinterable NiO,

consisting of small nanosized particles, reduced the activation energy of sintering which in turn altered the compatibility of such anodes with other components of the fuel cell.

3.3.2.2.2 Copper –YSZ

Figure 3.3.8 shows that unlike nickel, copper samples began the densification process at approximately 900°C. Past temperatures of 1100°C, the densification rate decreased. The first densification process was assigned to sintering of copper particles, while the second was assigned to YSZ sintering and subsequent melting of copper oxide within the sample. This explains the expansion seen at temperatures greater than 1100°C. CuYSZ-1 showed the most distinct difference between the two sintering phases, where expansion of the sample is observed at 1050°C and continued until 1200°C.

Adsorption analysis of the CuYSZ-1 showed the particle size of copper with respect to YSZ was extremely large. Heating this sample to 1050°C did not affect either copper or YSZ particle sizes. Although it was not expected for YSZ to sinter at this temperature, sintering of copper particles at this temperature was expected. The lack of grain growth in this sample was indicative of its large sinteractivity of 1300 ± 300kJ/mol.

CuYSZ-3 also exhibited unusual sintering behavior. Unlike other samples, this one showed a decrease in metal particle size, while there was an overall increase in surface area. Further analysis with SEM and EDX indicated this sample underwent a phase separation during sintering, where copper segregated from YSZ. Fig 3.9 shows CuYSZ-3 powder sintered onto YSZ electrolyte.

EDX spot analysis showed the copper phase formed a perimeter around the rest of the anode. Although, the inner region of the anode did contain copper, a significant amount of metal segregated towards the edge of the anode. SEM imaging of the calcined powder (Fig 3.7.c) illustrated the presence of two types of morphologies: Large particles ranging in size from a few hundred nanometers to a few micrometers, and small particles which exhibited diameters in the nanometer range. The large particles were found in large clusters and were present throughout the sample.

CuYSZ-4 and CuYSZ-5 had similar sintering behavior in which copper grain growth did occur. However, unlike the nickel samples, ammonia addition during synthesis did not have a significant effect on copper particle size or its grain growth during sintering. Activation energies of sintering for both samples were low and could not be distinguished. Error analysis led to a high regression error, since the temperature range for CuO-YSZ sintering

occurred in two distinct temperature ranges. As a result, only the range including the YSZ sintering was used to calculate sinteractivity (1100°C – 1300°C).

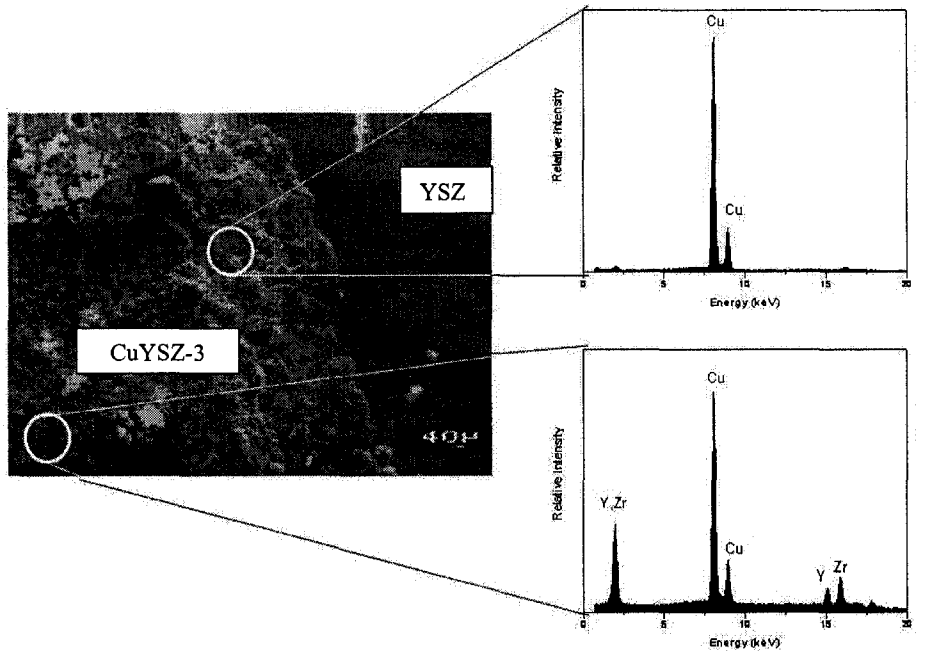

Figure 3.9 SEM image of the top view of CuYSZ-3 on a YSZ substrate after sintering to 1050°C. EDX spot analysis shows a segregation of copper oxide from the YSZ favoring the anode perimeter. The YSZ support is shown for reference.

SEM analysis of CuYSZ-5 (Fig 3.7.d) calcined powder showed a distinct difference in particle morphology to that of CuYSZ-3. Despite the presence of two morphologies, CuYSZ samples synthesized solely with NaOH (CuYSZ-5) resulted in copper platelets randomly distributed throughout the sample with diameters up to approximately one micron and thicknesses around 100*n*m. The presence of these thin particles which were not present in large clusters but randomly distributed throughout the sample led to small sinteractivities. Fortunately, the presence of these particles did not result in copper segregation from the YSZ.

Despite the presence of a CuO and YSZ phase in all the final products, CuO particle size distribution and the resulting sinteractivity were still affected by the precipitation agent employed during synthesis. The presence of a $Cu_2Cl(OH)_3$ precursor resulted in copper particles which had an average particle size of approximately 14μm. The presence of these large particles resulted in a large sinteractivity and therefore the inability for the copper

anode to be appropriately attached to the anode for SOFC testing. Materials calcined from a $Cu(OH)_2$ intermediate resulted in an anode material with a CuO species that segregated from YSZ during fuel cell fabrication. Anodes which resulted in CuO species during precipitation produced powders with similar particle sizes and therefore indistinguishable sinteractivities.

Calcination of copper hydroxychloride and copper hydroxide allowed CuO aggregation into large particles and cluster formations as is the case for CuYSZ-3. The presence of sinterable CuO, obtained by NaOH precipitation to pH 13, reduced the sinteractivity to a point where fuel cell fabrication was possible without phase segregation of the metal from the support.

3.3.2.2.2 Cobalt –YSZ

BET and particle size analysis of the cobalt samples (Table 3.2) demonstrate that the average cobalt particle sizes of the calcined powders were slightly different for samples prepared with NH_3 + NaOH or NaOH. Differences in particle size within each of the powders were also observed by SEM imaging. SEM analysis of CoYSZ-2 shows two distinct types of particles in the solid solution. The major phase consisted of the small nanosized particles seen previously in the copper and nickel samples, while the second phase consisted of large platelets approximately 1μm in diameter and 200nm thick randomly distributed in small numbers throughout the sample. CoYSZ-3 also showed the presence of platelets and small nanoparticles. The formation of cobalt oxide platelets has been observed previously and is attributed to the chloride precursor.[23] However, unlike CoYSZ-2, these platelets were nanosized, and were found in large numbers in cluster-like formations throughout the samples. The presence of these semi-sintered cluster formations may have led to apparent large particle sizes during chemisorption analysis.

The sintering behaviour for each powder was significantly different despite having identical green densities (2.8 ± 0.2 g/cm^3). This can be seen by the shrinkage as a function of temperature for each of the powders (Fig 3.8). Although the sintering temperature was approximately equal for each powder, where the temperature of largest change in length was at 1250°C, the overall change in length was significantly different. Fitting the curves to equation (2.16), a relatively small activation energy for CoYSZ-2 of 300 +/- 30 kJ/mol and a relatively large one for CoYSZ-3 of 780 +/- 90 kJ/mol were calculated. The activation energy of densification of CoYSZ-3 fell outside the activation energies reported for either of the nickel samples, while CoYSZ-2 sinteractivity was similar to that of the NiYSZ-3 and CuYSZ-5. The sinteractivity for CoYSZ-2 can be related to the presence of large

microparticles present throughout the sample, while the relatively large sinteractivity of CoYSZ-3 may be explained by the large semi-sintered cluster formations found within the sample.

Overall, we have shown the relationship of smaller particles showing a smaller energy of activation for sintering. However, the specific shape of the particles (e.g. platelets) also seems to affect sintering, and in particular, the powder microstructure related to the shape of the particles (such as aggregation of platelets) was shown to have a significant effect on E_a and can even cause segregation.

3.3.2.3 Anode Performance

Sintering of each anode was performed on commercially available 8% YSZ (Marketech Intl). Fig 3.10 shows low resolution cross-sectional views of the anode/electrolyte interfaces which reveals highly porous structures on dense YSZ for all prepared samples except CuYSZ-3.

In this case, the interface between YSZ and CuYSZ was indistinguishable. Additionally, the CuYSZ-3 anode was dense with very little porous structure. The lack of porosity at the anode interface was associated with phase segregation particular to this sample.

Electrochemical impedance measurements were used to identify the various resistive components within each anode. The EIS shown resulted from an identical arrangement of the electrode setup, with the only variation being the anode material and are iR_s corrected. The EIS data in Fig 3.11 show three semicircles which are common to each of the spectra, except those for Cu-YSZ anodes. Since the high frequency arc has been demonstrated to depend on the microstructure, it is the resistance of interest.

Qualitatively, it is observed the spectra consist of three flattened semi-circles which is a result of the porous nature of the anode. At low frequencies, there is also the introduction of noise within which has not been clearly defined. The noise was present in all six of the cells and may be the result of electrical noise introduced through the furnace. Impedance work in subsequent chapters does not show this distortion since the fuel cell set-up was modified whereby the fuel cell anode area was doubled and the electrolyte was thicker. To accommodate the larger fuel cell, the furnace was changed and the Chromel® shield was extended to run down the full length of the furnace.

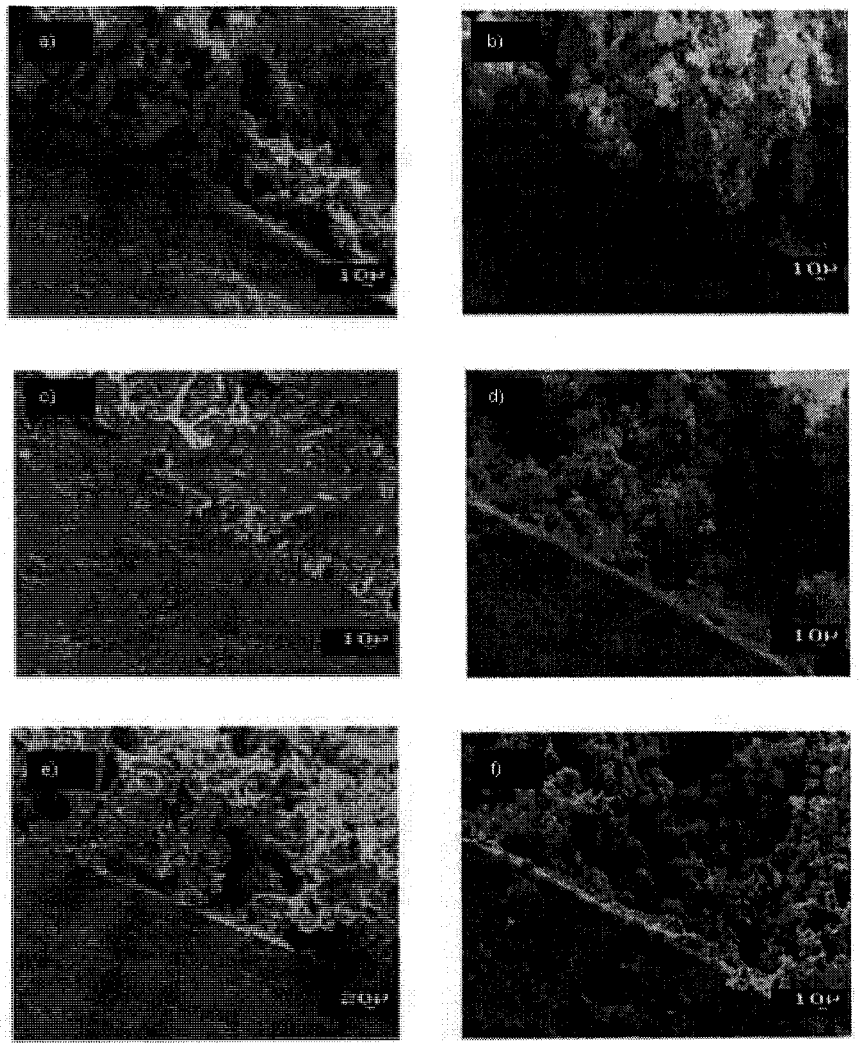

Figure 3.10 Cross-section of YSZ and anode powders after sintering on dense YSZ. a) NiYSZ-2; b) NiYSZ-3; c) CuYSZ-3; d) CuYSZ-5; e) CoYSZ-2; f) CoYSZ-3.

Table 3.3 summarizes the R_1 and R_2 values obtained for each anode. R_1 for anodes operated under fuel cell conditions were determined. The R_1 values for cobalt anodes were lower than for the remaining materials. However, it should be noted that this may be the direct cause of firing conditions, where the cobalt anodes were fired at 1250°C, nickel at 1200°C and copper at 1050°C. Copper samples exhibited very large R_1 values due to the undesirable sintering characteristics associated with copper, particularly CuYSZ-3. Within each metal system, R_1 values were directly correlated to the anode morphology and therefore the d_{metal}/d_{YSZ} ratios. As previously described in this chapters introduction, the

microstructural contribution of Ni-YSZ anodes has been shown to depend on the comparative sizes of YSZ to Ni grains. This observation was confirmed for both Ni-YSZ and Co-YSZ anodes in this study, where the smaller R_1 values were observed with materials that possessed smaller d_{metal}/d_{YSZ} ratios (Table 3.2). Resistances associated with the charge transfer process (R_2) were also affected by d_{metal}/d_{YSZ} and showed the same trend as R_1.

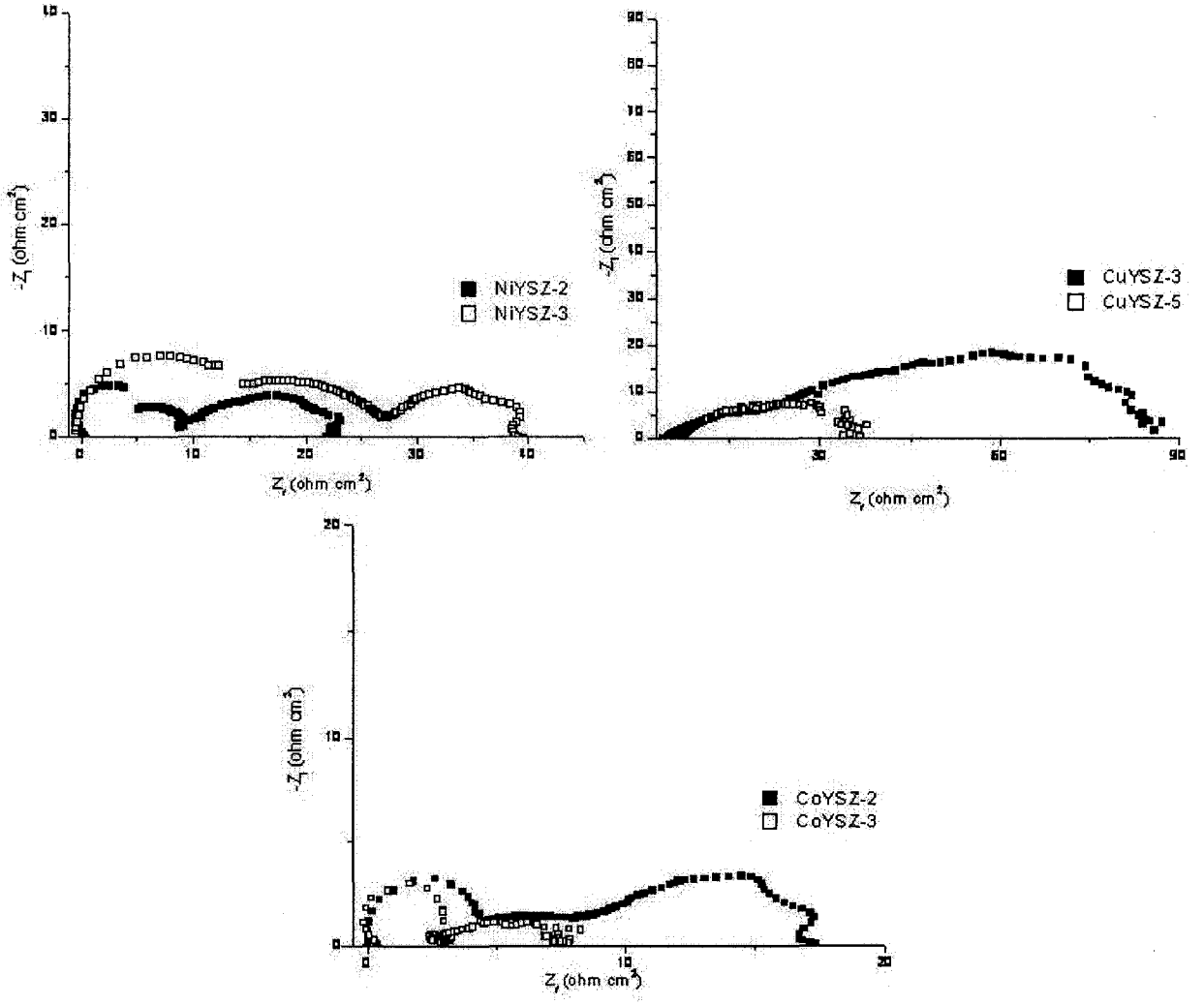

Figure 3.11 Nyquist data for oxidation of H_2 at 800°C at OCV for Ni-YSZ, Cu-YSZ and Co-YSZ anode cermets.

Table 3.3 Comparison of electrochemical performance of various anodes

Sample	R_1 (ohm•cm^2)	R_2 (ohm•cm^2)
NiYSZ-2	4	4
NiYSZ-3	6	18
CuYSZ-3	12	22
CuYSZ-5	4	11
CoYSZ-2	3	6
CoYSZ-3	2	1

R_1 values, were indicative of d_{metal}/d_{YSZ} particle size ratios for NiYSZ and CoYSZ samples, whereby smaller particle size ratios resulted in smaller resistances. Interestingly, the smaller d_{Ni}/d_{YSZ} ratio was obtained by synthesizing with NH_3 + NaOH, while the d_{Co}/d_{YSZ} ratio was smaller when NaOH was the synthesis agent. The differences in particle size ratios may be traced back to the original as synthesized products associated with these samples. That is, a crystalline precursor phase such as $Ni(OH)_{2(crys)}$ and $Co+3O(OH)_{(crys)}$ is the desired precursor product during co-precipitation, since it results in small metal particles at the nanometer scale as observed by SEM imaging of the calcined samples (Fig 3.7). Although CuYSZ anode microstructure could be manipulated in various ways using the precipitation technique, the CuYSZ sample synthesized with NaOH was the only viable copper anode due to its reasonable sintering characteristics and resistance to copper segregation.

3.3 Conclusion

Three co-precipitation methods for preparing various metal based SOFC anodes have been compared. When NaOH and NH_3 + NaOH were used as the precipitation agents, the final composition of the precursor powder was similar to the theoretical yield. Synthesis with NH_3 produced a low metal yield because of the ammonia complexation to metals. Total precipitation of copper with ammonia was possible, but only within a very narrow pH range. Crystalline phases of various metal species were obtained after precipitation leading to distinct morphologies within the calcined powders.

Sintering characteristics have been related to initial metal particle size. Powders with small, homogeneously dispersed metal particles resulted in a more intense densification process. The copper anode synthesized with NH_3 + NaOH, revealed phase separation during anode sintering, which did not occur with any other anode. Fuel cell fabrication and performance was related to d_{metal}/d_{YSZ} particle size ratios and other material properties of the reduced anode. Resistances associated with high frequency impedance processes were smallest for samples which resulted in a crystalline precursor phase during synthesis.

These results suggest that initial synthesis conditions can be used to directly influence the characteristics of the anode precursor powder and make fabrication of a cell a more controlled process. Anode parameters such as sintering and exchange current densities were not only affected by processing of the final powder, but also by the initial synthesis conditions.

References

(1) Zhu, W.; Deevi, S. *Mater. Sci. Eng.* **2003**, *A362*, 228.

(2) Dees, D. W.; Clark, T. D.; Easler, T. E.; Fee, D. C.; Mrazek, F. C. *J. Electrochem. Soc.* **1987**, *134*, 21412146.

(3) Matsushima, T.; Ohrui, H.; Hirai, T. *Solid State Ionics* **1998**, *111*, 315.

(4) Lee, J.; Moon, H.; Lee, H.; Kim, J. K. J.; Yoon, K. *Solid State Ionics* **2002**, *148*, 15.

(5) Wilkenhoener, R.; Vaben, R.; Buchkremer, H.; Stover, D. *J. Mater. Sci.* **1999**, *34*, 257.

(6) Tietz, F.; Dias, F. J.; Simwonis, D.; Stover, D. *J. Eur. Ceram. Soc.* **2000**, *20*, 1023.

(7) Bruggeman, D. *Ann. Phys.* **1935**, *24*, 636.

(8) Lee, J.-H.; Heo, J.; Lee, D.; Kim, J.; Kim, G.; Lee, H.; Song, H.; Moon, J. *Solid State Ionics* **2003**, *158*, 225.

(9) Brown, M.; Primdahl, S.; Mogensen, M. *J. Electrochem. Soc.* **2000**, *2*, 475.

(10) Mizusaki, J.; Tagawa, H.; Saito, T.; Ehara, S.; Takagi, T.; Hikita, T.; Ippommatsu, M.; Nakagawa, S.; Hashimoto, K. *J. Electrochem. Soc.* **1994**, *141*, 2129.

(11) Tanner, C. W.; Fung, K.-Z.; Virkar, A. V. *J. Electrochem. Soc.* **1997**, *144*, 21.

(12) Boer, B. d. SOFC Anode: Hydrogen oxidation at porous nickel and nickel/yttria stabilised zirconia cermet electrodes. PhD Thesis, University of Twente, 1998.

(13) Fukui, T.; Murata, K.; Ohara, S.; Abe, h.; Naito, M.; Nogi, K. *J. Power Sources* **2004**, *125*, 17.

(14) Leng, Y. J.; Chan, S. H.; Khor, K. A.; Jiang, S. P.; Cheang, P. *J. Power Sources* **2003**, *117*, 26.

(15) Muller, A.; Krugel, A.; Ivers-Tiffee, E. *Mat-wiss. u. Werkstofftech* **2002**, *33*, 343.

(16) Park, S.; Gorte, R. J.; Vohs, J. M. *App. Catal. A. Gen.* **2000**, *200*, 55.

(17) Jiang, S.; Callus, P.; Badwal, S. *Solid State Ionics* **2000**, *132*, 1.

(18) Li, Y.; Xie, Y.; Gong, J.; Chen, Y.; Zhang, Z. *Mater. Sci. Eng.* **2001**, *B86*, 119.

(19) Grgicak, C. M.; Green, R. G.; Du, W.-F.; Giorgi, J. B. *J. Am. Ceram. Soc.* **2005**, *88*, 3081.

(20) Gorte, R. J.; Park, S.; Vohs, J. M.; Wang, C. *Adv. Mater.* **2000**, *12*, 1465.

(21) Ahm, K.; Lee, S.; Vohs, J.; Gorte, R. "Novel Bimetallic anodes for direct utilization of hydrocarbon fuels"; Proceedings of the Ninth International Symposium on Solid Oxide Fuel Cells, 2005, Quebec City, Quebec.

(22) McFadyen, P.; Matijevic, E. *J. Inorg. Nucl. Chem.* **1973**, *35*, 1883.

(23) Ishikawa, T.; Matijevic, E. *Colloid Polym Sci* **1991**, *269*, 179.

(24) Lee, S.-H.; Her, Y.-S.; Matijevic, E. *J. Coll. Interface Sci.* **1997**, *186*, 193.

(25) Yashima, M.; Kakihana, M.; Yoshimura, M. **1996**, *86-88*, 1131.

(26) Dongare, M.; Malshe, K. M.; Gopinath, C. S. *Electrochem. Soc. Proceedings* **2002**, *2002-5*, 79.
(27) Dongare, M. K.; Dongare, A. M.; Tare, V.; Kemnitz, E. *Solid State Ionics* **2002**, *153-153*, 455.
(28) Yatsimirskii, K.; Volchenskova, I. *Teoreticheskaya i Eksperimenta'naya Khimya* **1967**, *3*, 17.
(29) Hayakawa, K.; Ueki, H.; Yamasaki, N.; Nakamura, S. *Kagoshima Daigaku Rigakubu Kiyo* **1969**, *2*, 59.
(30) Song, Q.; Tang, Z.; Guo, H.; Chan, S. *J. Power Sources* **2002**, *112*, 428.
(31) Trevani, L. N.; Roberts, J. C.; Tremaine, P. R. *J. Solution Chem* **2001**, *30*, 585.
(32) Bjerrum, J. *Metal ammine formation in aqueous solution*; P. Haase and Son: Copenhagen, 1957.
(33) Yatsimirski, K.; Volchenskova, I. *Teoreticheskaya i Ekserimenta'naya Khimya* **1968**, *4*, 808.
(34) Gibson, I.; Dransfield, G.; Irvine, J. *J. Mater. Sci.* **1998**, *33*, 4297.

4. Electrochemical Characterization of Ni- and Co-YSZ anodes in H_2 Fuel

Abstract

The temperature and potential dependence of electrochemical reaction rates for Ni- and Co-YSZ anodes were examined using alternating (AC) and direct (DC) current techniques. Up to three processes are observed in the impedance data for each metal where the process found in the high frequency range (~10kHz) did not depend on potential suggesting it resulted from a non-faradaic process. The second arc, in the 100Hz range, changed significantly with temperature and overpotential. The increase in reaction rate with respect to temperature and overpotential is symptomatic of a faradaic response and was therefore associated with the charge-transfer reaction. Further DC experiments at various temperatures were performed to determine the inverse Tafel slope (Lefat slope) and the resulting symmetry factor for two anodes (Ni- and Co-YSZ). It was found that the Lefat slope (b^{-1}) decreased with T according to $b^{-1} = \frac{\alpha F}{RT} + K$. The charge transfer coefficient was determined to be 1.5 for both anode systems with only the temperature independent constant K changing between them. The experimental result involving K is examined in relation to the affects of potential on entropy of activation and the apparent energy of activation.

4.1 Introduction

A detailed understanding of the rate-determining steps of SOFC cermet anodes is necessary to appropriately describe fundamental factors related to their kinetics, hence allowing for optimization of the fuel cell. Fundamental factors which describe charge-transfer reactions are generally accepted to occur at the triple phase boundary (TPB). The active TPB is where the metal, electrolyte and open pores meet as paths for the electrons, oxide ions and gas to carry out the hydrogen oxidation reaction of the SOFC anode

$$H_{2(g)} + O^{2-}{}_{(electrolyte)} \leftrightarrow H_2O_{(g)} + 2e^-{}_{(electrode)} \quad (4.1)$$

Although a variety of electrochemical techniques are available to study electrode processes, two main techniques have been used to describe SOFC anodes. One of the most promising methods used to unfold individual rate-limiting steps in SOFC anodes is impedance spectroscopy. This method results in a number of arcs in Nyquist plots which describe at least the same number of processes. In an ideal situation, the arcs are separated enough so they may be de-convoluted and assessed individually. A number of impedance spectra on various anodes have been described in the literature, but offer very little

consistency between interpretations.[1-10] Even the number of arcs reported has been inconsistent between findings.

The electrochemical oxidation of hydrogen on Ni-YSZ anodes is a multistep process which includes the dissociative adsorption of H_2 on the surface, surface diffusion of H or H^+ to the TPB, charge transfer reactions and finally desorption of H_2O molecules. It is yet unclear which of these reactions take place at the TPB and which are rate limiting.

Several reaction schemes for hydrogen oxidation on electrodes have been described. *Mogensen et al.* proposed a mechanism based on impedance data. Each arc was tentatively described for Ni-YSZ cermet anodes[1] and were corroborated by others.[4,8] It was determined that the high frequency arc was highly dependent on cermet structure and least dependant on anode polarization and partial pressures of reactant species, leading to the conclusion that R_1 may be attributed to the transport of charged species (H^+, O^{2-}, OH^-) across the Ni/YSZ interface. Process II, in the mid-frequency range, was most sensitive to atmospheric conditions and potential, suggesting an electron transfer process. Process III, found at low frequencies, was dominated by diffusion. Later it was suggested the third arc represented gas conversion impedance which was detected only in a setup where the electrode was characterized by a stable reference potential. This is the case when the reference electrode is placed in a different atmosphere and hence had no bearing on the anode performance itself, but is a function of the test geometry.[6] Based on the aforementioned impedance interpretations and the responses of each arc to the partial pressure, overpotential and temperature, the following mechanism was proposed and reaction (4.4) was assumed to be rate-limiting.

$$H_2 \rightleftarrows 2H_{ad,M} \quad (4.2)$$

$$2\times\left(H_{ad,M} \rightleftarrows H^+_{ad,M} + e^-\right) \quad (4.3)$$

$$2\times\left(H^+_{ad,M} + O^{2-}_{YSZ} \rightleftarrows OH^-_{YSZ}\right) \quad (4.4)$$

$$2OH^-_{YSZ} \rightleftarrows H_2O + O^{2-}_{YSZ} \quad (4.5)$$

Another possible reaction mechanism is represented by the following equations.

$$H_2 \underset{\leftarrow}{\overset{\rightarrow}{}} 2H_{ad,M} \quad (4.6)$$

$$H_{ad,M} + O_{YSZ}^{2-} \underset{\leftarrow}{\overset{\rightarrow}{}} OH^- + e^- \quad (4.7)$$

$$H_{ad,M} + OH^- \underset{\leftarrow}{\overset{\rightarrow}{}} H_2O + e^- \quad (4.8)$$

Where the first step is assumed to be the dissociative adsorption of H_2 followed by surface diffusion of H_{ad} to the TPB. The oxidation of H_{ad} by oxygen ions from the electrolyte would constitute the first of the electron transfers. If it is assumed that each electron transfer occurs individually, then water formation would proceed via hydroxide intermediates. Based on direct current techniques, *Holtappels et al.* suggested the second electron transfer involving adsorbed hydrogen, H_{ad} was rate determining ($\alpha_a = 0.7$). However, these findings were conclusive only for the temperature range below 845°C.[11] The anodic charge transfer coefficient (α_a) did not vary at low temperatures, but decreased at higher temperatures which led the authors to conclude that a mechanistic change occurs at high temperatures and another reaction step becomes important for the overall reaction rate. *Keech et al.* also suggested this as the possible mechanism when evaluating the performance of sol-derived Ni-YSZ anodes ($\alpha_a = 0.7 - 1.0$).[12] Other reaction pathways including diffusion of H through the bulk of the metal[13] or hydroxide spillover from the YSZ electrolyte to metal[14] have also been proposed.

However, it has previously been argued that changes in charge transfer coefficients with respect to temperature or overpotential may not indicate complex changes in rate-determining steps, but rather a dependence of α on temperature. Determination of the charge transfer coefficient is obtained by using the generalized kinetic equation for a one-electron transfer process proposed by Erdey-Gruz and Volmer and Butler.[15-18]

This relation takes into account both the forward and backward reaction directions of the process and exponential potential dependence of the current components through the transfer coefficients α_a and α_c. It is only in the case of one electron transfers, where the first step is the rate determining one, that $\alpha \equiv \beta$, the symmetry factor. Therefore a link between multi-step electrochemical reaction mechanisms and Tafel slopes must be considered.

At appreciable polarizations, the Butler-Volmer equation is simplified to

$$\ln i = \ln i_o + b^{-1}\eta \text{ where } b^{-1} = \frac{\alpha F}{RT} \quad (4.9)$$

By plotting ln*i* vs η, one may obtain both the exchange current density for a particular reaction and the inverse Tafel slope (Lefat slope). The charge transfer coefficient may be determined if the temperature is known. If equilibrium measurements were obtained at various temperatures, one would expect a plot of b^{-1} versus T^{-1} to result in a slope of $\alpha F / R$ and y-intercept of 0. However, the expected linear proportionality of b^{-1} to T^{-1}, where α is a temperature independent constant has been shown to be the exception rather than the rule. Previous work has indicated that b^{-1} is not dependent on temperature according to Equation 4.9, but varies with temperature in a different manner, because α itself may be a function of temperature. Various cases of α dependence on T are discussed below. The charge transfer coefficient has been shown to vary with temperature in three distinct ways.

The classical expression for b^{-1} with classical T^{-1}-dependence, that is when α is independent of T, has been observed for simple ionic redox reactions that have minimal interaction with the electrode surface.[19] Investigations of the hydrogen evolution reaction with various metals under different conditions have indicated that traditional dependence of b^{-1} with respect to temperature is not followed and that it is actually fitted by the following equation[19-22]

$$b^{-1} = \frac{\alpha' F}{RT} + K \quad (4.10)$$

Which also implies α is *apparently* temperature dependent since

$$b^{-1} = \frac{\alpha F}{RT} \equiv \frac{\alpha' F}{RT} + K \quad (4.11)$$

or

$$\alpha = \alpha' + \frac{KRT}{F} \quad (4.12)$$

A third possible type of b^{-1}-dependence on T^{-1} has been observed and was expressed in anodic Br_2 evolution from Br^- by Conway *et al.*[20] In this case, b^{-1} was found to be independent of T over an 80K temperature range. This phenomenon was also observed for the N_2 and O_2 evolution reactions and O_2 reduction.[19] In this case,

$$b^{-1} = \frac{\alpha(T)F}{RT} \quad (4.13)$$

α varied with T, making b^{-1} seemingly independent of T^{-1}.

The possible b^{-1} dependence on T^{-1} would also influence the conventional representations of the activation processes usually described by an Arrhenius type of equation and also must be considered. Traditionally, the apparent energy of activation is dependent on overpotential and is described by the following equation.

$$i_n = k_0 \exp\left[-\left(\frac{\Delta G^{o\neq} - n\alpha\eta F}{RT}\right)\right] \quad (4.14)$$

where k_o is the rate constant, i_n is the current density at a particular overpotential, n is the number of electrons and $\Delta G^{o\neq}$ represents the apparent activation energy. However, it is obvious the relationship between $\ln i_n$ and T^{-1} will not be linear unless α is independent of T. If α is dependent on T then $\Delta G^{o\neq}$ can only be calculated at OCV, when η is 0.

It is the purpose of this work to investigate the temperature and overpotential dependence of various SOFC anode processes to establish appropriate interpretations of impedance data obtained for porous Ni-YSZ and Co-YSZ SOFC anodes. Additionally, an investigation of the temperature dependence of b^{-1} using DC techniques will determine whether the Lefat slope is classically dependant on T^{-1} for the hydrogen oxidation reaction on Ni-YSZ and Co-YSZ SOFC cermet anodes over a 250°C temperature range, thereby establishing appropriate values of the fundamental parameters α and β.

4.2 Experimental

The fuel cell was prepared by mixing Triton X-100 (Research Chemical Ltd)/water and 1g of anode powder. The YSZ supported metal (M-YSZ) (55wt%) anode materials were prepared via co-precipitation by dissolving appropriate amounts of $ZrCl_4$, Y_2O_3 (dissolved in 10ml of 37wt% HCl) and $NiCl_2 \cdot 6H_2O$ or $CoCl_2 \cdot 6H_2O$ (Aldrich) in 165 ml of distilled water. To ensure YSZ phase purity and stability (Chapter 3), the anode materials were synthesized with 21 mol% YSZ. Precipitation was achieved through introduction of 2M NaOH (Aldrich) to a final pH of 13. Following precipitation, the product was filtered, washed, dried at 120°C and calcined at 750°C for 2h.

0.15g of the anode slurry was coated onto an YSZ green-disk (Tosoh) and heated to 1400°C for 4h in air. A 70wt% LSM/30wt%YSZ mixture (LSM, Nextech Materials; YSZ, Tosoh) was used as the cathode and reference electrode material. The cathode was prepared by coating 0.15g of the LSM/YSZ powder symmetrically opposing the sintered anode, while the reference electrode was approximately 4mm to the side of the cathode. After sintering, the YSZ electrolyte was 0.5mm thick and the area of the electrodes were $0.4cm^2$ for the anode and cathode and $0.2cm^2$ for the reference electrode.

All electrochemical measurements were performed in pure hydrogen (50 sccm flow) at 800°C to 1000°C using intervals of 50°C. After initial preparation and mounting of the single cell, a minimum OCV of 1.0V was required to continue electrochemical measurements. All electrochemical measurements were taken using a VoltaLab 40 (Radiometer Analytical). Impedance measurements were taken over a frequency range of 100kHz-10mHz from OCV to an overpotential of 400mV at 100mV intervals. Equivalent circuit modeling of impedance data was performed with Zview software. DC current-voltage measurements were conducted using a potential scan rate of 0.25mV/s.

4.3 Results and Discussion

Typical impedance curves obtained during the course of these experiments contain two distinct arcs at the high- and mid- frequency range and a Warburg type element at low-frequencies which traditionally describes diffusional limitations (Section 2.3.3.2.6) Figure 4.1.a shows a typical impedance curve obtained during the course of these experiments on Ni-YSZ anodes in 50 sccm flow of H_2. The Ni-YSZ spectra contained 2 distinct arcs at high and mid- frequencies. A Warburg element or a third arc was

occasionally observed in the mHz range and is not included in these figures. The solid line represents the fit obtained from the ($LR_s[C_1\ (R_1(R_2Q_2)]$) EC (Section 2.3.2.1.6).

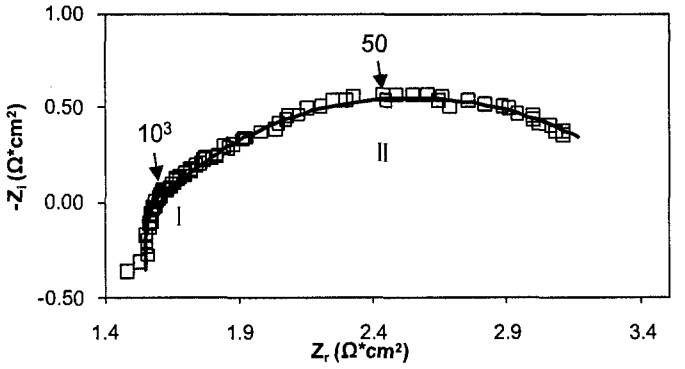

Figure 4.1. a) Typical impedance spectra obtained for Ni-YSZ system at 850°C and 50sccm flow H_2 at OCV (□) Impedance data, (—) Fitted data. The apex of each arc is label with the frequency in Hz

The Warburg element in SOFC's is suggested to be the result of the experimental set-up and has been described as 'gas conversion' impedance.[5,6] Gas conversion impedance would result when there is a stable reference electrode on the opposite side of the working electrode (as in this case). Figure 4.2 shows Nyquist plots of impedance spectra for Ni-YSZ anodes at increasing overpotentials. The third low frequency response is also present in the Co-YSZ samples as a semi-circle (not shown). The low frequency Warburg (or semi-circle) response was not observed at η>200mV, suggesting simple gas diffusion limitations based on Fick's Law should not be used to describe this element. Other possible sources of the low-frequency element may include, but are not limited to, hydrogen and/or oxygen 'diffusion' through the metal and/or electrolyte.[23]

Further analysis on the nature of the third low frequency response was not performed and subsequent discussions regarding equivalent circuit modeling refer to the first two arcs of the spectra. The simplified model proposed by *Fleig et al.* ($LR_s[C_1\ (R_1(R_2Q_2)]$), including an inductance, was used to model the first two arcs found in the impedance data obtained in this work.[2,24-26]

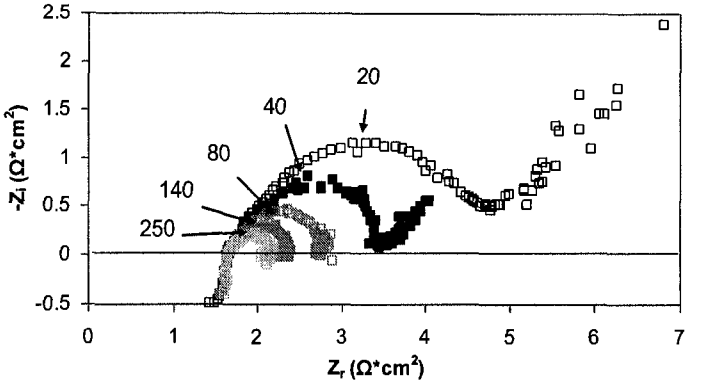

Figure 4.2 Nyquist plot of impedance spectra of Ni-YSZ anode in H_2 at 800°C at various overpotentials (□) OCV, (■)η=100mV, (□)η=200mV, (▣)η=300mV and (□)η=400mV. The apex of each arc is label with the frequency in Hz.

To elucidate the origins of the high- and mid- frequency arcs, a series of temperature and overpotential experiments were performed. Figure 4.3 shows the dependence of each resistance as it related to overpotential for Ni-YSZ and Co-YSZ anodes at 800°C.

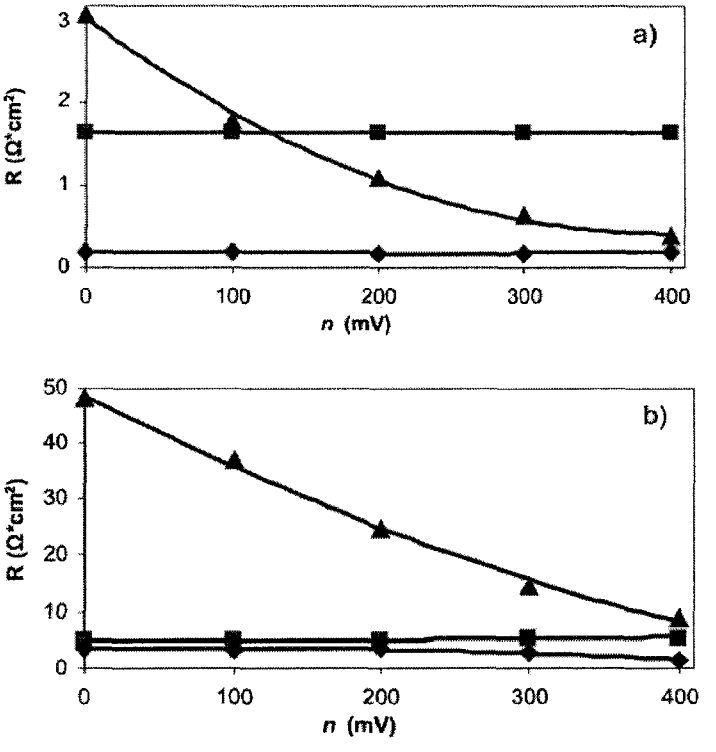

Figure 4.3 Parameters of equivalent circuit as a function of electrode overpotentials for (a) Ni-YSZ system and (b) Co-YSZ system at 800°C. (■)R_s. (♦)R_1 and (▲)R_2

The dc-bias independence of R_s and R_1 strongly indicated that the process associated with R_2 (Process II) was the only arc/process associated with the 'true' electrode processes (i.e. hydrogen oxidation) while the other two may be related to bulk transport. The resulting bias independence of R_s was not surprising since it is associated with the series resistance and represents contact resistances between cell components and conductivities of the electrodes, electrolyte and wires. The process coupled with R_1 (Process I), is not as well established and has not always been distinguished from any additional arcs present in the spectra. However, its bias independence also indicated a resistance and capacitance derived from transport processes rather than charge transfer processes, consistent with previous findings.[1,4]

All processes were activated by temperature (Figure 4.4).

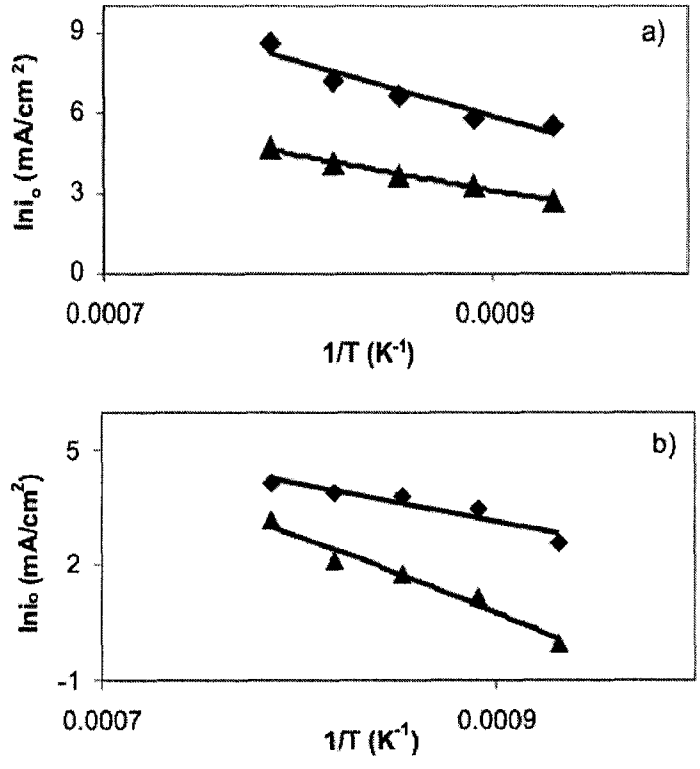

Figure 4.4. Arrhenius plots of the anodic exchange current density on (a) Ni-YSZ and (b) Co-YSZ cermet electrodes at OCV. (♦)Process I and (▲)Process II.

Activation energies and area specific resistances are listed in Table 4.1 for Process I and II, for each anode at OCV at various temperatures.

Table 4.1 Activation parameters obtained from AC measurements for Process I and II for Ni-YSZ and Co-YSZ anodes.

	Process I				Process II			
Temperature (°C)	R_1 (Ω•cm^2)		E_{aR1} (kJ/mol)		R_2 (Ω•cm^2)		E_{aR2} (kJ/mol)	
	Ni	Co	Ni	Co	Ni	Co	Ni	Co
800	0.5	9.0			7.7	120.5		
850	0.4	3.7	-160 +/-	-80	4.4	38.0	-107 +/-	-170 +/-
900	0.2	2.8	30	+/-20	3.2	21.9	4	10
950	0.1	2.7			2.1	16.3		
1000	0.02	2.2			1.3	5.8		

The activation energy for Process I was determined to be 160+/-30 kJ/mol for the Ni-YSZ anode. The tendency for R_1 to decrease with increasing temperature was consistent with previous findings although the activation energy was approximately twice as large as that found for Ni-YSZ anodes in H_2O/H_2 mixtures.[1,4] The Co-YSZ anode exhibited activation energies of 80+/-10 kJ/mol for R_1, which is significantly less than that obtained for Ni-YSZ. Variability in activation for Process I was not unexpected and is readily explained by the process involving transport of charged species between YSZ and metal.[4] Additionally, changes in transport properties between the metal and YSZ interface may be attributed to metal-zirconia solid state reactions which readily occur.[27,28]

The arc associated with process II, which was in the 100Hz range of the impedance spectrum, was strongly bias and temperature dependent. The activation energy associated with process II was 107+/-4 kJ/mol for Ni-YSZ anode and is in concordance with previous findings which range from 110-135kJ/mol.[3,8,11] The apparent activation energy associated with process II of the Co-YSZ anode was one and a half times greater than those reported for the nickel based anode.

The dependency of R_2 on potential (Figure 4.3) strongly suggested this arc represented the processes involved in charge transfer. As mentioned previously, little and conflicting evidence is available in the literature for identifying this process with any certainty and establishing the rate-determining step of this process is yet required. It should be noted that adsorption/desorption processes may also influence the resistances through overpotential however, the large activation energies associated with Process II suggest dissociative H_2 adsorption and H_2O desorption are not the reactions associated with R_2.[29]

The capacitances varied between Process I and II by an order of magnitude for the Ni-YSZ samples and by three orders of magnitude for Co-YSZ at 800°C. The Ni-YSZ capacitances were approximately 0.3 and 9 mF/cm^2 for C_1 and Q_2 at OCV respectively. The Co-YSZ capacitances were approximately 0.002 and 3 mF/cm^2 for C_1 and Q_2 at OCV respectively. Simple model calculations performed by *Primdahl et al.* suggest the capacitance obtained for C_1 of both anodes, are in the realm of a double layer capacitance of the M-YSZ interface. Again suggesting arc I is attributable to transport of ions across the M-YSZ interface. Capacitances obtained from arc II, which are in the 10 mF/cm^2 range, suggest adsorption of charged species on YSZ or metal.[1]

According to the low field approximation of the Butler-Volmer equation and assuming the rate determining step occurs once (i.e $\nu = 1$), the reciprocal charge transfer resistance at low overpotentials is proportional to the exchange current density, i_o

$$i_0 = \frac{RT}{nFR_{CT}} \qquad (4.15)$$

where R is the ideal gas constant, T is temperature, n is the number of electrons involved in the transfer process (where $n = (\alpha_a + \alpha_c)\nu$), F is Faradays constant and R_{CT} is the charge transfer resistance. Therefore exchange current densities obtained from AC data are expected to be the equal to the ones obtained by DC techniques. Figure 4.5 shows an example of iR_s corrected DC measurement for Ni-YSZ and Co-YSZ samples and the subsequent Tafel behavior of each anode. The quantity of R_s was obtained as the high-frequency intercept of the impedance spectrum for each respective temperature.

The overpotential range was not restricted since there was no indication of passivation. Qualitatively it is observed that the cathodic and anodic branches of the current-overpotential curves are not symmetrical. This indicates different reaction kinetics for the hydrogen oxidation reaction (anodic branch) and hydrogen evolution reaction (cathodic branch). Therefore, the assumption that $\alpha \equiv \beta = 0.5$ is not valid and will be examined in more detail.

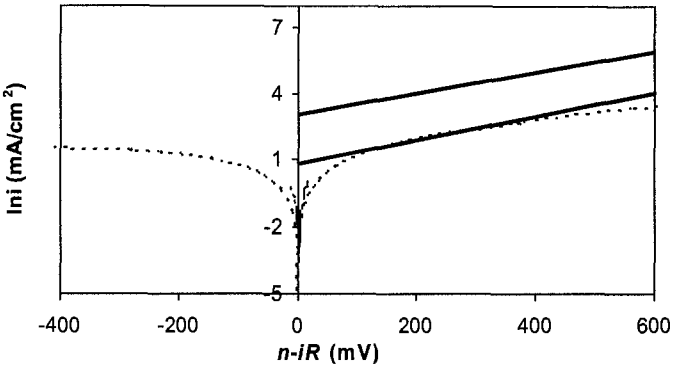

Figure 4.5 ln(current)-potential relations for the hydrogen evolution and oxidation reactions at 800°C for (—) Ni-YSZ and (--) Co-YSZ anodes in pure H_2.

Additionally, even after iR_s compensation it was observed that the ln$i$ vs η plots are curved at high overpotentials. Therefore to choose an appropriate Tafel region three criteria were required: 1) the exchange current densities between DC and AC techniques were comparable 2) the Tafel region began at high overpotentials (i.e. > 180 mV) and 3) the correlation coefficient was >0.99. As an exception, the linear region for Co-YSZ at 800°C started at overpotential less than 180mV as seen in Figure 4.5. Generally, the linear segment ranged approximately 150mV and 0.5 decades. Table 4.2 summarizes all values obtained from AC and DC techniques.

Table 4.2 Comparison of exchange current densities obtained for Ni-YSZ and Co-YSZ anodes via DC and AC techniques and the Lefat slopes at each temperature.

	Ni-YSZ			Co-YSZ		
Temperature (°C)	i_o (EIS) (mA/cm^2)	i_o (DC) (mA/cm^2)	b^{-1} (mV^{-1})	i_o (EIS) (mA/cm^2)	i_o (DC) (mA/cm^2)	b^{-1} (mV^{-1})
800	15	19	0.0049	1	2	0.0072
850	27	32	0.0040	3	3	0.0068
900	39	35	0.0038	6	6	0.0059
950	64	68	0.0025	8	7	0.0059
1000	104	88	0.0024	24	16	0.0046

There is good agreement between the two calculated values, where i_o from impedance data is obtained from the second arc at OCV and i_o is obtained from quasi-steady state DC experiments at high overpotentials, where the DC experiments were run at 0.25 mV/s.

Figure 4.6.a. shows the relationship between the anodic Lefat slope and inverse temperature for both anodes. The traditional relationship between b^{-1} and T^{-1} is not

observed. The slopes for the Ni-YSZ and Co-YSZ samples were 18(+/-3) mV/K and 16(+/-3) mV/K respectively and the y-intercepts were -0.012(+/-0.002) mV^{-1} and -0.008(+/-0.003) mV^{-1}. Additionally, the data in Figure 4.6.b. show that the experimental α calculated at each temperature is not constant with temperature.

Changes in α may be due to an expected temperature dependence, or a result of a change in reaction mechanism, where the rate controlling step may change from charge transfer to adsorption. Additionally, the impact of nonuniform potential in SOFC electrodes and resultant electrokinetic parameters has been explored by Kenney et al.[33] Work by Soderberg et al. suggested the porous nature of the electrodes may also impact the transfer coefficient.[34] Further discussion on these possibilities is given below.

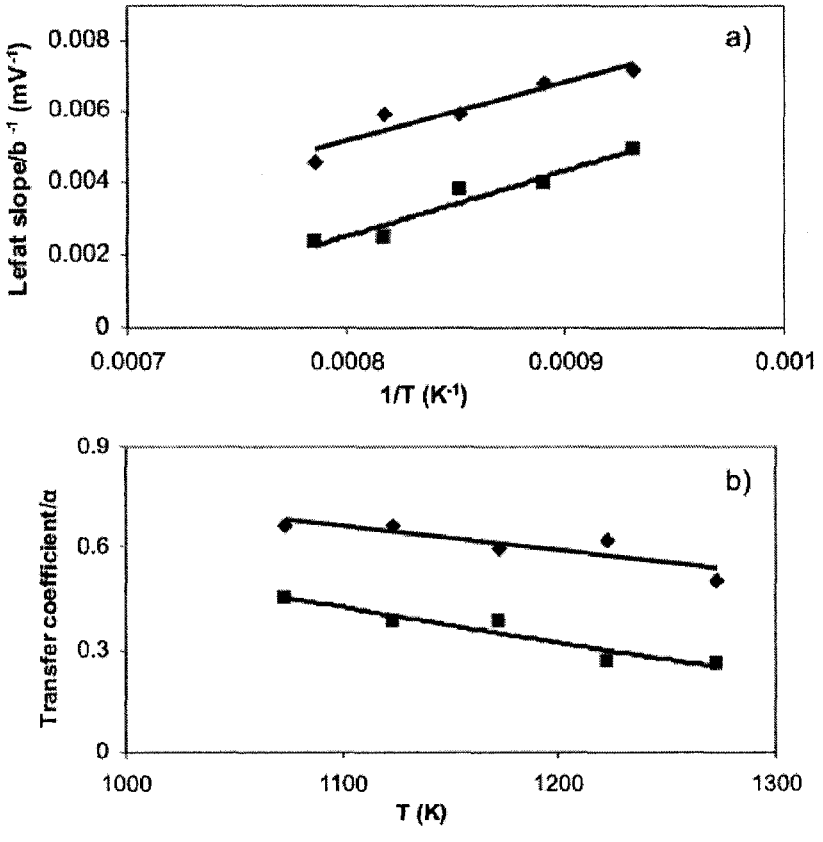

Figure 4.6 (a) Lefat slopes as a function of inverse temperature for (■) Ni-YSZ and (♦) Co-YSZ SOFC anodes. (b) Charge transfer coefficients as a function of temperature for (■) Ni-YSZ and (♦) Co-YSZ SOFC anodes.

Comparisons between the slope and intercept of Equations 4.11 and 4.12 were performed and the y-intercept of Figure 4.6.b. was equal to the α' calculated from $db^{-1}/dT^{-1}=\alpha' F/R$. Table 4.3 shows the resulting α' values for Ni-YSZ and Co-YSZ anodes obtained from Equations 4.11 and 4.12.

Table 4.3 Calculated charge transfer coefficients obtained by the slope ($db^{-1}/dT^{-1}=\alpha' F/R$) of Equation 4.11 and the y-intercept of Equation 4.12.

	α' (Derived from slope of Figure 4.6.a	α' (The y-intercept of Figure 4.6.b
Ni-YSZ	1.5	1.5
Co-YSZ	1.4	1.5

The resulting 'true' transfer coefficient, written as α', is actually 1.5 and was calculated from Equation 4.11 or 4.12, which is fundamentally different from that normally assumed. It should be noted that the 'true' transfer coefficient has a value appreciably different from 0.5 (although the value for Ni-YSZ at 800°C and Co-YSZ at 1000°C are coincidentally similar). Therefore, erroneous conclusions would result if the traditional relationship between b^{-1} and T^{-1} was assumed. Based on apparent transfer coefficients obtained at various temperatures, one could determine that α between Ni-YSZ and Co-YSZ are significantly different and vary by a factor of approximately 1.5 at each temperature. However, by identifying the real form of the Tafel equation and by determining the relationship between α and T, it was observed that the true charge transfer coefficient did not vary between metals and only the temperature independent K-term did. Non-trivial explanations of the significance of the K-term have been offered in the literature.[20,21,30,31] One such explanation to consider is that if the entropy of activation $\Delta S^{o\neq}$ and hence the electrochemical energy of activation are affected through the term $\alpha\eta F$, the Lefat slope is expected to contain a temperature-independent component.[20]

$$\frac{1}{b}=-\frac{d}{d\eta}\left(\frac{\Delta H^{o\neq}-\left[T\left(\Delta S^{o\neq}\pm\alpha\eta F\right)\right]+\alpha'\eta F}{RT}\right) \quad (4.16)$$

$$\frac{1}{b}=-\frac{F}{RT}\left(\alpha'\pm\alpha T\right) \quad (4.17)$$

This result can account for cases where the apparent transfer coefficient linearly increases or decreases with temperature.

The b^{-1} dependence on inverse temperature thereby influences the conventional representations of the activation processes usually described by an Arrhenius type of equation and must be considered. In the case where α' linearly varies with temperature by virtue of the potential dependence of entropy, the traditional Arrhenius equation offered in Equation 4.14 is modified to include the potential dependant term and the temperature dependant α

$$\ln i_n = -\left(\frac{\Delta H^{o\ddagger} - \left[T\left(\Delta S^{o\neq} \pm \left(\alpha' + \frac{KRT}{F} \right) \eta F \right) \right] - \alpha' \eta F}{RT} \right) \quad (4.18)$$

$$\frac{d\ln i_n}{dT^{-1}} = -\left(\frac{\Delta H^{o\neq} - \alpha' \eta F}{R} \pm K \eta T^2 \right) \quad (4.19)$$

At high overpotentials and high temperature, the term $\pm K\eta T^2$ becomes significant and a linear relationship between $\log i_n$ and $1/T$ is no longer expected. Figure 4.7. shows the $\log i_n$ versus T^{-1} relationships of the Ni-YSZ sample tested over 5 overpotentials ranging from 0 to 400mV in 100mV intervals using AC data.

Linearity between the two variables is lost at high overpotentials and temperature. Non-linearity is most noticeable at η=400mV, where $\frac{d \log i_n}{d\eta}$ is larger at higher temperatures, again suggesting a non-traditional α dependence on T through the change in the entropy of activation with temperature and not changes in reaction mechanism or anomalous electrode properties. Additionally, the plot between $\ln i_o$ and η at OCV shows that the relationship remains linear within the whole temperature range, suggesting there is no change in reaction mechanism at higher temperatures.

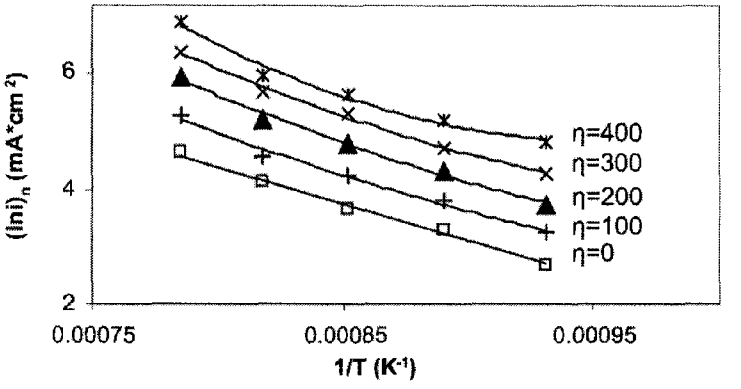

Figure 4.7 Arrhenius plots of anodic exchange current density on Ni-YSZ cermet anodes at various overpotentials and the affect on linearity.

In the case of a reaction involving only one electron transfer, the derived Lefat slopes may be directly related to the characteristics of the transition state determining the reaction rate of the process by evaluating the symmetry factor β. However, when a reaction involves more than one electron, where the transfer steps usually occur in discrete steps, the transfer coefficients may be used to give information on reaction mechanisms. A relationship between the transfer coefficients α and the symmetry factor β is given by the following equations[32]

$$\alpha_a = \frac{\gamma_f}{\nu} + z_{rds}(1-\beta) \qquad (4.20)$$

$$\alpha_c = \frac{\gamma_p}{\nu} + z_{rds}\beta \qquad (4.21)$$

Where the important quantities are the numbers of electrons transferred prior to (γ_p), during (z_{rds}), and following (γ_f) the rate-determining step, and the number of times the rate-determining step occurs (ν). Therefore, if β=0.5 and there is only one electron transfer per rate determining step, a transfer coefficient of 1.5 would suggest a successive two electron transfer, where the first electron transfer is the rate determining step followed by a second transfer.

The same method was used to determine the relationship between α_c and T for the Ni-YSZ anode. The cathodic charge transfer coefficient (for T = 900-1000°C) ranged from 0.6-0.7, as expected from the following relationship

$$\alpha_a + \alpha_c = \frac{n}{\nu} \quad (4.22)$$

where n is the total number of electrons transferred and the other variables are described above.

This work supports the mechanism in which the rate determining step was proposed to involve adsorbed hydrogen and not H^+ and OH^-. However we do not suggest that changes in transfer coefficient values at high temperatures reflect changes in reaction mechanism, but rather to an expected deviation from the assumed constancy of α.

4.4 Conclusion

Determination of the charge transfer coefficients to elucidate mechanistic differences for porous Ni-YSZ and Co-YSZ SOFC anodes was performed. Impedance spectra for both metals resulted in three main components, where the first two processes were associated with transport and faradaic processes respectively. Both processes were activated by temperature and the apparent activation energies for hydrogen oxidation was determined to be 107+/-4kJ/mol and 170+/-10kJ/mol for Ni-YSZ and Co-YSZ respectively.

The temperature dependence of the Lefat slopes were also examined and compared to three previously sited types of dependence. The SOFC anodes resulted in a Type II dependence, where the Lefat slope was linearly proportional to the inverse temperature, but with an additional temperature independent term. This temperature independent term caused significant differences between the traditionally calculated α_a values for each anode at each temperature. The 'true' charge transfer coefficient (α_a'), calculated over a range of 250°C is 1.5 for both Ni-YSZ and Co-YSZ, suggesting the electrochemical oxidation of hydrogen is a two step reaction where the first electron transfer is rate determining for both metals.

References

(1) Primdahl, S.; Mogensen, M. *J. Electrochem. Soc.* **1997**, *144*, 3409.

(2) Fleig, J.; Maier, J. *J. Electrochem. Soc.* **1997**, *144*, L302.

(3) Holtappels, P.; Vinke, I.; Haart, L. d.; Stimming, U. *J. Electrochem. Soc.* **1999**, *146*, 2976.

(4) Kek, D.; Mogensen, M.; Pejovnik, S. *J. Electrochem. Soc.* **2001**, *148*, A878.

(5) Primdahl, S.; Mogensen, M. *J. Electrochem. Soc* **1999**, *146*, 2827.
(6) Primdahl, S.; Mogensen, M. *J. Electrochem. Soc.* **1998**, *145*, 2431.
(7) Aaberg, R. J.; Tunold, R.; Odegard, R. *Solid State Ionics* **2000**, *136-137*, 707.
(8) Sukenshini, A. M.; Habibzadeh, B.; Becker, B. P.; Stoltz, C. A.; Eichhorn, B. W.; Jackson, G. S. *J. Electrochem. Soc.* **2006**, *153*, A705.
(9) Holtappels, P.; Bradley, J.; Irvine, J.; Kaiser, A.; Mogensen, M. *J. Electrochem. Soc.* **2001**, *148*, A923.
(10) Jiang, S.; Badwal, S. *J. Electrochem. Soc.* **1997**, *144*, 3777.
(11) Holtappels, P.; Haart, L. d.; Stimming, U. *J. Electrochem. Soc.* **1999**, *146*, 1620.
(12) Keech, P. G.; Trifan, D. E.; Birss, V. I. *J. Electrochem. Soc.* **2005**, *152*, A645.
(13) Bessler, W. G.; Warnatz, J.; Goodwin, D. G. *Solid State Ionics* **2007**, *177*, 3371.
(14) Mizusaki, J.; Tagawa, K.; Isobe, K.; Tajika, M.; Koshiro, I.; Maruyama, H.; Hirano, K. *J. Electrochem. Soc.* **1994**, *141*, 1674.
(15) Butler, J. *Trans. Faraday Soc.* **1923**, *19*, 729.
(16) Butler, J. *Trans. Faraday Soc.* **1932**, *28*, 379.
(17) Erdey-Gruz, T.; Volmer, M. *Z. Phys. Chem. A.* **1930**, *150*, 203.
(18) Erdey-Gruz, T.; Wick, H. *Z. Phys. Chem. A.* **1932**, *162*, 53.
(19) Conway, B. E. The Temperature and Potential Dependence of Electrochemical Reaction Rates and the Real Form of the Tafel Equation. In *Modern Aspects of Electrochemistry*; Bockris, J. O. M., Ed.; Plenum Press: New York, 1985; Vol. 16; pp 103.
(20) Conway, B.; Tilak, D. M. B. *Trans. Faraday Soc.* **1969**, *66*, 1203.
(21) Conway, B.; Salomon, M. *J. Chem. Phys.* **1964**, *41*, 3169.
(22) Post, B.; Hiskey, C. *J. Am. Chem. Soc.* **1950**, *72*, 4203.
(23) Holtappels, P.; Vinke, I.; Haart, L. d.; Stimming, U. *J. Electrochem. Soc.* **1999**, *146*, 2976.
(24) Fleig, J. *J. Electroceram.* **2004**, *13*, 637.
(25) Fleig, J.; Maier, J. *J. Electroceram.* **1997**, *1*, 73.
(26) Fleig, J.; Pham, P.; Sztulzaft, P.; Maier, J. *Solid State Ionics* **1998**, *113-115*, 739.
(27) Dongare, M.; Malshe, K. M.; Gopinath, C. S. *Electrochem. Soc. Proceedings* **2002**, *2002-5*, 79.
(28) Dongare, M. K.; Dongare, A. M.; Tare, V.; Kemnitz, E. *Solid State Ionics* **2002**, *153-153*, 455.
(29) Hecht, E. S.; Gupta, G. K.; Zhu, H.; Dean, A. M.; Kee, R. J.; Maier, L.; Deutschmann, O. *J. Appl. Catal. A* **2005**, *295*, 40.
(30) Conway, B.; Tessier, D.; Wilkinson, D. *J. Electrochem. Soc.* **1989**, *136*, 2486.
(31) Gileadi, E. *J. Electrochem. Soc.* **1987**, *134*, 117.
(32) Lefebvre, M. C. Establishing the Link Between Multistep Electrochemical Reactio Mechanisms and Experimental Tafel Slopes. In *Modern Aspects of Electrochemistry*; White, R. E., Ed.; Plenum Publishers: New York, 1999; Vol. 32; pp 249.
(33) Kenney, B.; Karan K. *J. Electrochem Soc.* **2006,** *153,* A1172.
(34) Soderberg, J.N.; Co A.C.; Sirk, A.H.C.; Birss V.I. *J. Phys. Chem. B.* **2006,** *110*, 10401.

5. Electrochemical Characterization of Ni- and Co- YSZ anodes in H_2S/H_2 Fuel

Abstract

Single cell solid oxide fuel cell experiments using Ni-YSZ and Co-YSZ anodes were performed to examine their performance in H_2S/H_2 mixtures. Introduction of 10 v/v% H_2S in the fuel stream resulted in anodes which initially showed significant signs of degradation. However, when all of the metal was changed to metal-sulfide, the performance was rectified suggesting metal-sulfides are viable anode materials for SOFC systems. Electrochemical experiments, mass spectrometry of the exhaust gas and XRD of the post run anodes indicate the main reaction is hydrogen oxidation in both fuel streams. DC experiments at various temperatures were performed to determine the inverse Tafel slope (Lefat slope) and the resulting charge transfer coefficients for NiS- and CoS-YSZ anodes. The charge transfer coefficient was determined to be 1.5 for NiS-YSZ anode suggesting the rate determining step of hydrogen oxidation on these anodes is the electron transfer between H_{ad} and O^{2-}. CoS-YSZ exhibited traditional Tafel behavior such that α remained constant over a wide temperature range but yielded a charge transfer coefficient much less than that of the other anodes (α=0.21+/-0.04).

5.1 Introduction

Solid oxide fuel cells (SOFC) are the most flexible fuel cells with respect to fuel selection. They have great potential for generating power from many sources including, hydrogen, hydrocarbons, syngas and biogas.[1-3] Utilizing hydrocarbons as fuels has procured much attention recently due to their natural abundance, easy transport and accessibility making SOFCs an ideal bridging technology towards H_2 utilization. However, fuel impurities, especially sulfur compounds, which are found in most hydrocarbon feed stocks, cause degradation of the anodes, affecting the overall performance of the fuel cell. Therefore, it has been of interest to examine the sulfur tolerance of SOFC anodes by understanding the sulfur poisoning mechanism and to develop sulfur tolerant anodes for SOFC systems.

Ni-YSZ based systems have shown little tolerance to fuels containing low (ppm) H_2S concentrations, where sulfur tolerance decreased with lower operating temperatures and higher H_2S concentrations.[4,5] However, up to 90% recovery of these systems occurred when H_2S was removed from the fuel, signifying that poisoning is caused by blocking of active Ni-YSZ sites by either adsorbed sulfur or H_2S. The small irreversible component was suggested to be the result of Ni-S formation.[5,6] Further studies of nickel-sulfide interactions by Raman

spectroscopy at high temperatures showed that Ni-S is the prevalent species at SOFC operating conditions.[7]

Due to the incompatibility of Ni-YSZ based systems with sulfur, emphasis has recently been placed on improving tolerance of SOFC anodes by changing their composition. Ni-based anodes, where the electrolyte component was changed from yttria-stabilized zironia (YSZ) to scandia-stabilized zirconia (SSC) showed increased tolerance at 100ppm H_2S concentrations at 800°C.[4] Additionally, Cu-ceria anodes exhibited high sulfur tolerance and were able to operate at levels up to 450ppm at 800°C without any appreciable loss in performance.[8] An alternative approach was to utilize perovskite structures which support oxide-ion vacancies to give good oxide-ion conduction and have a mixed-valent cation from the 4d or 5d block which provides good electronic conduction, while exhibiting high sulfur tolerance. The double perovskites $Sr_2Mg_{1-x}Mn_xMoO_{6-\delta}$ showed long term stability in 50ppm H_2S/H_2 at 800°C, without formation of sulfur species.[9] Other perovskites also showed potential by exhibiting sulfur tolerance at 1000°C for up to 8 hours in a 1%H_2S/H_2 mixture.[10] Although these anode materials showed promise in H_2S/H_2 fuel mixtures at low concentrations, little evidence on their long term performance at high sulfur concentrations is available.

Alternatively, the ability to electrochemically oxidize H_2S in a fuel cell has also been established. This was first demonstrated by *Pujare et al.* by utilizing thiospinel $CuFe_2S_4$ as the anodes electrocatalytic site and pure H_2S as fuel.[11] Additionally, anode catalysts comprising of composite metal sulfides derived from a mixture of sulfides of Mo and other transition metals (Fe, Co, Ni) were stable and effective electrocatalysts for conversion of H_2S in SOFC's, with Co-Mo-S exhibiting superior activity and longevity.[12,13] Although these data suggested metal-sulfides are viable SOFC anodes for H_2S containing fuels, very little is understood regarding the H_2S oxidation reaction, which was emphasized by larger than expected OCV values obtained in these cases.

When utilizing H_2S as fuel with an oxide-conducting electrolyte the reaction that takes place at the cathode is the same as in the conventional case when hydrogen is used and is represented by the following equation

$$1/2O_2 + 2e^- \rightleftarrows O^{2-} \quad (5.1)$$

After migration through the electrolyte the oxide ions can react with hydrogen sulfide in two ways

$$H_2S + O^{2-} \rightleftarrows H_2O + \tfrac{1}{2} S_2 + 2e^- \quad (5.2)$$

$$H_2S + 3O^{2-} \rightleftarrows H_2O + SO_2 + 6e^- \quad (5.3)$$

where the reversible potentials are 0.726V and 0.750V at 800°C respectively. The process may further be complicated by thermal decomposition of hydrogen sulfide to sulfur and hydrogen via

$$H_2S \rightleftarrows H_2 + \tfrac{1}{2} S_2 \quad (5.4)$$

thereby introducing hydrogen which may also be oxidized. Therefore higher than expected OCV values (~1V) observed in these systems may be explained by the reaction of H_2. Moreover, the products of Equations 5.2 and 5.4 may be further oxidized

$$1/2\ S_2 + 2O^{2-} \rightleftarrows SO_2 + 4e^- \quad (5.5)$$

Reactions between excess H_2S and SO_2 may also take place via the second step of the Claus process

$$2\ H_2S + SO_2 \rightleftarrows 2H_2O + 3/nS_n \quad n=2\text{-}8 \quad (5.6)$$

where n is the average molecular species of the sulfur product. Since reaction 5.6 is an equilibrium reaction favoured at low temperatures and high SO_2 partial pressures, significant H_2O and S_n production is not expected at high H_2S concentrations and SOFC operating temperatures.

By studying the product distribution of the H_2S, Pt|$(Ce_2)_{0.8}$)($SmO_{1.5}$)|Pt, air system, *Peterson et al.* suggested complete oxidation of hydrogen sulfide to sulfur dioxide was the preferred product.[14] However, it was impossible to determine whether the reaction took place via a two step (via Equations 5.2 and 5.5) or one step process (via Equation 5.3) since both require a $6e^-$ transfer.

Since SOFC operation in the presence of H_2S/H_2 fuel mixtures represents a complex electrochemical process where oxidation of hydrogen has been shown to be strongly influenced by the presence of H_2S, a detailed study to determine the electrochemical reactions involved is necessary. This chapter describes the performance of Ni-YSZ and Co-YSZ anodes subjected to 10%v/v H_2S/H_2 fuel over an extended period of time. Product analysis via mass spectrometry as well as post run anode analysis elucidated the nature of the active anode, while electrochemical impedance spectroscopy and linear sweep voltammetry at various temperatures was used to determine fundamental kinetic parameters, such as the anodic charge transfer coefficient α_a and electrochemical activation energies.

5.2 Experimental

The fuel cell was prepared by mixing Triton X-100 (Research Chemical Ltd)/water and 1g of anode powder. The YSZ supported metal (M-YSZ) (55wt%) anode materials were prepared via co-precipitation by dissolving the appropriate amounts of $ZrCl_4$, Y_2O_3 (dissolved in 10ml of 37wt% HCl) and $NiCl_2 \cdot 6H_2O$ or $CoCl_2 \cdot 6H_2O$ (Aldrich) in 165 ml of distilled water. To ensure YSZ phase purity and stability, anode materials were synthesized with 21 mol% YSZ. The precipitation was achieved through introduction of 2M NaOH (Aldrich) to a final pH of 13. Following precipitation, the product was filtered, washed, dried at 120°C and calcined at 750°C for 2h.

0.15g of the slurry was coated onto an YSZ green-disk (Tosoh) and heated to 1400°C for 4h in air. A 70wt% LSM/30wt%YSZ mixture (LSM, Nextech Materials; YSZ, Tosoh) was used as the cathode and reference electrode material. The cathode was prepared by coating 0.15g of the LSM/YSZ powder symmetrically opposing the sintered anode, while the reference electrode was approximately 4mm to the side of the cathode. After sintering, the YSZ electrolyte was 0.5mm thick and the area of the electrodes were $0.4cm^2$ for the anode and cathode and $0.2cm^2$ for the reference electrode.

All electrochemical measurements were performed in pure hydrogen or in a 10%v/vH_2S/H_2 mixture at 800°C to 1000°C using intervals of 50°C. Hydrogen and hydrogen

sulfide flows were regulated by mass flow controllers (MKS) to a total flow of 50sccm. After initial preparation, mounting and reduction of the single cell, a minimum OCV of 1.0V was required to continue electrochemical measurements. All electrochemical measurements were taken using a VoltaLab 40 (Radiometer Analytical). Impedance measurements were taken over a frequency range of 100kHz-10mHz from OCV to an overpotential of 400mV at 100mV intervals. Equivalent circuit modeling of the impedance data was performed with Zview software. DC current-voltage measurements were conducted using a potential scan rate of 0.25mV/s. The exhaust gas was monitored using an AccuQuad residual gas analyzer. Post-run analysis of the fuel cell anodes was accomplished by X-ray diffraction (XRD) (Phillips PW1830) using CuKα radiation with a wavelength of 1.54Å. The scan range was $2\Theta = 20^{\circ}$ to 90° at a rate of $0.02^{\circ}\ s^{-1}$. Crystalline phases were assigned using the Powder Diffraction File (PDF) database (ICCD, 2001, Dataset 1-51). NanoLab7 SEM with Kevex EDS was used for elemental analysis.

5.3 Results and Discussion

5.3.1 Performance of Ni-YSZ and Co-YSZ anodes in H_2 and H_2S/H_2

Figure 5.1 shows the dependence of each resistance as it relates to overpotential for the Ni-YSZ anode at 850°C in H_2S/H_2 after significant exposure time (15h) obtained from impedance data.

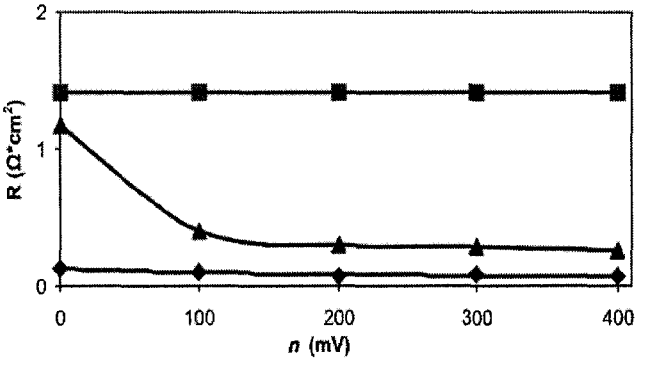

Figure 5.1 Parameters of equivalent circuit as a function of electrode overpotentials for Ni-YSZ system 850°C in 10% v/vH_2S/H_2. (■)R_s. (♦)R_1 and (▲)R_2

It shows the same overpotential trends as those found with the H_2, Ni-YSZ system, suggesting interpretation of impedance spectra remains similar to that found in hydrogen, where R_s and R_1 may be related to non-faradaic processes and R_2 to charge transfer processes.

The progression of impedance behaviour is shown in Figure 5.2 for Ni-YSZ and Co-YSZ anodes with time after H_2S addition.

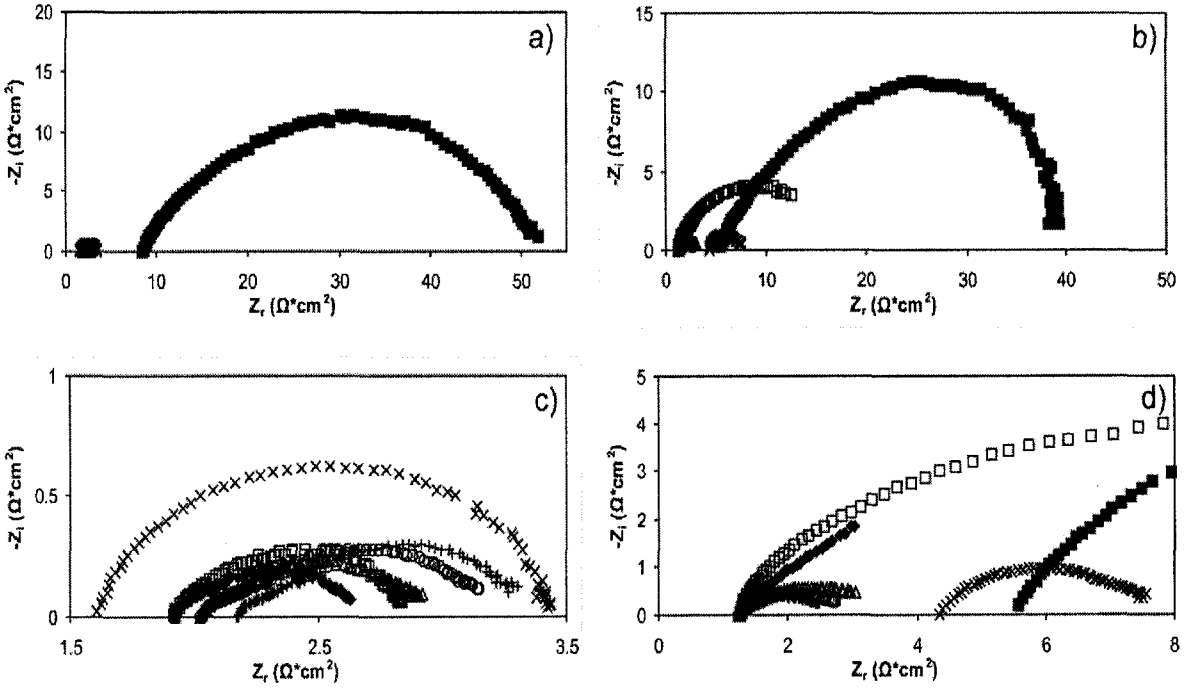

Figure 5.2 Impedance plots of (a) Ni-YSZ and (b) Co-YSZ anodes in H_2S/H_2 at OCV, T=850°C at various times. (x) t=0 (H_2 only), (■) t=1min, (□) t=1.5 hours, (♦) t=3 hours, (Δ) t=5hours, (○) t=10 hours, (+) t=15 hours. (c) and (d) are expanded images of (a) and (b) respectively.

The first measurement was taken with hydrogen as fuel. The impedance spectra exhibit two overlapping depressed arcs at the high- and mid- frequency range. The results indicated the Ni-YSZ and Co-YSZ cermet anodes were initially degraded by the sulfide impurity. All resistances for both anodes increased when H_2S was added to the fuel stream (t=1min). However, after t=1.5h the resistances noticeably decrease. After t=3h the resistances remain relatively constant and are significantly smaller than those obtained when H_2 was the fuel. Interestingly, the R_s values also significantly change after H_2S addition. Convergence of R_s for the Co-YSZ anode to a value that was approximately half the original indicated improved contact between fuel cell components or decreased electrolyte resistance. Increased electrical conductivity of the anode was excluded as a source of decreased R_s since most metal sulfides are small band gap semiconductors and are expected to have a lower electrical conductivity than the metals.[15] Cross-sectional SEM/EDX analysis of the post run SOFC showed the

absence of sulfur in the YSZ electrolyte, demonstrating that conversion from metal to metal-sulfide influenced the serial resistance by improving contact between anode and electrolyte. However, the same trend was not present in the Ni-YSZ system, where the R_s increased from 1.6 to 2.2 $\Omega \cdot cm^2$ after H_2S addition and may be directly linked to the instability of the anode at high temperatures due to the low melting temperatures of nickel sulfides ($T_m(Ni_3S_2)$=787°C and T_m(NiS)=976°C). In comparison, the melting temperature of CoS (1182°C) would account for the higher stability seen in the cobalt anodes.

R_2 resistances, associated with the charge transfer process also noticeably changed when H_2S was added to the fuel stream. R_2 for Ni-YSZ decreased from 2.0 $\Omega \cdot cm^2$ in hydrogen to 1.1 $\Omega \cdot cm^2$ after 15hrs of 10 %v/vH_2S/H_2 exposure. The Co-YSZ anode exhibited a drastic increase in exchange current densities where R_2 decreased from 4.5 to 1.4 $\Omega \cdot cm^2$ in hydrogen and H_2S/H_2 respectively.

XRD analysis of post run anodes indicated addition of high levels of H_2S into the fuel stream resulted in anodes consisting of Ni-S and Co-S species. More specifically, the Ni-YSZ anode consisted of mostly Ni_3S_2 (PDF# 44-1418) with traces of $Ni_{1-x}S$(PDF# 02-1273), while the Co-YSZ anode was $Co_{1-x}S$(PDF# 25-1081) with traces of Co_9S_8(PDF# 02-1459). Presence of metal-sulfide species demonstrated the metals were converted to metal sulfides during operation when H_2S was introduced. However, the phases present at room temperature are not assumed to be the electrode present during fuel cell operation at high temperatures. In situ analysis is required to determine the exact species of M-S present during operation. Sulfidation studies of cobalt and nickel suggest the active species at fuel cell operating temperatures are $Co_{1-x}S$ and $Ni_{3+x}S_2 + Ni_{1-x}S$ respectively.[16,17] Since the exact metal sulfide species at high temperatures is not known, the sulfide anodes synthesized in-situ by H_2S addition are hereby referred to as to as NiS- and CoS-YSZ.

Increased polarization of the anode during the first minutes of H_2S introduction is consistent with results obtained previously with low concentrations of H_2S in H_2 and may be the result of initial blocking of reactive sites by sulfur species or by agglomeration of metal particles accelerated by the presence of sulfur thereby decreasing the TPB. With increased exposure time, all the metal was converted to metal-sulfide and a decrease in polarization was observed. This suggested the deactivation observed at low concentrations over short periods of time was a result of the transition between metal and metal-sulfide phases. Once all the metal was converted, the active metal-sulfide catalyst was used as a viable anode material for H_2S containing fuels. However, the reduction of metal-sulfide back to metal is

possible. Therefore, to maintain the structural and compositional purity of metal-sulfide anodes, H_2S would continuously be required in the fuel stream.

Very little is known regarding the actual electrochemical oxidation of H_2S to SO_2, particularly if the reaction is complicated by the presence of another fuel such as H_2. Analysis of exhaust gas by mass spectrometry indicated there was not a significant amount of SO_2 produced and was below the detection limit of the instrument (P_{SO_2}/P_{tot}=0.001), suggesting the main fuel was actually H_2 and not H_2S. Additionally, there was no evidence of solid sulfur formation once the fuel cell was examined after a 15 hour period, except for the metal-sulfide anodes themselves. Therefore, the main increase in performance over time was due to the ability of metal-sulfide electrodes to oxidize hydrogen at an appreciable and continuous rate. This is in agreement with OCV values obtained when H_2S/H_2 was used as fuel. The OCVs of the Ni-YSZ and Co-YSZ anodes in H_2S/H_2 at 850°C were 1.1V and 1.2V, respectively. The slight discrepancy between OCV values of each anode was attributed to irreproducibility of the seal between fuel cells. These values are similar to ones obtained when H_2 was the fuel (1.2V for both anodes) and are significantly different from OCVs calculated from thermodynamic data for the oxidation of H_2S (0.75V) at 850°C. Although small contributions from the oxidation of H_2S cannot fully be excluded, based on the aforementioned observations, all corresponding kinetic analysis assumes the oxidation of hydrogen on metal-sulfides is the main electrochemical reaction.

Figure 5.3 shows the SEM/EDX analysis of post-run anodes tested in 10%v/v H_2S/H_2. Figure 5.3.a shows a portion of the Ni-based anode which was removed from the electrolyte. Large crystal species ranging in size from 2-100*u*m (100*u*m not shown) in diameter were present throughout the anode. EDX shows the large crystalline particles were NiS- while the less compact 'meshy' part was a combination of NiS- and YSZ. The SEM cross-sections of the Co-based anodes in Figure 5.3.b show phase segregation toward the electrolyte not observed prior to fuel cell operation. A dense layer consisting of CoS- was next to the dense YSZ, while the porous structure on the top of this consisted of CoS- and YSZ. This segregation of dense, non-porous CoS- towards the electrolyte would significantly decreased the triple phase boundary between metal, YSZ and gas. Improvement of NiS- and CoS- microstructure should result in fuel cell anodes with higher current densities than those of the well-known Ni-based anodes.

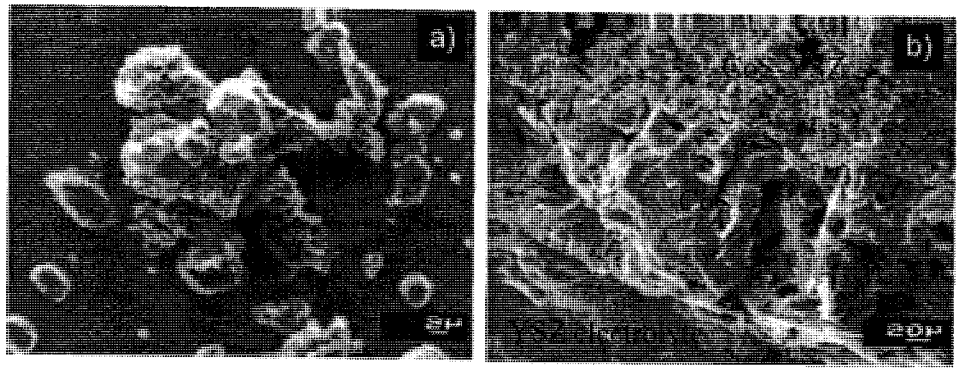

Figure 5.3 SEM images of anodes' microstructure after operating at 850°C for 15hours in 10%v/v H_2S/H_2. a) Section of Ni-YSZ anode b) Cross-section of Co-YSZ on dense YSZ electrolyte showing phase segregation of newly formed CoS- toward the electrolyte.

5.3.2 Hydrogen oxidation on NiS- and CoS- YSZ

Figure 5.4 shows an example of iR_s corrected DC measurement for Ni-YSZ and Co-YSZ samples under H_2S/H_2 and the subsequent Tafel behavior of each.

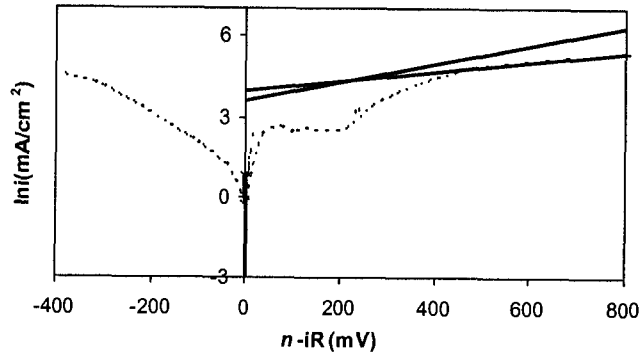

Figure 5.4 ln(current)-potential relations for the hydrogen evolution and oxidation reactions at 850°C for (—) Ni-YSZ and (- -) Co-YSZ in 10 %v/v H_2S/H_2.

Linear voltammograms for the H_2S/H_2 system were obtained after 15h of exposure to assure all the metal had converted to metal-sulfide. The quantity of R_s was obtained as the high-frequency intercept of the impedance spectrum for each respective temperature. Qualitatively it was observed that near OCV, before reaching Tafel behavior, an anodic peak was observed for both anodes in H_2S/H_2 atmospheres that were not present when H_2 was the fuel. An enlarged partial LSV of this region demonstrated it consisted of at least two overlapping peaks (Figure 5.5.a). Previous cyclic voltammetry experiments on similar

samples performed in this laboratory show that the process was irreversible in H_2S atmospheres (Figure 5.5.b).

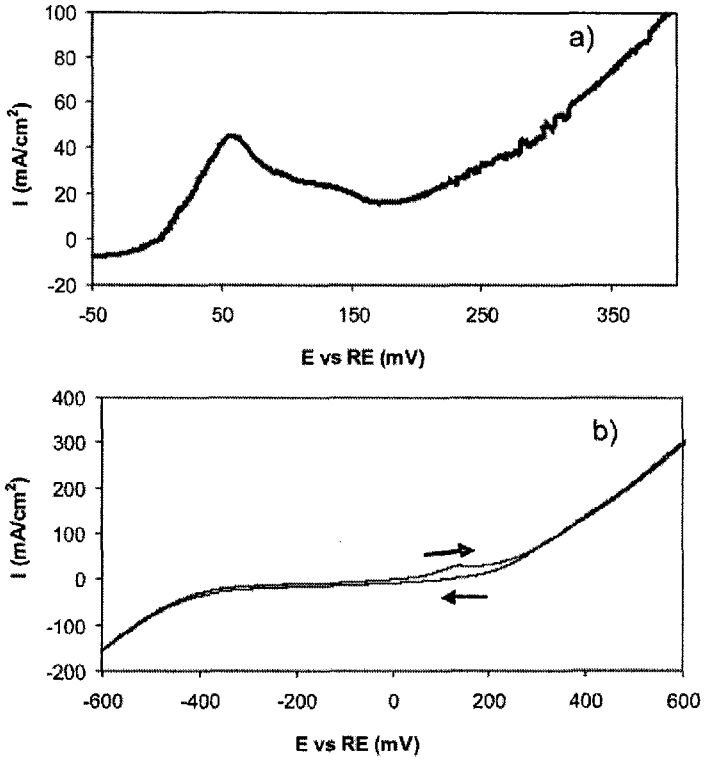

Figure 5.5 a) Enlarged LSV of Ni-YSZ in 10%v/v H_2S/H_2 atmospheres at 850°C. b) Full range CV of similar anode (Co-YSZ) in H_2S contaminated fuel at 850°C.

CV studies at various scan rates, temperatures and partial pressures are required to fully determine the nature of these peaks, however, previous studies on Cu_2S by *Nava et al.* suggest they may be related to serial oxidation of the metal-sulfides through defective sulfides.[18]

Figure 5.6 shows the relationship between the charge transfer coefficient and temperature for both anodes in H_2S/H_2 atmospheres obtained in the same manner as described in Chapter 4.

The traditional relationship between α and $T$was not observed and is more readily described by Equation 4.12 for all but one of the anodes. The CoS-YSZ anode exhibited a relatively constant α at all temperatures, (0.21+/-0.04), as per Equation 4.9, where the traditional relationship between b^{-1} and T^{-1} was observed.

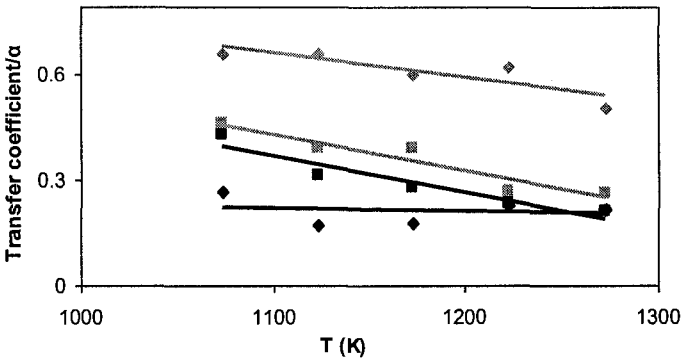

Figure 5.6 Charge transfer coefficients as a function of temperature for (■) NiS-YSZ and (♦) CoS-YSZ SOFC anodes. Charge transfer coefficients for (■) Ni-YSZ (♦) Co-YSZ in H_2 are given for comparison.

Table 5.1 includes the resulting α' values and their temperature dependence for NiS- and CoS-YSZ SOFC anodes for hydrogen oxidation.

Table 5.1 Summary of electrochemical data for NiS- and CoS-YSZ SOFC anodes.

	NiS-YSZ				CoS-YSZ			
Temp (°C)	b^{-1} (mV^{-1})	α'	$\alpha f(T)$	E_a (kJ/ mol)	b^{-1} (mV^{-1})	α'	α $f(T)$	E_a (kJ/ mol)
800	0.0046	1.5	$\alpha = \alpha' + \frac{KRT}{F}$	130 +/-10	0.0028	0.2	$\alpha = \alpha'$	220 +/-60
850	0.0032				0.0019			
900	0.0028				0.0017			
950	0.0022				0.0022			
1000	0.0019				0.0019			

The 'true' transfer coefficient (α'=1.5) has a value appreciably different from 0.5, which is normally assumed. Furthermore, the 'true' transfer coefficient is substantially different from the apparent transfer coefficients obtained at various temperatures, where the measured α's ranged from 0.26-0.46, 0.50-0.66 and 0.20-0.42 for Ni-, Co- and NiS-YSZ respectively. By identifying the real form of Tafel and determining a relationship between α and T, it was determined that the charge transfer coefficient does not vary between anodes and only the temperature independent K-term does.

Based on the relationship between α and β proposed by *Bockris and Reddy*[19] if β=0.5 and there is only one electron transfer per rate determining step, a transfer coefficient of 1.5

would suggest a successive two electron transfer, where the first electron transfer is rate determining and the second electron transfer follows it, consistent with previous findings for hydrogen oxidation on Ni- and Co-YSZ.

The charge transfer coefficient did not change with temperature for CoS-YSZ and resulted in an average value of 0.21+/-0.04 for α. This suggested a different rate determining step for hydrogen oxidation involving the CoS anode which is not easily determinable by Equation 4.20 and possibly involves factors associated with adsorption kinetics, where the rate determining step may include the dissociation of reactants or recombination of products on the surface.[19]

All processes were activated by temperature. Activation energies were calculated using temperature dependence of $\ln i_o$. Figure 5.7 examines the relationship between $\ln i_o$ and temperature for NiS- and CoS-YSZ anodes.

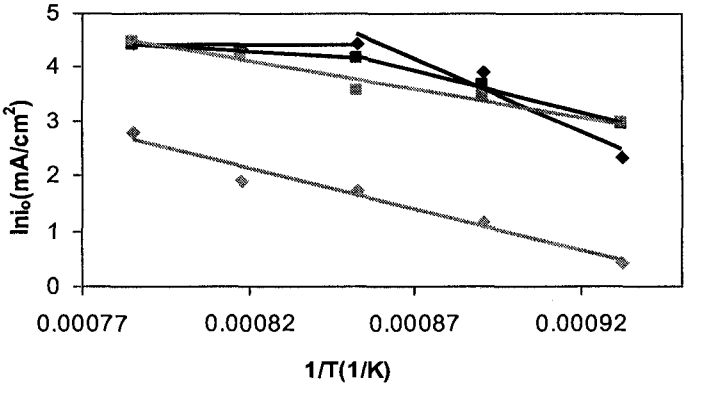

Figure 5.7 Arrhenius plots of anodic exchange current density on (■) NiS-YSZ and (♦) CoS-YSZ SOFC anodes. (▩) Ni-YSZ (◈) Co-YSZ in H_2 are given for comparison.

Linearity existed within the whole temperature range for H_2 oxidation on metals (Chapter 4) at OCV. For metal-sulfide systems, Arrhenius behavior was present in the temperature range of 800°C to 900°C. At temperatures above 900°C the exchange current density did not change significantly with temperature. Activation energies for the NiS-YSZ and CoS-YSZ systems were 130+/-10kJ/mol and 220+/-60kJ/mol respectively. The activation energy associated with NiS-YSZ was slightly larger than the one for Ni-YSZ, but is in the range previously reported for hydrogen oxidation.[1,20,21] The activation energy associated with CoS-YSZ was significantly larger than those energies previously reported; again suggesting a different rate determining step.

5.4 Conclusion

Metal sulfides, specifically NiS- and CoS-YSZ anodes were shown to be active over long periods of time for the hydrogen oxidation reaction. Impedance analysis demonstrated an initial decrease in SOFC performance when H_2S was added to the fuel stream, but after approximately 3 hours, when all of the metal was converted to metal-sulfide, the performance was rectified, suggesting metal-sulfides are viable anode materials for SOFC systems. CoS-YSZ anodes are preferential to NiS-YSZ due to their higher melting temperature, stability and activity. Mass spectrometry and electrochemical results showed the main fuel was H_2 as opposed to H_2S and subsequent kinetic analysis on metal and metal-sulfide systems for oxidation of hydrogen at various temperatures followed.

Proper determination of the charge transfer coefficients to elucidate mechanistic differences for NiS- and CoS- YSZ SOFC anodes was performed. Impedance spectra for both anodes resulted in two main components, where the two processes were associated with charge transport and faradaic processes respectively. Temperature dependence of Tafel slopes were examined and compared to three types of temperature dependence. The NiS-anodes resulted in a Type II dependence, similar to that of the Ni- and Co-YSZ systems, where the Lefat slope was linearly proportional to the inverse temperature, but with an additional temperature independent term. The CoS- anode exhibited traditional dependence, where α was constant over the temperature range tested. The 'true' α calculated over a 250°C range was 1.5 for NiS-YSZ, signifying the electrochemical oxidation of hydrogen is a two step reaction where the first electron transfer is rate determining. The CoS-YSZ anode exhibited a constant α, 0.21+/-0.04 at all temperatures, suggesting a complex rate determining step for hydrogen oxidation on CoS anodes.

References

(1) Sukeshini, A. M.; Habibzadeh, B.; Becker, B. P.; Stoltz, C. A.; Eichhorn, B. W.; Jackson, G. S. *J. Electrochem. Soc.* **2006**, *153*, A705.

(2) Zhu, W.; Deevi, S. *Mater. Sci. Eng.* **2003**, *A362*, 228.

(3) Gorte, R. J.; Park, S.; Vohs, J. M.; Wang, C. *Adv. Mater.* **2000**, *12*, 1465.

(4) Sasaki, K.; Susuki, K.; Iyoshi, A.; Uchimura, M.; Imamura, N.; Kusaba, H.; Teraoka, Y.; Fuchino, H.; Tsujimoto, K.; Uchida, Y.; Jingo, N. "Sulfur Tolerance of Solid Oxide Fuel Cells"; International Symposium of Solid Oxide Fuel Cells IX (SOFC-IX), 2005, Quebec City, Quebec.

(5) Matsuzaki, Y.; Yasuda, I. *Solid State Ionics* **2000**, *132*, 261.

(6) Xia, S.; Birss, V. "Deactivation and Recovery of Ni-YSZ anode in H_2 fuel containing H_2S"; International Proceedings of Solid Oxide Fuel Cells IX (SOFC-IX), 2005, Quebec City, Quebec.

(7) Dong, J.; Zha, S.; Liu, M. "Study of Sulfur-Nickel Interactions Using Raman Spectroscopy"; International Symposium on Solid Oxide Fuel Cells-IX (SOFC-IX), 2005, Quebec City, Quebec.

(8) He, H.; Gorte, R. J.; Vohs, J. M. *Electrochem. Solid State Lett.* **2005**, *8*, A279.

(9) Huang, Y. H.; Dass, R. I.; Xing, Z.-L.; Goodenough, J. B. *Science* **2006**, *312*, 254.

(10) Mukundan, R.; Brosha, E. L.; Garzon, R. H. *Electrochem. Solid State Lett.* **2004**, *7*, A5.

(11) Pujare, N. U.; Semkow, K. W.; Sammells, a. F. *J. Electrochem. Soc.* **1987**, *134*, 2639.

(12) Liu, M.; Wei, G.; Luo, J.; Sanger, A. R.; Chuang, K. T. *J. Electrochem. Soc.* **2003**, *150*, A1025.

(13) Wei, G.; Luo, J.; Sanger, A.; Chuang, K. *J New Mater. Electochem. Systems* **2005**, *8*, 59.

(14) Peterson, D. R.; Winnick, J. *J. Electrochem. Soc.* **1998**, *145*, 1449.

(15) Xu, Y.; Schoonen, M. A. *Amer. Mineralogist* **2000**, *85*, 543.

(16) Mrowec, S.; Danielewski, M.; Wojtowicz, A. *J. Mater. Sci.* **1998**, *33*, 2617.

(17) Seim, H.; Fjellvag, H.; Gronvold, F.; Stolen, S. *J. Solid State Chem.* **1996**, *121*, 400.

(18) Nava, D.; Gonzalez, I. *Electrochem. Acta* **2006**, *51*, 5295.

(19) Lefebvre, M. C. Establishing the Link Between Multistep Electrochemical Reactio Mechanisms and Experimental Tafel Slopes. In *Modern Aspects of Electrochemistryq*; White, R. E., Ed.; Plenum Publishers: New York, 1999; Vol. 32; pp 249.

(20) Holtappels, P.; Haart, L. d.; Stimming, U. *J. Electrochem. Soc.* **1999**, *146*, 1620.

(21) Holtappels, P.; Vinke, I.; Haart, L. d.; Stimming, U. *J. Electrochem. Soc.* **1999**, *146*, 2976.

6. Anodes for Direct Oxidation of Methane Containing H_2S

Abstract

Single cell solid oxide fuel cells using Ni-YSZ and Co-YSZ anodes were tested in H_2, CH_4, and H_2S/CH_4 fuel mixtures. Their performance was found to quickly degrade in dry CH_4 due to carbon deposition and lifting of the anode from the electrolyte. In contrast, hydrogen or methane containing H_2S showed an increase in exchange current densities when compared to H_2,M/YSZ/LSM,air systems (M=Ni or Co), despite having less optimal anode microstructure. Conversion from metal to metal-sulfide in the presence of H_2S produced large, dense metal-sulfide particles surrounded by YSZ, thus decreasing the TPB. Furthermore, CoS-based anodes showed phase segregation and densification towards the electrolyte. Despite this, long term testing at 0.5V of the H_2S/CH_4,CoS-YSZ/YSZ/LSM,air system showed no signs of degradation over a 6 day period. Only after removal of H_2S from the H_2S/CH_4 stream did the CoS- anode reduce back to Co, signifying H_2S is required to maintain the metal-sulfide active anode.

6.1 Introduction

Solid oxide fuel cells (SOFC) are the most flexible fuel cells with respect to fuel selection. They have great potential for generating power from many sources including, hydrogen, natural gas, syngas and biogas. Utilizing natural gas as fuel has garnered much attention recently due to its natural abundance, ease of transport and accessibility.

Numerous efforts to sustain direct utilization of hydrocarbons in SOFCs have shown that conventional Ni-YSZ anodes are prone to uncontrolled carbon deposition during operation with dry hydrocarbon feeds since catalytic dissociative adsorption of CH_4 on the anode surface (Equation 6.2) competes with the desired electrochemical reaction (Equation 6.1).

$$CH_4 + 4O^{2-} \rightleftarrows CO_2 + 2H_2O + 8e^- \qquad (6.1)$$

$$CH_4 \rightleftarrows C_{gr} + 2H_2 \qquad (6.2)$$

Some researchers have attempted to circumvent carbon deposition by using alternative operating conditions, where steam is added to the fuel stream[1,2]. The anode provides catalytic sites for reforming CH_4, converting methane to H_2 and CO. However, internal steam reforming of methane is endothermic and can cause a significant cooling effect with the development of large temperature gradients, while the high H_2O/CH_4 ratio required to avoid

coke formation results in a severe decrease of fuel cell open-circuit potential, thereby reducing its efficiency. Other modifications to operating conditions have focused on introducing oxygen through the electrolyte by increasing the electrochemical load.[3]

Alternative work has focused on preparing anode materials, which may be used directly in a dry hydrocarbon environment without changing the operating conditions. To replace Ni-based anodes, these materials should be easy to maintain, easy to process and exhibit similar catalytic properties to those of Ni without suffering similar carbon formation. Emphasis has been placed on Cu-based anode materials since they are inexpensive and have been shown to be relatively inert to the formation of C-C bonds. However, the melting temperature of copper and its oxides are low compared to that of Ni and its oxide. Therefore, copper anodes cannot be produced as easily as nickel anodes and require pre-sintering of the electrolytic component with pore formers prior to Cu impregnation.[4] Additives such as Mo, Pd, Co, Sm_2O_3 and CeO_2 to Ni- and Cu-based anodes have also been examined and show positive results as they inhibit the formation of adsorbed graphitic layers.[5-8] However, the problems of cell processing and carbon formation are yet to be fully resolved.

Natural gas also contains sulfur compounds which are known to degrade the anodes. Ni-YSZ based systems have shown little tolerance to fuels containing low (ppm) H_2S concentrations, where sulfur tolerance decreased as a function of lower operating temperatures and higher H_2S concentrations.[9,10] Due to the incompatibility of Ni-YSZ based systems with sulfur, emphasis has recently been placed on improving tolerance of SOFC anodes by changing the composition of the anode.[9,11-13] Although these materials showed promise in H_2/H_2S fuel mixtures at low concentrations, little evidence on their long term performance at high sulfur concentrations in methane is available.

In this chapter Ni-YSZ and Co-YSZ anodes were subjected to H_2, CH_4, and H_2S/CH_4 fuel over extended periods of time. The primary objective of this work was to determine the feasibility of employing Ni-YSZ and Co-YSZ cermets as anode materials in multiple fuel environments. Electrochemical measurements were used to determine performance and lifetime of the anodes in each fuel stream. Post-run analysis with SEM, XRD and XPS was used to determine the nature of the active species and any morphological changes that occurred during SOFC operation.

6.2 Experimental

The fuel cell was prepared by mixing Triton X-100 (Research Chemical Ltd)/water and 1g of anode powder. The YSZ supported metal (M-YSZ) (55wt%) anode materials were prepared via co-precipitation by dissolving appropriate amounts of $ZrCl_4$, Y_2O_3 (dissolved in 10ml of 37wt% HCl) and $NiCl_2 \cdot 6H_2O$ or $CoCl_2 \cdot 6H_2O$ (Aldrich) in 165 ml of distilled water. To ensure YSZ phase purity and stability, the anode materials were synthesized with 21 mol% YSZ.[14] Precipitation was achieved through introduction of 2*M* NaOH (Aldrich) to pH 13. Following precipitation, the product was filtered, washed, dried at 120°C and calcined at 750°C for 2h. Resulting powder composition and characterization has been described previously.[15,16]

0.15g of the slurry was coated onto an YSZ green-disk (Tosoh) and heated to 1400°C for 4h in air. A 70wt% LSM/30wt%YSZ mixture (LSM, Nextech Materials; YSZ, Tosoh) was used as the cathode and reference electrode material. The cathode was prepared by coating 0.15g of LSM/YSZ powder symmetrically opposing the sintered anode, while the reference electrode was approximately 4mm to the side of the cathode.[17] Upon sintering, the YSZ electrolyte was 0.5mm thick with electrode areas of $0.4cm^2$ for the anode and cathode and $0.2cm^2$ for the reference electrode. 10wt%Rh/Pt mesh current collectors were embedded into the electrodes during sintering to minimize any losses due to contact resistance.[18]

Hydrogen, methane and hydrogen sulfide flows were regulated by mass flow controllers (MKS) to a total flow of 50sccm. Temperature was controlled via an Omron E5CN controller and measured with a K-type thermocouple placed outside a shielded quartz tube. The Chromel®-shielded quartz tube was placed in the furnace around the fuel cell, connected to ground and used as a precaution to reduce background noise introduced by the furnace.

All electrochemical measurements were performed at 850°C with the following fuels: pure hydrogen, pure methane or 0.3-10%v/vH_2S/CH_4. Pyrex® was used to seal the edge of the alumina tube to the YSZ surface. After initial preparation, mounting and reduction of the cell, a minimum OCV of 1.0V was required to continue electrochemical measurements. All such measurements were taken using a VoltaLab 40 (Radiometer Analytical), where impedance measurements were taken over a frequency range of 100kHz-250mHz at OCV. Equivalent circuit modeling of impedance data was performed with Zview software. DC current-voltage measurements were conducted using a potential scan rate of 2mV/s. Exhaust gas was monitored using an AccuQuad residual gas analyzer. Pre- and post-run analysis of

the fuel cell anode was accomplished by X-ray diffraction (XRD) (Phillips PW1830) using CuKα radiation with a wavelength of 1.54Å. The scan range was measured from $2\Theta = 20°$ to 90° at a rate of $0.02° s^{-1}$. Crystalline phases were assigned using the Powder Diffraction File (PDF) database (ICCD, 2001, Dataset 1-51). NanoLab7 SEM with Kevex EDS was used to assess particle size and morphology as well as elemental compositions.

X-ray photoelectron spectroscopy (XPS) experiments were performed in a SPECS Gmbh. multi-technique ultra-high vacuum chamber with a base pressure of 10^{-10} mbar. A non-monochromated source producing aluminum Kα X-rays (1486.7 eV) was used and survey spectra in the binding energy range 1200-1 eV were taken (0.8 sec. dwell, 0.3eV step). The electron pass energy was set to 10 eV. Higher resolution scans of selected peaks were performed for quantification and comparison purposes (8 sec. dwell, 0.2 eV step), and were fit in Casa XPS analysis software using a mixed Gaussian-Lorentzian function after Shirley background subtraction. The Binding energy scale was calibrated to the advantageous carbon peak which was set to 284.8 eV.

6.3 Results and Discussion

6.3.1 Performance of Ni-YSZ and Co-YSZ anodes in CH_4

Prior to fuel cell operation, SEM images of the precursor anode/YSZ electrolyte cross-sections were taken and are exhibited in Figure 6.1.

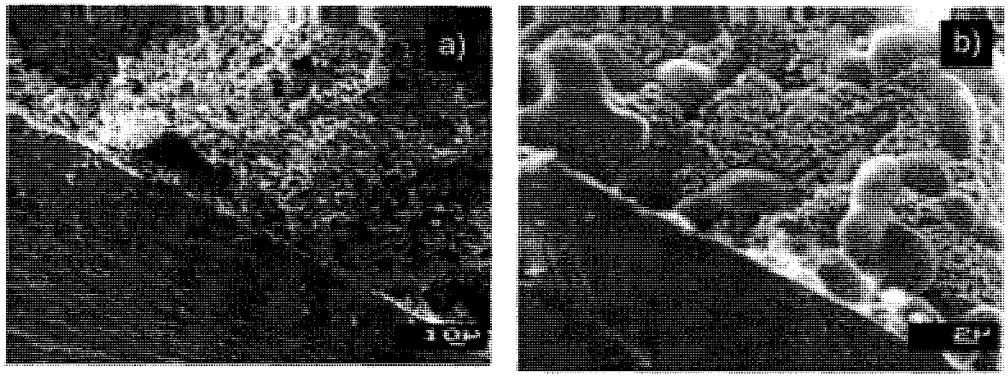

Figure 6.1 Cross-sections of YSZ and anode precursor powders after sintering on dense YSZ. a) NiO-YSZ; b) Co_3O_4-YSZ.

The NiO-YSZ anode in Figure 6.1.a shows porous microstructure and good contact between anode and electrolyte. The Co_3O_4-YSZ anode in Figure 6.1.b showed a substantially different morphology and was characterized by large YSZ particles surrounded by Co_3O_4. Contact between the Co_3O_4-YSZ and electrolyte was also satisfactory.

Figure 6.2 shows the ratio of exchange current densities obtained with CH_4 and H_2 fuels for Ni- and Co-YSZ anodes.

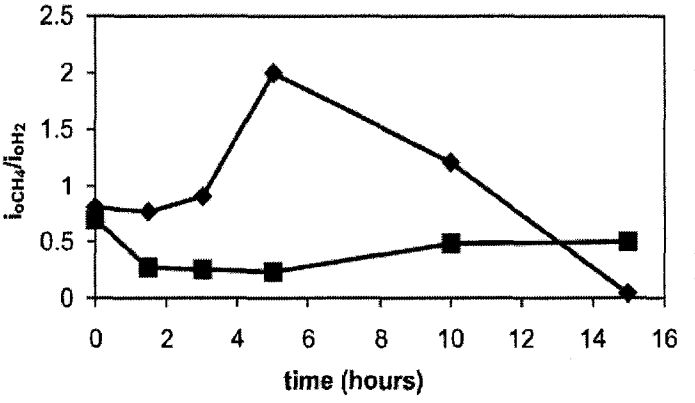

Figure 6.2 Changes in exchange current densities of Ni-YSZ and Co-YSZ anodes over time in CH_4. (♦) Ni-YSZ (■) Co-YSZ.

Ratios of exchange current densities between the fuel of interest and H_2 were used to account for deviations associated with irreproducibility between fuel cells. Therefore it is a measure of the increase/decrease in performance in a particular fuel with respect to H_2. Exchange current densities were obtained using the high field approximation of the generalized kinetic equation for a one-electron transfer process proposed by Erdey-Gruz and Volmer and Butler.[19-22]

$$\ln i = \ln i_o + b^{-1}\eta \text{ where } b^{-1} = \frac{\alpha_a F}{RT} \qquad (6.3)$$

By plotting ln$i$ vs η, one may obtain both the exchange current density for a particular reaction and the inverse Tafel slope. Exchange current densities were used to describe performance in each fuel. Upon operation with dry methane, the Ni-YSZ anode exhibited a slight increase in performance in the first five hours, but quickly began to degrade after 5 hours of operation (Figure 6.2). By the 15th hour the anode had fully degraded and showed no activity. Post-run analysis showed the anode had disintegrated and black powder found at the bottom of the fuel cell was collected for analysis. Unlike Ni-YSZ, Co-YSZ exhibited an $i_oCH_4/i_oH_2 < 1$ at all times with no signs of decreasing performance during 15 hours of testing.

However, post run analysis of this anode showed it had partially separated from the electrolyte due to the onset of carbon poisoning.

XRD analysis of the black powder found at the bottom of the Ni-YSZ fuel cell consisted of Ni (PDF# 04-0850), YSZ (PDF# 30-1468) and graphite (PDF# 26-1077). Post-run XRD of the Co-YSZ anode itself showed the presence of hexagonal Co (PDF# 05-0727), YSZ and small amounts of graphite.

Low resolution SEM/EDX of post-run anodes in Figure 6.3 revealed the morphology of the anodes after 15 hours in dry methane.

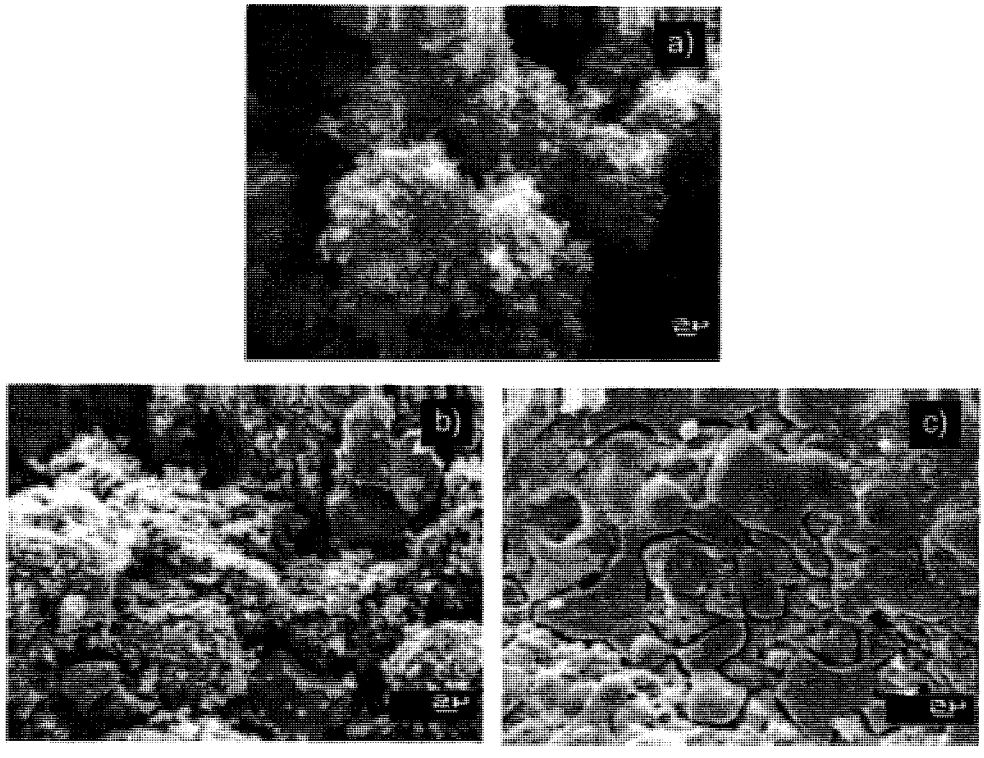

Figure 6.3 SEM images of top views of the anodes microstructure after operating at 850°C for 15hours in CH_4. a) Ni-YSZ; b) Co-YSZ and c) Co-YSZ in contact with the electrolyte.

It is clear that the Ni-YSZ anode had degraded producing the powder containing a significant amount of graphite with no visible signs of the original Ni or YSZ sintered bodies. Co-YSZ anodes resulted in a portion of the anode disengaged and another portion still attached to the electrolyte. Figure 6.3.b shows a section of the anode which was separated from the electrolyte. The large crystalline particles approximately 2-6μm in diameter were YSZ, while the smaller particles consisted of Co and graphite. Figure 6.3.c is the portion of the anode which did not disengage from the electrolyte and shows the sintered YSZ and Co

morphology as seen prior to fuel cell operation in methane, albeit with separation between the Co and YSZ bodies.

The tendency of metals to form carbon has been well studied particularly for catalytic applications.[23-26] Carbon formation involves deposition of a carbon source onto the metal surface, its dissolution into the bulk and its precipitation back out as a fiber at the surface of the metal particle. Therefore the metal phase can be physically lifted from the electrolyte by carbon. This lifting is noticeable in the Co-based anode where the Co species in Figure 6.3.c are separated from YSZ, eventually leading to disintegration of the anode from the YSZ component. Although the Co-based anode showed no signs of degradation during 15 hours of operation, SEM and XRD analysis suggested this fuel cell would eventually suffer full degeneration within hours.

6.3.2 Performance of Ni-YSZ and Co-YSZ anodes in H_2S/CH_4

When H_2S/CH_4 was used as fuel, a decrease in performance was initially observed. However, as with the H_2S/H_2 system, the performance quickly increased and exceeded that observed when H_2 was the fuel as evidenced by the large $i_oH_2S/CH_4/i_oH_2$ ratios (Figure 6.4).

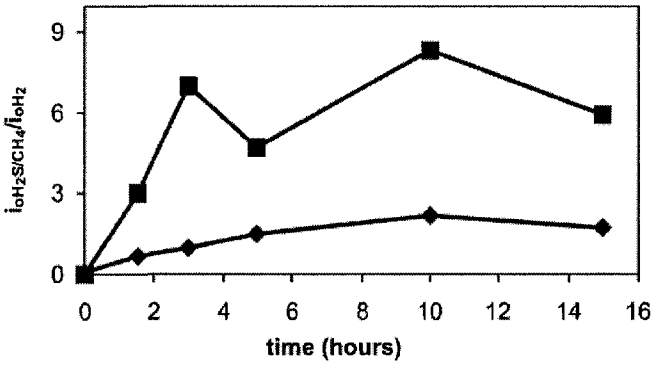

Figure 6.4 Changes in exchange current densities of Ni-YSZ and Co-YSZ anodes over time in 10%v/vH_2S/CH_4. (♦) Ni-YSZ (■) Co-YSZ.

Formation of NiS- and CoS- species was again deemed to be the cause of initial decrease in performance. Once all the metal converted to metal-sulfide a marked increase in performance was again observed. Both the NiS- and CoS- systems showed remarkable improvement in the oxidation of dry methane, producing exchange current densities which were ~1.5 ad ~6 times greater respectively than those obtained when dry hydrogen was the fuel. Neither fuel cell showed signs of degradation over a 15 hour period.

XRD analysis of post run anodes indicated addition of high levels of H_2S into the fuel stream resulted in anodes consisting of NiS- and CoS- species. More specifically, the Ni-YSZ anode consisted of Ni_7S_6 (PDF# 14-0364), $NiS_{1.03}$(PDF# 02-1273) and Ni_xS_6 (PDF# 51-0718), while the Co-YSZ anode was $CoS_{1.035}$(PDF# 25-1081). Again, the phases present at room temperature are not assumed to be the electrode present during fuel cell operation at high temperatures and are possibly $Co_{1-x}S$ and $Ni_{3+x}S_2 + Ni_{1-x}S$, as suggested previously.[27,28]

Post-run analysis of the fuel cell showed that unlike the H_2S/H_2 system, a silvery foil like substance was found near the anodes and along the edges of the tube. XRD of this substance indicated that it was amorphous and characterization via powder x-ray diffraction was not possible. SEM analysis of this substance was performed as shown in Figure 6.5.

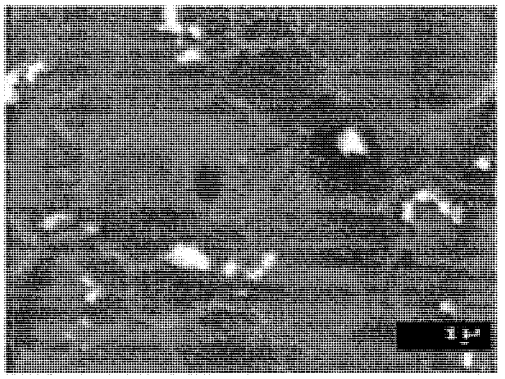

Figure 6.5 SEM image of the foil produced during H_2S/CH_4 fuel cell operation.

The foil consisted of flat plate like particles approximately 10μm in diameter. Two foil samples were studied by X-ray photoelectron spectroscopy, in the first sample the surface of the foil in contact with the alumina tube was analyzed (Figure 6.6.a). In the second the outside surface was considered.

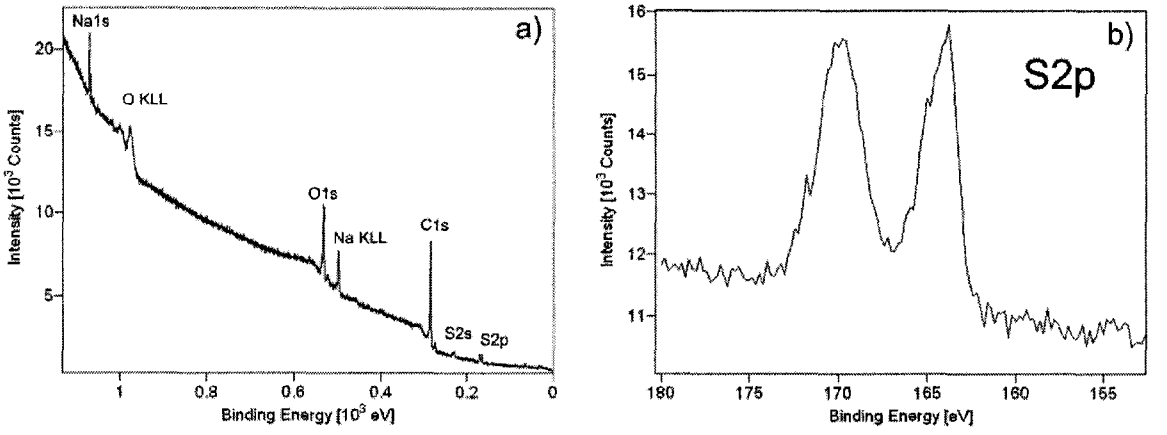

Figure 6.6 (a) XP-survey spectrum (1100-0 eV) of the amorphous carbon sample surface which was in contact with the alumina tube. (b) High resolution scan of the split sulfur 2p peaks.

In the first sample, the foil surface region was composed of carbon, oxygen, sulfur, and sodium in relative atomic concentrations of 66%, 24%, 6%, 4% respectively. The sodium was not seen in the second sample suggesting it was from the Pyrex ring or Alumina tube. The sulfur 2p peak (Figure 6.6.b) however, was seen in both samples, and it was found to be split, with one peak at a binding energy of 164 eV and the other at 169.8 eV. The former likely corresponding to elemental sulfur (164 eV) or a chemisorbed sulfide such as CS_2 (163.7eV)[29], and the latter consistent with an oxygen containing sulfur species such as a sulfone (~167-170 eV) or sulfate (~168-171 eV)[30]. The amorphous carbon foil itself likely grows in a manner similar to a chemical vapor deposition (CVD) type mechanism, in which precursor gases react or decompose at a substrate surface forming a film. These types of films are often grown by various types of CVD such as plasma enhanced CVD or hot filament CVD in which the precursors are altered in order increase growth rate. However these added techniques are not necessarily required and the high temperatures of the fuel cell may produce the same results. There is a large body of literature in which carbon films are formed by CVD using methane and hydrogen as precursor gases.[31-33] Typically temperature and precursor ratios control the film structure from amorphous to crystalline. XP-spectra of sulfur doped micro and nano-crystalline carbon films grown by Gupta *et al.* [33] using CH_4, H_2 and H_2S as precursors showed a split sulfur 2p peak similar to the one observed in the foil. By depth profiling it was found that the elemental sulfur was incorporated throughout the film while the oxygen containing sulfates or sulfones were absorbed only on the surface.

Analysis of exhaust gas by mass spectrometry indicated there was not a significant amount of SO_2 produced, yet there was CS_2 production according to the following reaction

$$CH_4 + 2H_2S \rightleftarrows CS_2 + 4H_2 \quad (6.4)$$

Other possible products such as CH_3SH and C_2H_5SH[34] were not observed in the mass spectrum.

OCV values obtained for these systems were 1.0V and 1.2V for the Ni-based and Co-based anodes respectively. The slight discrepancy between the OVC's of each anode was attributed to reproducibility of the seal between fuel cells. The introduction of CS_2 as an electrochemically active species renders determination of the fuel impossible since CS_2 may be oxidized in numerous ways. Table 6.1 lists the possible reactions of CS_2 with the theoretical cell potential at 850°C.

Table 6.1 Reversible potentials for possible CS_2 oxidation reactions at 850°C calculated from thermodynamic data.

Reaction #	Electrochemical Reaction	E^o at 850°C (V)
1	$CS_2 + 2O^{2-} \rightleftarrows CS + SO_2 + 4e^-$	-0.345
2	$CS_2 + 3O^{2-} \rightleftarrows COS + SO_2 + 6e^-$	0.835
3	$CS_2 + O^{2-} \rightleftarrows COS + \frac{1}{2} S_2 + 2e^-$	1.049
4	$CS_2 + 4O^{2-} \rightleftarrows CO_2 + SO_2 + 8e^-$	1.225
5	$CS_2 + 2O^{2-} \rightleftarrows CO_2 + S_2 + 4e^-$	0.991
6	$CS_2 + O^{2-} \rightleftarrows CO + S_2 + 4e^-$	0.510

Because of the small separation in potential, once Nernstian effects are taken into account, the electrochemically active species cannot be distinguished between H_2, CH_4 or CS_2. Despite mass spectrum data showing no significant signs of COS or SO_2 production, the possibility of the measured OCV resulting from electrochemical oxidation of a combination of H_2, CH_4 or CS_2 is not excluded.

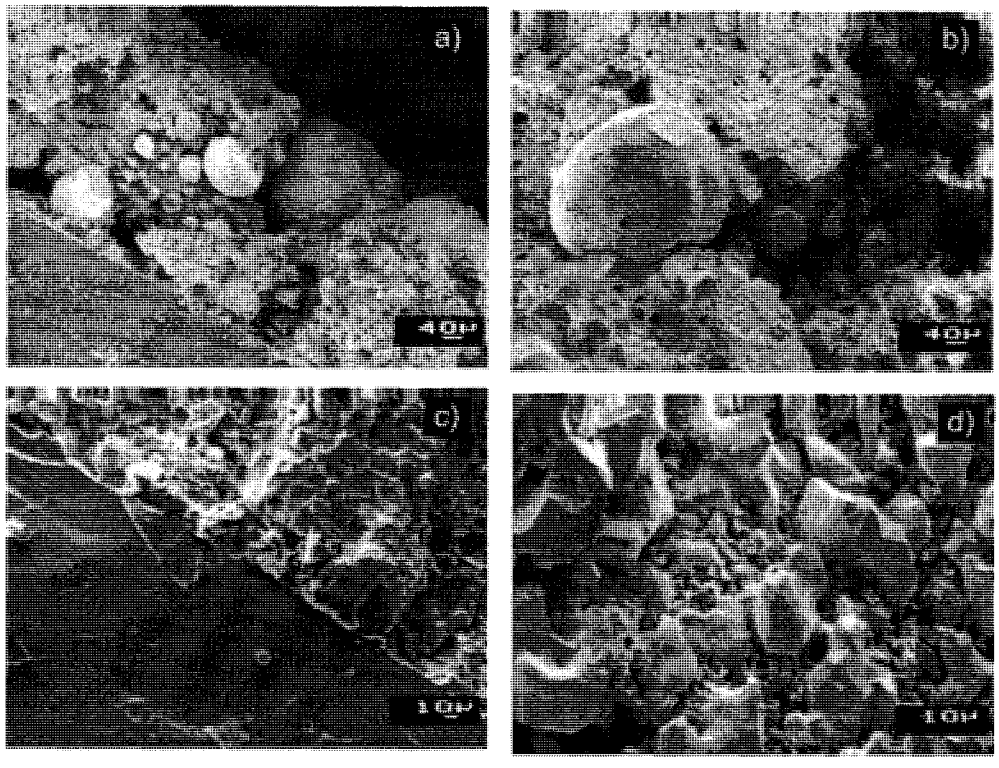

Figure 6.7 SEM images of Ni-YSZ and Co-YSZ anodes after operating at 850°C for 15 hours in H_2S/CH_4. a) Cross section of Ni-YSZ on dense YSZ; b) Top view of Ni-YSZ anode; c) Cross section of Co-YSZ on dense YSZ; d) Top view of Co-YSZ anode.

SEM/EDX post-run analysis of the anodes showed reasonable contact for both the Ni-based and Co-based anodes (Figure 6.7.a and 6.7.c). The Co-YSZ anode showed an extremely dense structure near the electrolyte consisting of CoS- and YSZ. Figure 6.7.d is the top view of the anode and shows large particles consisting of a CoS- phase surrounded by smaller YSZ particles. The large increase in activity of these systems with respect to H_2 demonstrates the exciting prospect of using metal-sulfides as anodes for oxidation of sulfur containing natural gas, particularly if one considers the agglomeration observed for the CoS-YSZ anode and consequent reduction of the TPB. Similar results are observed for NiS-YSZ

anodes where large particles of NiS- species dominated the anode microstructure (Figure 6.7.a and 6.7.b).

To assess the feasibility of using CoS-YSZ as a potential fuel cell anode, the cell was left to run for a total of 6 days at 850°C in 10%v/v H_2S/CH_4. Figure 6.8 shows the H_2S/CH_4,Co-SYSZ/YSZ/LSM,air system ran continuously at 0.5V without any noticeable degradation. In fact, the output consistently increased with time.

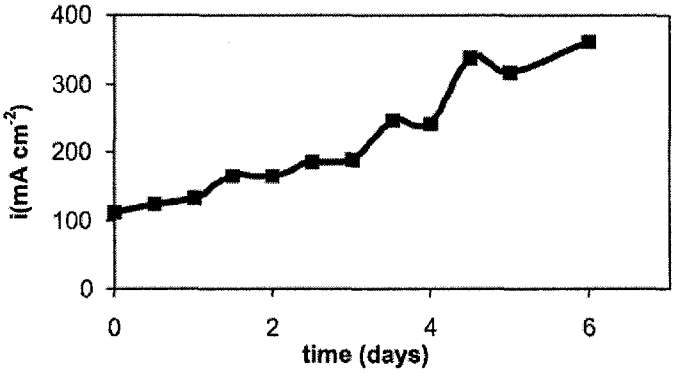

Figure 6.8 Current densities measure over a 6 day period in 10%v/v H_2S/CH_4 on Co-YSZ at 0.5V and 850°C.

However, when H_2S was removed from the system, the anode quickly degraded due to carbon deposition (Figure 6.9).

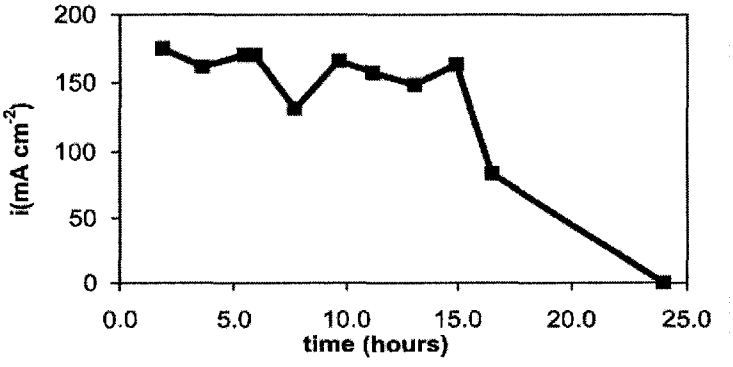

Figure 6.9 Current densities measured over a 2 day period in CH_4 on CoS-YSZ at 850°C.

Post-run XRD analysis showed this anode consisted of Co (PDF# 15-0806), YSZ (PDF# 30-1468) and graphite (PDF# 26-1077). The CoS- species maintained in the fuel cell when H_2S was present was quickly reduced back to elemental Co through sulfidation of CH_4 or H_2 with adsorbed –S. Removal of sulfur from the feed changed the CoS- species to cubic Co

and, not hexagonal Co, which was the species found when CH_4 was the fuel. Irregardless of crystal structure, carbon formation seems inevitable on Co.

From previous results it became evident that H_2S was required in the feed to maintain fuel cell performance. To determine the amount of H_2S needed to maintain anode performance the CoS- anode was synthesized in situ by adding a 10%v/v H_2S/H_2 mixture. The fuel was then changed to H_2S/CH_4 and the amount of H_2S was varied in the stream. Figure 6.10 is a plot of current density at 0.5V as a function of time for CoS-YSZ in CH_4 with decreasing amounts of H_2S.

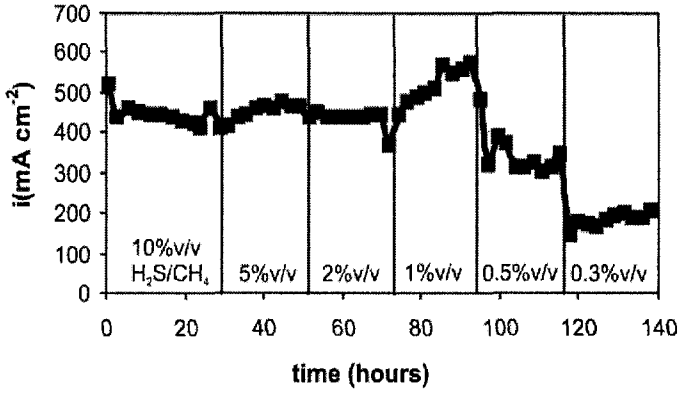

Figure 6.10 Current density as a function of time at 850°C at 0.5V with changing H_2S content.

The anode showed stable performance at each concentration for 24 hours and ran for a total of 140 hours. Cell performance was stable for concentrations of H_2S>1%v/v. Below 1%v/v, activity decreased as a function of H_2S partial pressure. The loss in performance may be a result of decreased H_2 production, as per reaction 6.4, and/or a change in cobalt sulfide stoichiometry to another sulfide species, where $Co_{1-x}S$ may convert to Co, Co_4S_3 or Co_9S_8 at low H_2S partial pressures.[27]

6.4 Conclusion

Degradation of the Ni- and Co-based anodes occurred quickly in dry methane. Co-based anodes showed an increase in carbon deposition resistance over Ni-YSZ; however, XRD and SEM analysis of the used Co- anodes showed a significant amount of carbon deposition after 15hours.

The use of metal sulfides, specifically NiS- and CoS-YSZ anodes were active over long periods of time for methane and hydrogen fuels containing H_2S. Electrochemical evaluation

of the anode performance via linear voltammetry showed an initial decrease in SOFC performance when H_2S was added to the fuel stream, but after approximately 3 hours, when all of the metal was converted to metal-sulfide, the performance recovered and greatly surpassed the initial values. The superior performance suggests metal-sulfides are viable anode materials for carbon, sulfur resistant SOFC systems. H_2S/CH_4,CoS-YSZ/YSZ/LSM,air systems systematically exhibited significantly larger exchange current densities over H_2,Co-YSZ/YSZ/LSM,air fuel cells. NiS-YSZ also showed a marginal increase in exchange current densities. CoS- based anodes were able to operate in H_2S/CH_4 for up to 6 days without degradation or any visible signs of carbon deposition. The reaction between CH_4 and H_2S resulted in CS_2 production, where any of these gases were possible fuels and could not be distinguished. Carbon deposition quickly ensued when H_2S was removed from the fuel stream and CoS- reduced back to elemental Co.

The addition of H_2S into pure fuel streams enhanced SOFC performance by converting the anodes from pure metal to metal sulfides, suggesting metal-sulfides (particularly CoS- due to its higher melting temperature), are appropriate and interesting anode materials for SOFC's with fuels containing sulfur species.

References

(1) Liu, J.; Barnett, S. A. *Solid State Ionics* **2003**, *158*, 11.

(2) Weber, A.; Sauer, B.; Muller, A. C.; Herbstritt, D.; Ivers-Tiffee, E. *Solid State Ionics* **2002**, *152-153*, 543.

(3) Koh, J.-H.; Yoo, Y.-S.; Park, J.-W.; Lim, H. C. *Solid State Ionics* **2002**, *149*, 157.

(4) Gorte, R. J.; Park, S.; Vohs, J. M.; Wang, C. *Adv. Mater.* **2000**, *12*, 1465.

(5) Triantafyllopoulos, N. C.; Neophytides, S. G. *J. Catal.* **2003**, *217*, 324.

(6) Zhan, Z.; Lin, Y.; Barnett, S. "Anode Catalyst Layers for direct hydrocarbon and internal reforming SOFC's"; Solid Oxide Fuel Cells IX, 2005, Quebec City, Quebec.

(7) Nabae, Y.; Yamanaka, I.; Takenaka, S.; Hatano, M.; Otsuka, K. "Synergy of Pd and Ni Catalysts for direct oxidation of methane over lanthanum chromite based anodes"; Solid Oxide Fuel Cells IX, 2005, Quebec City, Quebec.

(8) Ahm, K.; Lee, S.; Vohs, J.; Gorte, R. "Novel Bimetallic anodes for direct utilization of hydrocarbon fuels"; Proceedings of the Ninth International Symposium on Solid Oxide Fuel Cells, 2005, Quebec City, Quebec.

(9) Sasaki, K.; Susuki, K.; Iyoshi, A.; Uchimura, M.; Imamura, N.; Kusaba, H.; Teraoka, Y.; Fuchino, H.; Tsujimoto, K.; Uchida, Y.; Jingo, N. "Sulfur Tolerance of Solid Oxide Fuel Cells"; International Symposium of Solid Oxide Fuel Cells IX (SOFC-IX), 2005, Quebec City, Quebec.

(10) Matsuzaki, Y.; Yasuda, I. *Solid State Ionics* **2000**, *132*, 261.

(11) He, H.; Gorte, R. J.; Vohs, J. M. *Electrochem. Solid State Lett.* **2005**, *8*, A279.

(12) Huang, Y. H.; Dass, R. I.; Xing, Z.-L.; Goodenough, J. B. *Science* **2006**, *312*, 254.

(13) Mukundan, R.; Brosha, E. L.; Garzon, R. H. *Electrochem. Solid State Lett.* **2004**, *7*, A5.

(14) Grgicak, C. M.; Giorgi, J. B. "YSZ Phase Purity and Stability in Chemically Prepared SOFC anodes"; Proceedings of the Ninth International Symposium on Solid Oxide Fuel Cells, 2005, Quebec City, Quebec.

(15) Grgicak, C. M.; Green, R. G.; Du, W.-F.; Giorgi, J. B. *J. Am. Ceram. Soc.* **2005**, *88*, 3081.

(16) Grgicak, C. M.; Green, R. G.; Giorgi, J. B. *J. Mater. Chem.* **2006**, *16*, 885.

(17) Krishnan, V. V.; McIntosh, S.; Gorte, R. J.; Vohs, J. M. *Solid State Ionics* **2004**, *166*, 191.

(18) Jiang, S.; Love, J.; Apateanu, L. *Solid State Ionics* **2003**, *160*, 15.

(19) Butler, J. *Trans. Faraday Soc.* **1923**, *19*, 729.

(20) Butler, J. *Trans. Faraday Soc.* **1932**, *28*, 379.

(21) Erdey-Gruz, T.; Volmer, M. *Z. Phys. Chem. A.* **1930**, *150*, 203.

(22) Erdey-Gruz, T.; Wick, H. *Z. Phys. Chem. A.* **1932**, *162*, 53.

(23) Keep, C.; Baker, R.; France, J. *J. Catal.* **1977**, *47*, 232.

(24) Baker, R.; Harris, P.; Terry, S. *Nature* **1975**, *253*, 37.

(25) Baker, R.; Harris, P.; Henderson, J.; Thomas, R. *Carbon* **1975**, *13*, 17.

(26) Baker, R.; Barber, M.; Harris, P.; Feates, F.; Waite, R. *J. Catal.* **1972**, *1972*, 51.

(27) Mrowec, S.; Danielewski, M.; Wojtowicz, A. *J. Mater. Sci.* **1998**, *33*, 2617.

(28) Seim, H.; Fjellvag, H.; Gronvold, F.; Stolen, S. *J. Solid State Chem.* **1996**, *121*, 400.

(29) Lindberg B.J., H. K., Johansson G., Gelius U., Fahlmann A., Nordling C., Siegbahn K. *Phys. Scripta 1* **1970**, *286*.

(30) Moulder J.F., S. W. F., Sobol P.E., Bomben K.D. *Handbook Of X-Ray Photoelectron Spectroscopy*; Physical Electronics, Inc., 1995.

(31) Fantoni, R.; Giorgi, M.; Moliterni, A. G. G.; Berden, W. C. M.; Lazic, V.; Martini, O.; Mattiot, F. P. *J. Mater. Res.* **1992**, *7*, 1204.

(32) Feng, Z.; Komvopoulos, K. *J. Appl. Phys.* **1995**, *78*, 2720.

(33) Gupta, S.; Weiner, B. R.; Morell, G. *J. Mater. Res.* **2003**, *18*, 363.

(34) Raulin, F.; Toupance, G. *Orig. Life* **1975**, *6*, 91.

7. $Ni_{1-x}Co_x$-YSZ and $Ni_{1-x}Cu_x$-YSZ Cermet Anodes

Abstract

NiCu- and NiCo- bimetallic YSZ anodes were synthesized via co-precipitation of their respective chlorides resulting in $Ni_{1-x}Co_x$-YSZ and $Ni_{1-x}Cu_x$-YSZ species. Single cell solid oxide fuel cells of these bimetallic anodes were tested in H_2, CH_4, and H_2S/CH_4 fuel mixtures. Their performance was found to quickly degrade in dry CH_4 due to carbon deposition and lifting of the anode from the electrolyte. Additions of Cu^{2+} into the NiO lattice resulted in large metal particle sizes and decreased SOFC performance. Addition of Co into the NiO lattice to form $Ni_{0.91}Co_{0.09}O$-YSZ anode precursor produced a cermet with a large BET surface area and active metal surface area, thus increasing the rate of hydrogen oxidation for this sample. However, when H_2S/CH_4 was used, sulfidated $Ni_{0.65}Co_{0.35}$YSZ showed superior activity, even surpassing the H_2 systems, thereby demonstrating the exciting prospect of using sulfidated $Ni_{1-x}Co_x$-YSZ as SOFC anodes in sulfur containing methane streams.

7.1 Introduction

Alternative preparations of SOFC anodes include the addition of a second component in the metal phase of the cermet. Suitable changes in composition of Ni-YSZ may improve the anodes performance by reducing coarsening of metallic particles and improving oxidation resistance of the anodes. Previous studies on bimetallic anodes suggest improved hydrogen oxidation rates and carbon deposition resistance. Small additions of Fe (10%w/w) had a significant positive influence on SOFC power generating characteristics in humidified H_2 at 800°C, while Mn and Ag additions greatly decreased power densities due to enlarged *i*R losses at the anode side.[1] However, iron is easily oxidized at high overpotentials or high oxygen partial pressures and may therefore exhibit undesirable corrosive properties in these conditions.

As seen previously (Chapter 6), direct utilization of hydrocarbons on Ni-YSZ electrocatalysts is not possible since Ni is prone to uncontrolled graphite formation. Precious metal addition (1%w/w) to Ni-YSZ influenced carbon deposition rates and electrochemical activity in CH_4, with NiRu- and NiPt-YSZ showing increased activity and decreased C-C formation.[2] However, carbon deposition was not entirely avoided; suggesting studies on alternative anodes are still required for direct utilization of CH_4. Replacing nickel with an electronic conductor that does not catalyze carbon formation, such as copper, has shown promise since it is relatively inert for the formation of C-C bonds and is inexpensive. However, copper's low melting temperature poses challenges in terms of anode stability and fuel cell fabrication.

In general the thermal stability, activity and sinteractivities of cermets are expected to increase with melting temperature of the metal. Nickel and copper have melting temperatures of 1728K and 1356K, respectively. The melting temperature of copper and its oxides are low compared to that of Ni and its oxide. Addition of significant amounts of copper to Ni-YSZ cermets showed a decrease in surface areas.[3,4] However, combining a small amount of copper to nickel cermet may result in anodes which exhibit desired properties of each individual metal. Therefore we hypothesized that mixtures of Ni and Cu would exhibit high stability due to the nickel component and slower carbon deposition rates due to the copper one.

Alternatively, cobalt exhibits a melting temperature of 1768K. Mixtures of Ni-Co would be expected to result in high electrochemical activities and thermal stabilities and would not require any unusual processing conditions. Additionally cobalt possesses a higher oxidation resistance than nickel and is not likely to exhibit corrosive properties at high overpotentials or high oxygen partial pressures.[5] It was recently shown that the addition of a small amount of cobalt to nickel cermets resulted in an increased electrochemical activation energy and pre-exponential factor, suggesting a larger metal dispersion.[1] This work was corroborated by *Ringuede et al*, where the surface area of these samples increased from $26m^2/g$ to $33\ m^2/g$ when moderate amounts of cobalt were added to Ni-YSZ synthesis.[3] Increased capacitance during H_2 oxidation were also observed with moderate cobalt fractions in Ni-YSZ suggesting microstructural changes such as extension of the TPB.[5]

This study was concerned with the stability and structural properties of NiCu- and NiCo-YSZ anodes in H_2, CH_4 and 10%v/v H_2S/CH_4. Emphasis was placed on electrochemical performance of each anode to evaluate performance in H_2 and stability in CH_4 and H_2S/CH_4 over time. Surface area, XRD and XRF were used to characterize the synthesized powders.

7.2 Experimental

7.2.1 Sample Preparation

YSZ supported metal (M-YSZ) (55 wt%) anode materials were prepared by dissolving appropriate amounts of $ZrCl_4$, Y_2O_3 (dissolved in 10ml of 37 wt% HCl) and $NiCl_2 \cdot 6H_2O$, $CuCl_2 \cdot 2H_2O$ or $CoCl_2 \cdot 6H_2O$ (Aldrich) in 165ml of distilled water. The precipitation was achieved through the introduction of sodium hydroxide (Aldrich) to pH 13. Following precipitation, the product was filtered, washed three times in 500ml of water and dried at 120°C overnight. A portion of dried product was then calcined at 750°C for 2h.

7.2.2 Characterization

The quantities of each metal were obtained using a Philips PW2400/00 X-ray fluorescence (XRF) instrument that was calibrated with a concentration gradient of $NiCl_2$, CuO or Co_3O_4 in a mixture of $ZrCl_4$ and Y_2O_3. Powder composition and crystallite sizes were determined by X-ray diffraction (XRD) (Phillips PW1830) using CuKα radiation with a wavelength 1.54 Å. The scan range was measured from $2\Theta = 20°$ to 90° at a rate of 0.02°/sec. Crystalline phases were assigned using the Powder Diffraction File (PDF) database (ICCD, 2001, Dataset 1-51). Lattice parameters were measured after theta calibration with LaB_6 internal standard (NIST) and peak refinement using Jade 6.1 software.

BET surface area and average particle sizes of the calcined powders were determined after reduction in flowing H_2 (99.9%, Praxair) at 600°C for 2h using a Quantachrome Autosorb 1-C instrument. Average metal particle size was measured by obtaining the active metal surface area via chemisorption experiments with H_2 as vector gas.

7.2.3 Electrochemical testing of synthesized anodes

The fuel cell was prepared by mixing Triton X-100 (Research Chemical Ltd)/water and 1g of anode powder. 0.15g of the slurry was coated onto an YSZ green-disk (Tosoh) and heated to 1400°C for 4h in air. A 70wt% LSM/30wt%YSZ mixture (LSM, Nextech Materials; YSZ, Tosoh) was used as the cathode and reference electrode material. The cathode was prepared by coating 0.15g of the LSM/YSZ powder symmetrically opposing the sintered anode, while the reference electrode was approximately 4mm to the side of the cathode. After sintering, the YSZ electrolyte was 0.5mm thick and the area of the electrodes were $0.4cm^2$ for the anode and cathode and $0.2cm^2$ for the reference electrode.

All electrochemical measurements were performed in pure hydrogen, CH_4, or 10%v/vH_2S/CH_4 mixture at 850°C. Hydrogen, methane and hydrogen sulfide flows were regulated by mass flow controllers (MKS) to a total flow of 50sccm. After initial preparation, mounting and reduction of the single cell, a minimum OCV of 1.0V was required to continue electrochemical measurements. All electrochemical measurements were taken using a VoltaLab 40 (Radiometer Analytical). Impedance measurements were taken over a frequency range of 100kHz-250mHz at OCV. Equivalent circuit modeling of the impedance data was performed with Zview software. DC current-voltage measurements were conducted using a potential scan rate of 2mV/s. Post-run analysis of the fuel cell anodes was accomplished by X-ray diffraction (XRD) (Phillips PW1830) using CuKα radiation with a wavelength of 1.54Å. The scan range was $2\Theta = 20°$ to 90° at a rate of 0.02°

s^{-1}. Crystalline phases were assigned using the Powder Diffraction File (PDF) database (ICCD, 2001, Dataset 1-51). NanoLab7 SEM with Kevex EDS was used for elemental analysis.

7.3 Results and discussion

7.3.1 Characterization of bimetallic SOFC anodes

Co-precipitation of $NiCl_2 \cdot 6H_2O$, Y_2O_3 (dissolved in HCl) and $ZrCl_2$ resulted in a two phase mixture of NiO and YSZ, with lattice parameters of 4.1761(0.0003) and 5.157(0.001) respectively as measured by XRD. Addition of small amounts of $CuCl_2 \cdot 2H_2O$ to the precipitation process also resulted in two phase systems consisting of cubic NiO and YSZ phases without an independent copper phase. Figure 7.1 shows the variation of the cubic lattice parameters of NiO with respect to copper and cobalt concentration.

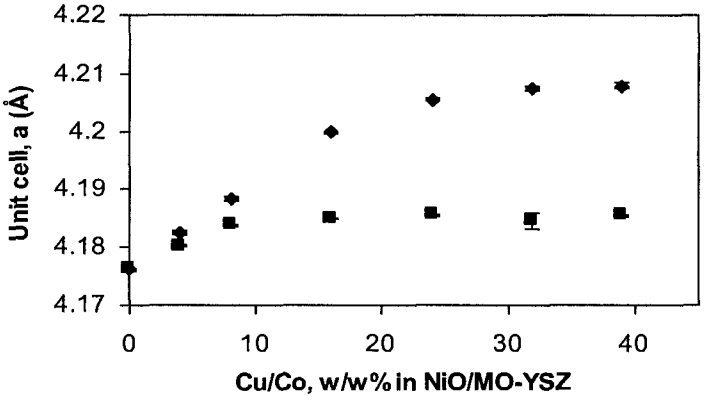

Figure 7.1 Variation in cubic unit cell parameters of NiO in NiO/MO-YSZ samples with increase in (■) copper and (♦) cobalt content.

Variation of the NiO lattice parameter in the calcined sample was linear with copper content up to 8w/w% (total metal content of 55w/w%). Once a significant amount of copper was added to the precipitation, the lattice parameters of NiO ceased to increase and a separate monoclinic CuO phase was observed. YSZ lattice parameters remained constant (5.162(0.003)) despite increasing Cu^{2+} concentrations. This type of cell-parameter variation is typical of systems in which substitution occurs. The observed variations of lattice parameters at low copper concentrations were mainly due to the different ionic radii $R_{Ni^{2+}}$=0.69Å and $R_{Cu^{2+}}$=0.72Å.[6] The same trend is observed for nickel/cobalt samples. Variation of the NiO lattice parameter was linear with cobalt content up to 24w/w%, suggesting solubility of Co^{2+} in the NiO lattice is greater than that of Cu^{2+}. Beyond this point

the lattice did not change and a separate Co_3O_4 phase was observed in the diffractrogram. YSZ lattice parameters remained constant in the NiO/CoO-YSZ systems (5.152(0.006)). Increases in NiO lattices were significantly larger for Co^{2+} than for Cu^{2+} and were attributed to the larger ionic radius of Co^{2+} ($R_{Co^{2+}}$=0.74Å).[6]

Table 7.1 shows the relative molar concentrations of metals in the two phase mixtures determined by XRF, assuming full isomorphic substitution of Cu^{2+} or Co^{2+} in NiO. Mixtures with the presence of a third phase; CuO or Co_3O_4 are not included. The BET surface area of NiO-YSZ was 21m^2/g with an average Ni particle size of 253nm. Substitution of Cu^{2+} within the oxide significantly reduced surface area and increased the particle size of the metal. Sinteractivity was also affected by the addition of copper.

Table 7.1 Powder characteristics of single and alloyed metal SOFC anode precursors.

Formula composition of metal oxide phase	BET Surface Area of reduced powder (m^2/g)	d_{Metal} (nm)	E_a (kJ/mol)
NiO	21	253	870+/-40
$Ni_{0.88}Cu_{0.12}O$	16	677	380+/-20
$Ni_{0.80}Cu_{0.20}O$	12	3576	470+/-50
CuO	12	1261	n/a
$Ni_{0.91}Co_{0.09}O$	44	118	360+/-40
$Ni_{0.82}Co_{0.18}O$	22	770	420+/-10
$Ni_{0.65}Co_{0.35}O$	19	2143	460+/-20
Co_3O_4	18	240	600+/-10

n/a- not applicable since CuO-YSZ melts at ~1100°C
Formula compositions - determined by XRF
BET surface area and d_{Metal} - obtained on reduced precursor powders calcined to 750°C
E_a - sinteractivity and is calculated as described in Section 2.2.7

Initially, the sinteractivity decreased from 870+/-40 to 380+/-20 kJ/mol for NiO-YSZ and $Ni_{0.88}Cu_{0.12}O$-YSZ respectively despite the larger metal particle size associated with this sample. Increasing the copper concentration increased both metal particle size and sinteractivity. The same trend was apparent for the NiCo-samples, where these samples resulted in smaller sinteractivities than those related to the single metal cermets. As the concentration of cobalt increased within the alloys both particle sizes and sinteractivities increased.

7.3.2 Anode Performance

7.3.2.1 Hydrogen

Determination of the exchange current density for each anode was obtained by using the high field approximation of the generalized kinetic equation for electron transfer processes proposed by Erdey-Gruz and Volmer and Butler.[7-10] iR_s corrections were made by utilizing the high frequency intercept of impedance measurements at OCV. The exchange current densities were used to evaluate performance differences between anodes. Figure 7.2 shows an example of iR_s corrected DC measurement for a NiCo-YSZ anode and the Tafel fits.

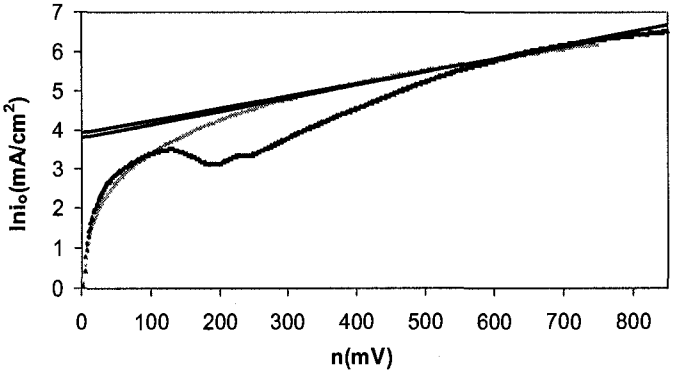

Figure 7.2 Example ln(current)-potential relations on sample $Ni_{0.91}Co_{0.09}$-YSZ used to determine exchange current densities for samples in (═)H_2 and (▬)10v/v%H_2S/CH_4 atmospheres.

Figure 7.3 shows the relationship between exchange current densities for $Ni_{1-x}Cu_x$- and $Ni_{1-x}Co_x$-YSZ anodes in hydrogen. Each type of anode was tested three times and the errors are represented in the figure. Although reproducibility between fuel cells was low (average relative standard deviation of 33%), significant differences between anode performances were still observed. Most notably, addition of copper to the nickel cermet resulted in a marked decrease in performance, particularly for $Ni_{0.80}Cu_{0.20}$-YSZ. The decrease in performance was related to the decreased TPB associated with the large metal particles obtained in this sample.[11]

Also, $Ni_{0.91}Co_{0.09}$-YSZ showed significant improvement in anode performance when compared to other $Ni_{1-x}Co_x$-YSZ samples. This was attributed to the large surface area and small metal particle size obtained when moderate amount of cobalt was introduced into the Ni bulk. This result is in agreement with *Ringuede et al.*, who showed an increase in

capacitance for moderate Co fractions, suggesting microstructural changes such as an extension of the metal/YSZ contact area.[5]

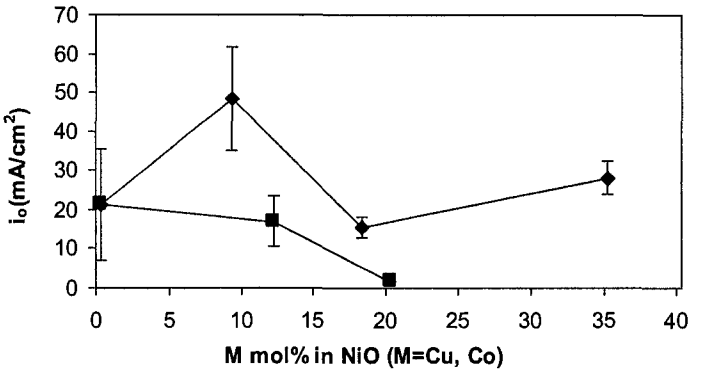

Figure 7.3 Exchange current densities for (■) $Ni_{1-x}Cu_x$-YSZ mixtures and (♦)$Ni_{1-x}Co_x$-YSZ mixtures.

7.3.2.2 CH_4 and H_2S/CH_4

Upon operation with dry methane, the Ni-YSZ anode exhibited a slight increase in performance in the first five hours, but quickly began to degrade after 5 hours of operation (Figure 6.2). By the 15th hour the anode had fully degraded and showed no activity. Post-run analysis showed the anode had disintegrated and black powder found at the bottom of the fuel cell was collected. Co-YSZ exhibited an i_oCH_4/i_oH_2 <1 (Figure 6.2) at all times with no signs of decreasing performance during 15 hours of testing. Post run analysis of this anode showed it was partially separated from the electrolyte due to the onset of carbon poisoning and was expected to suffer full degradation (Chapter 6). The $Ni_{1-x}Co_x$-YSZ samples exhibited the same carbon poisoning trend found for the Ni- and Co-YSZ anodes.

Carbon poisoning was prevalent for all $Ni_{1-x}Co_x$-YSZ anodes, with significant amounts of graphite found at the anode and at the bottom of the fuel cells, consistent with previous findings.[12] $Ni_{1-x}Cu_x$-YSZ anodes also showed significant carbon poisoning after 15 hours. Although copper is relatively inert for C-C bond formation, the presence of carbon corrosion in these anodes suggested a significant amount of copper was required to suppress carbon formation. That is, a separate copper phase is needed to successfully oxidize dry methane at an appreciable rate, with little to no graphite formation.[13,14]

When H_2S/CH_4 was used as fuel, a decrease in performance was initially observed. However, as for the H_2S/H_2,Ni- and Co-YSZ systems, the performance was rectified after ~3hours of operation (see Chapter 6). Formation of NiS- and CoS- species was deemed to be

the cause of initial decrease in performance. Once all the metal converted to metal-sulfide a marked increase in performance was observed. The same trend was observed for $Ni_{1-x}Co_xYSZ$ samples, where there was an initial decrease in performance followed by a significant increase after ~3 hours. Additionally, Figure 7.2 shows the anodic peaks in the 200mV in region are observed in H_2S/CH_4 as in the case of H_2S/H_2 atmospheres (see Chapter 5).

Table 7.2 shows the exchange current densities obtained after 15 hours of operation in H_2 and H_2S/CH_4. $Ni_{0.91}Co_{0.09}$-YSZ and $Ni_{0.82}Co_{0.18}$-YSZ showed sufficient activities in H_2S/CH_4 fuel streams resulting in exchange current densities which were approximately equivalent to those obtained when dry hydrogen was used, without any signs of degradation. $Ni_{0.65}Co_{0.35}$-YSZ exhibited a significant improvement in performance, where i_o increased from 24 mA/cm^2 in H_2 to 94mA/cm^2 in H_2S/CH_4, representing a 4-fold improvement. $Ni_{0.65}Co_{0.35}$-YSZ showed superior performance in H_2S/CH_4, surpassing all other anodes, even Ni-YSZ. XRD of the post run anodes showed significant amounts of NiS- species (Ni_3S_2 (PDF# 44-1418) and Ni_7S_6 (PDF# 14-0364)) and a minor unidentified phase. No identifiable CoS- or NiCoS- species as per the Powder Diffraction File (PDF) database (ICCD, 2001, Dataset 1-51) were found. SEM/EDX spot analysis indicated the-post run anodes consisted of Ni-Co-S and YSZ particles as opposed to NiS-, CoS- and YSZ particles. Therefore, sulfidation of the $Ni_{1-x}Co_x$ alloy does not promote phase separation between metal-sulfides, suggesting the active species during H_2S/CH_4 SOFC operation is a NiCoS- species. Additionally, as seen previously (Chapter 6), post-run analysis revealed the silvery foil like substance near the anodes and along the edges of the tube.

Table 7.2 Comparison of exchange current densities of each fuel cell run in H_2 and then in H_2S/CH_4.

Formula composition of metal oxide phase	i_o(mA/cm^2) in dry H_2	i_o(mA/cm^2) in 10%H_2S/CH_4	$i_oH_2/i_oH_2S/CH_4$
NiO	18	32	1.8
$Ni_{0.91}Co_{0.09}O$	51	44	0.9
$Ni_{0.82}Co_{0.18}O$	13	12	0.9
$Ni_{0.65}Co_{0.35}O$	24	94	3.9
Co_3O_4	4	25	6

OCV values obtained for all systems were 1.0+/-0.1V, again preventing the electrochemically active species to be distinguished between H_2, CH_4 or CS_2. However, increased activity of these systems with respect to H_2 demonstrated the exciting prospect of using bimetal-sulfides as anodes for oxidation of sulfur containing natural gas. This is particularly true for sulfidized $Ni_{0.65}Co_{0.35}$YSZ, which showed superior activity in 10v/v%H_2S/CH_4.

$Ni_{1-x}Cu_x$YSZ samples were tested in H_2S/CH_4 but continuously exhibited mechanical stress (i.e. electrolyte cracking) during the first few hours of operation, suggesting the expansion mismatch between anode and electrolyte was too great during sulfidation of $Ni_{1-x}Cu_x$.

7.4 Conclusion

Co-precipitation with NaOH to pH 13 was used to prepare various bimetallic SOFC anodes. The substitution of Cu^{2+} into the NiO lattice resulted in larger particle sizes, but smaller sinteractivities. Fuel cell performance was negatively affected by Cu^{2+} substitution, where the exchange current densities decreased with increasing copper content. Also, the addition of moderate amounts of copper did not inhibit graphite formation during dry methane oxidation.

The substitution of Co^{2+} into the NiO lattice resulted in powders with increased surface areas and decreased metal particle sizes, significantly affecting sinteractivities and SOFC performance. $Ni_{0.91}Co_{0.09}$-YSZ showed improvement in H_2 oxidation. This increase was attributed to the extension of the TPB. $Ni_{0.65}Co_{0.35}$-YSZ showed superior performance in H_2S/CH_4 streams suggesting sulfidated $Ni_{0.65}Co_{0.35}$YSZ is a superior electrocatalyst for sulfur and carbon containing fuels.

References

(1) Ishihara, T.; Yan, J.; Shinagawa, M.; Matsumoto, H. *Electrochem. Acta* **2006**, *52*, 1645.

(2) Takeguchi, T.; Kikuchi, R.; Yano, T.; Eguchi, K.; Murata, K. *Catal. Today* **2003**, *84*, 217.

(3) Ringuede, A.; Labrincha, J.; Frade, J. *Solid State Ionics* **2001**, *141-142*, 549.

(4) Grgicak, C. M.; Giorgi, J. B. "YSZ Phase Purity and Stability in Chemically Prepared SOFC anodes"; Proceedings of the Ninth International Symposium on Solid Oxide Fuel Cells, 2005, Quebec City, Quebec.

(5) Ringuede, A.; Bronine, D.; Frade, J. *Electrochem. Acta* **2002**, *48*, 437.

(6) Shannon, R. *Acta Crystallogr.* **1976**, *1976*, 751.

(7) Butler, J. *Trans. Faraday Soc.* **1923**, *19*, 729.

(8) Butler, J. *Trans. Faraday Soc.* **1932**, *28*, 379.

(9) Erdey-Gruz, T.; Volmer, M. *Z. Phys. Chem. A.* **1930**, *150*, 203.

(10) Erdey-Gruz, T.; Wick, H. *Z. Phys. Chem. A.* **1932**, *162*, 53.
(11) Grgicak, C. M.; Green, R. G.; Giorgi, J. B. *J. Mater. Chem.* **2006**, *16*, 885.
(12) Ahn, K.; Lee, S.; Vohs, J.; Gorte, R. "Novel Bimetallic anodes for direct utilization of hydrocarbon fuels"; Proceedings of the Ninth International Symposium on Solid Oxide Fuel Cells, 2005, Quebec City, Quebec.
(13) Gorte, R. J.; Park, S.; Vohs, J. M.; Wang, C. *Adv. Mater.* **2000**, *12*, 1465.
(14) Lu, Z.; Pei, L.; He, T.-m.; Huang, X.-q.; Liu, Z.-g.; Ji, Y.; Zhao, X.-h.; Su, W.-h. *J. Alloys. Comp.* **2002**, *334*, 299.

8. Conclusion

Abstract

Internal losses associated with SOFC anodes are particularly interesting area of research since the high operating temperatures allow utilization of multiple fuels. Therefore, losses must be minimized not only in hydrogen, but in methane and methane containing significant amounts of sulfides. This thesis deals with the synthesis of SOFC anodes and their performance and stability in multiple fuel environments (H_2, CH_4, H_2S/H_2 and H_2S/CH_4). Maximization of the TPB by optimizing synthesis conditions was explored in Chapter 3. Chapters 4 and 5 dealt with electrochemical characterization of porous Ni- and Co-YSZ anodes. Chapters 5, 6 and 7 examined the use of these anodes in fuel environments other than H_2. Chapter 8 is an overall evaluation of the results obtained throughout the course of this work. Recommendations for further research are also included.

8.1 Introduction

An introduction to fuel cells is provided. The history and types of fuel cells are discussed. The second part of the introduction describes efficiencies related to the SOFC. Emphasis is placed on describing voltage efficiency since it was the focus of this work.

8.2 Experimental/Analytical Considerations

Analytical assumptions and considerations are evaluated in this chapter. Generally, this chapter can be divided into two main branches: 1) Materials characterization and 2) Electrochemical characterization. Only XRF and XRD were used to assess compositions. Other techniques such as IR and UV-VIS were not used in this vain. XRD was particularly useful and was employed to obtain information on crystallite sizes, lattice parameters and phase composition. Physisorption and chemisorption analysis to attain specific surface areas and particle sizes were valuable, but the assumptions applied to model the isotherms were not helpful in providing information regarding morphology. As a result complimentary SEM analysis was necessary.

Validation of electrochemical testing was performed to assess the optimal fuel cell conditions to be used throughout the research. Concerns regarding the thickness of the electrolyte and the cross-talk between anode and cathode were addressed. Although the cross-talk between electrodes was deemed sufficiently low to continue electrochemical experiments, efforts aimed at minimizing this source of error are recommended. Some suggestions include using thicker electrolytes with a symmetric cell design, where a reference electrode is wrapped around the electrolyte and the electrodes are symmetrically opposed to one another.

8.3 Chemically Prepared SOFC Anodes

In this chapter an evaluation of chemically prepared Ni- Cu- and Co-YSZ anodes was performed. Since SOFC voltage efficiency is dependent on the TPB, finding alternative methods to synthesize anodes to achieve a larger boundary is justified. The Ni-YSZ anode had previously been synthesized via ammonia precipitation and was prepared as a reference material for co-precipitated Cu- and Co-YSZ anodes. However, during the course of this research it was clear that complexation of ammonia to the nickel was a concern and addition of NaOH to the precipitation was needed to obtain proper compositions. Despite similar XRD's, SEM and chemisorption analysis revealed a significant difference between the powders synthesized with NH_3 + NaOH and NaOH. Further examination into the sinteractivity revealed the powder properties and hence the sintered anode was greatly influenced by the mode of anode preparation. This was also the case for Cu- and Co-YSZ anodes.

Although Ni-YSZ anodes had previously been synthesized via co-precipitation by various groups,[1,2] a greater understanding between intermediate species, powder morphology, sinteractivities and SOFC anode performance was obtained through this work. It was determined that NaOH (pH 13) precipitation resulted in amorphous $\beta Ni(OH)_2$ intermediates (a fact that might be interesting in other electrochemical applications such as the Ni(II)/Ni(III) electrode reactions). Additionally, the crystallinity of the $\beta Ni(OH)_2$ can no longer be directly related to the pH of solution as previously suggested.[3]

The evaluation of co-precipitated Cu-YSZ and Co-YSZ anodes was also established. Co-precipitation of copper, yttrium and zirconium led to a variety of intermediates including copperhydroxychloride, copper hydroxide and copper oxide. The formation of copper hydroxide at high pH also suggested a complicated relationship between pH, complexing agent and precipitate.

By carefully evaluating the intermediate species obtained for all metals, a relationship between SOFC performance and intermediate species obtained through co-precipitation was established. That is, anodes that resulted in a crystalline intermediate during precipitation, exhibited smaller d_M/d_{YSZ} in the calcined powder and sintered anode, directly affecting SOFC anode resistances.

This work demonstrates the viability of using the co-precipitation method as a means to control particle sizes via the precipitation agent chosen. It emphasizes the need to control

metal yield during ammonia precipitation and includes new insights as to how the hydroxide intermediate formed during this has a direct affect on crystalline size, sintering and ultimately fuel cell performance.

8.4 Electrochemical Characterization of Ni- and Co-YSZ anodes in H_2 Fuel

Because of the conflicting AC impedance results prevalent in the literature, understanding the origin of each arc for this fuel cell set-up was important. Impedance responses with respect to overpotential and temperature were examined. The high-frequency arc associated with Process I varied with temperature, but not overpotential, suggesting a mass transport process. The mid-frequency arc (Process II) varied with temperature and overpotential. Activation energies of ~100kJ/mol suggested it was related to charge transfer processes rather than dissociative adsorption of H_2 or H_2O desorption. The low-frequency response decreased at higher overpotentials and was not present at overpotentials >200mV. Further analysis of this arc was not performed. However, since the third AC response is not always observed, further research into the nature of this process would be of great value. Responses to anode microstructure, overpotential, gas flow, temperature and anode composition would aid in determining the nature of Process III.

Evaluation of DC measurements using the Butler-Volmer relation suggested the rate determining step for hydrogen oxidation was the charge transfer step between O^{2-} and H_{ad}. This was experimentally determined by examining the relationship between the changes in Lefat slopes with temperature. The Tafel ranges were chosen based on three criteria (Chapter 4). The Lefat slope dependence was also corroborated by the $\ln i_\eta$ v T^{-1} curves obtained independently from impedance data, which exhibited a non-linear relationship between $\ln i_\eta$ and T^{-1} at high overpotentials. However, the curvature observed in the $\ln i$ vs η plots is not desired. Further experiments on ideal non-porous anodes at various temperatures, partial pressures and overpotentials are recommended to fortify the kinetics proposed in Chapter 4.

However, this chapter re-introduces the concept of the variability of the transfer coefficient with temperature in terms of the change in the entropy of activation with temperature. This variability would have a large impact on how transfer coefficients are determined and compared between laboratories at various conditions.

8.5 Electrochemical Characterization of Ni- and Co- YSZ anodes in H_2S/H_2 Fuel

This work concentrated on the performance aspects of Ni- and Co-YSZ anodes in fuels containing H_2S. Since H_2S is generally regarded as a poison, recent research has focused on preparing anodes that are resistant to sulfur poisoning. The work presented in this chapter introduced the concept of using metal sulfides, particularly CoS-, as viable SOFC materials for fuels containing H_2S. A 10%v/vH_2S/H_2 mixture was chosen to assess the poisoning rate. The anode performance initially degraded when H_2S was introduced, however, after significant exposure (~3hours) the performance of the anodes significantly increased. OCV results suggested the main electrochemical reaction was that of H_2 oxidation. Electrochemical characterization at various temperatures and overpotentials suggested impedance spectra are similar to spectra found for the H_2,Ni-YSZ system and may be interpreted in the same manner where the high-frequency arc was associated with transport and the mid-frequency arc with charge transfer. Relationships between the Lefat slope and T^{-1} indicated the rate determining step on NiS- anodes is the charge transfer between O^{2-} and H_{ad}, while the rate determining step of CoS- anodes could not be determined. The formation of the metal sulfides and the SOFC performance of these sulfides led to further experimentation.

8.6 Anodes for Direct Oxidation of Methane Containing H_2S

The result obtained when H_2S was added to the fuel led to further examinations of how these metal sulfide anodes would act in H_2S/CH_4 mixtures. Analysis of the anodes in this fuel mixture is important since natural gas (a possible SOFC fuel) contains H_2S and other sulfides. Long term performance of CoS- anodes in H_2S/CH_4 mixtures was assessed. The fuel cell ran on H_2S/CH_4 for 6 days without any signs of degradation. However, when H_2S was removed from the fuel stream, carbon deposition from CH_4 quickly ensued and disintegration of the anode was observed. It was determined that at least 1v/v%H_2S was required to maintain optimal fuel cell performance. The ability of CoS- anodes to work continuously in H_2S/CH_4 mixtures is interesting; however questions regarding which CoS- phases are the electrochemically active ones still remain. Experiments focusing on these identifications are recommended. Additionally, since the sulfide anodes were prepared in situ, no emphasis was placed on improving these anodes microstructure. It is expected that

the performance of CoS- anodes could be further enhanced by improving the anodes microstructure.

This chapter highlights the increased performance of Ni-YSZ and Co-YSZ anodes in H_2S environments. This contribution is particularly important. Studies at low partial pressure of H_2S suggest the poisoning of Ni or Co by H_2S may lead to a detrimental effect over long periods of time in high H_2S concentrations. This section dispels that assumption and introduces the idea of using sour gas as a viable fuel in NiS- and CoS-YSZ fuel cells.

8.7 $Ni_{1-x}Co_x$-YSZ and $Ni_{1-x}Cu_x$-YSZ Cermet Anodes

NiCu- and NiCo- bimetallic YSZ anodes were synthesized via co-precipitation of their respective chlorides resulting in $Ni_{1-x}Co_x$-YSZ and $Ni_{1-x}Cu_x$-YSZ species. Single cell solid oxide fuel cells of these bimetallic anodes were tested in H_2, CH_4, and H_2S/CH_4 fuel mixtures. Additions of Cu^{2+} into the NiO lattice resulted in large metal particle sizes and decreased SOFC performance. Addition of Co into the NiO lattice to form $Ni_{0.91}Co_{0.09}O$-YSZ anode precursor produced a cermet with a large BET surface area and active metal surface area, thus increasing the rate of hydrogen oxidation for this sample. However, when H_2S/CH_4 was used, sulfidated $Ni_{0.65}Co_{0.35}$YSZ showed superior activity, even surpassing the H_2 systems, demonstrating the exciting prospect of using sulfidated $Ni_{1-x}Co_x$-YSZ as SOFC anodes in sulfur containing methane streams.

References

(1) Marinsek, M.; Zupan, K.; Macek, J. *J. Power Sources* **2000**, *86*, 383.
(2) Li, S.; Guo, R.; Li, J.; Chen, Y.; Liu, W. *Ceram. Int.* **2003**, *29*, 883.
(3) Song, Q.; Tang, Z.; Guo, H.; Chan, S. *J. Power Sources* **2002**, *112*, 428.

Appendix A
Sample Calculation: Determination of $\Delta_r G_T^o$, $\Delta_r H_T^o$, OCV and theoretical efficiencies for a SOFC operating at 850°C

Variations of $\Delta_r H_T^o$ with temperature are expressed in terms of Kirchoff's Law

$$\Delta_r H_{T2}^o = \Delta_r H_{T1}^o + \int_{T1}^{T2} \Delta_r C_p dT$$

where

$$\Delta_r C_p = \sum_j \nu_j C_{p,m}(J)$$

Variations of $\Delta_r G_T^o$ is also dependant on temperature and is expressed in terms of the Gibbs Helmholz equation

$$\Delta_r G_{T2}^o = \frac{T2}{T1}\Delta_r G_{T1}^o + \Delta_r H_{T1}^o\left(\frac{T1-T2}{T1}\right)$$

Open circuit potentials are directly proportional to Gibbs free energy

$$\Delta_r G_T^o = -nFE_T^o$$

The theoretical efficiency is the ratio of the enthalpy and Gibbs energies

$$\varepsilon_T = \frac{\Delta_r G_T^o}{\Delta_r H_T^o}$$

Standard energies of formation and molar heat capacities[1]

	$\Delta_f H^o$ (kJ/mol)	$\Delta_f G^o$ (kJ/mol)	$C_{p,m}$ (J/K·mol)
CS_2	116.6	67.1	
O_2	0	0	29.4
CO_2	-393.5	-394.4	
SO_2	-296.8	-300.1	
CO	-110.5	-137.2	
S_2	128.6	79.7	
CH_4	-74.4	-50.3	
H_2O	-241.8	-228.6	33.6
H_2S	-20.6	-33.4	
CS	184	234	
COS	-142	-169.2	
H_2	0	0	28.8

$$H_{2(g)} + \tfrac{1}{2} O_{2(g)} \Leftrightarrow H_2O_{(g)}$$

$$\Delta_r H^o = \sum_j \nu_j \Delta_f H^o(J)$$

$$\Delta_r H^o_{298} = -241.8\,kJ/mol - 0\,kJ/mol - 0\,kJ/mol$$

$$\Delta_r H^o_{298} = -241.8\,kJ/mol$$

$$\Delta_r H^o_{T2} = \Delta_r H^o_{T1} + \int_{T1}^{T2} \Delta_r C_p dT$$

$$\Delta_r H^o_{1123} = -241.8\,kJ/mol + \left\{\left(33.6\,J/K\cdot mol - 28.8\,J/K\cdot mol - \tfrac{1}{2}\cdot 29.4\,J/K\cdot mol\right)(1123K - 298K)\right\}$$

$$\Delta_r H^o_{T2} = -250.2kJ/mol$$

$$\Delta_r G^o = \sum_j \nu_j \Delta_f G^o(J)$$

$$\Delta_r G^o_{298} = -228.6\,kJ/mol - 0\,kJ/mol - 0\,kJ/mol$$

$$\Delta_r G^o_{298} = -228.6\,kJ/mol$$

$$\Delta_r G^o_{T2} = \frac{T2}{T1}\Delta_r G^o_{T1} + \Delta_r H^o_{T1}\left(\frac{T1 - T2}{T1}\right)$$

$$\Delta_r G^o_{1123} = \frac{1123K}{298K}\left(-228.6\,kJ/mol\right) - 241.82\,kJ/mol\left(\frac{298K - 1123K}{298K}\right)$$

$$\Delta_r G^o_{1123} = -191.9\,kJ/mol$$

$$\varepsilon_T = \frac{\Delta_r G^o_T}{\Delta_r H^o_T}$$

$$\varepsilon_{1123} = \frac{-191.9\,kJ/mol}{-250.2\,kJ/mol}$$

$$\varepsilon_{T,1123} = 0.77$$

$$\Delta_r G^o_T = -nFE^o_T$$

$$-191.9\,kJ/mol = -2FE^o_{1123}$$

$$E^o_{1123} = 1.0V$$

(1) *CRC Handbook of Chemistry and Physics*, 74 ed.; Chemical Rubber Company Co: Boca Raton, 1993.

Appendix B
Transition State Theory and the Effects of Potential on Energy Barriers

Transition State Theory or Absolute Rate Theory assumes the reactions proceed through a well-defined transition state or activated complex. For a simple one-electron transfer at an interface,

$$O + e^- \Leftrightarrow R$$

the effects of a potential change on the standard free energies of reduction are represented by the following diagram

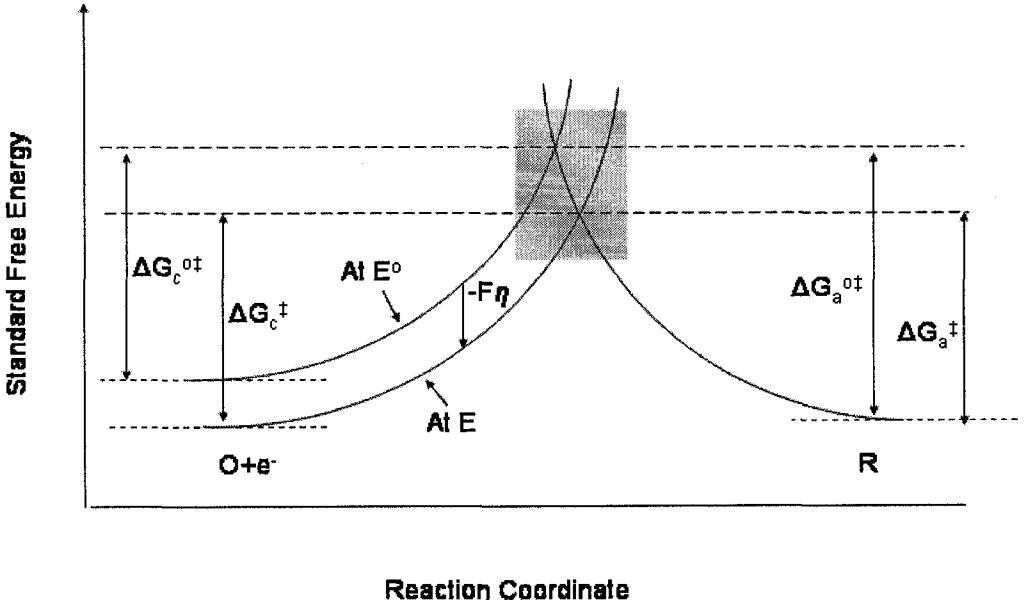

If the potential E^o is changed by a cathodic overpotential (η) to E, the relative energy of the electrons on the electrode change by $-F\eta$. Therefore, the $\Delta G_a^{\neq}$ is less than the $\Delta G_a^{o\neq}$ by a fraction of the total energy change (β, $0<\beta<1$).

$$\Delta G_a^{\neq} = \Delta G_a^{o\neq} - \beta F\eta$$

and $\Delta G_c^{\neq}$ is larger than $\Delta G_c^{o\neq}$ by 1-β.

$$\Delta G_c^{\neq} = \Delta G_c^{o\neq} + (1-\beta)F\eta$$

If we expand the gray section of the above diagram and assume the curves are locally linear, the $F\eta$ drop can be divided into anodic and cathodic portions.

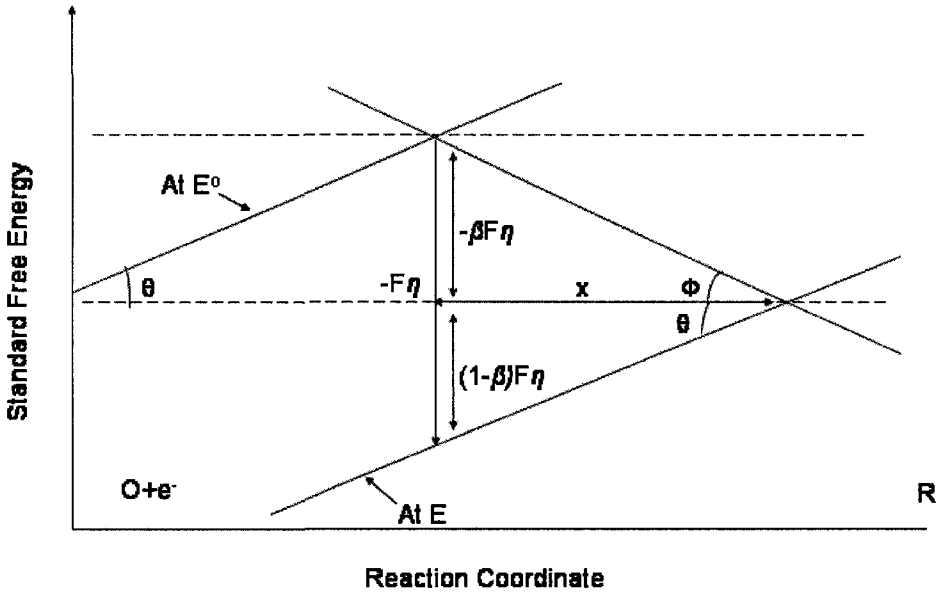

Therefore, β is a measure of the "symmetry" of the energy barrier and describes the portion of overvoltage that influences the cathodic versus anodic reactions. Further examination of the geometry reveals

$$\tan\theta = \frac{(1-\beta)F\eta}{x}$$

$$\tan\phi = \frac{\beta F\eta}{x}$$

$$\frac{\tan\theta}{1-\beta} = \frac{\tan\phi}{\beta}$$

$$\beta = \frac{\tan\phi}{\tan\theta - \tan\phi}$$

If the intersection is symmetrical $\theta = \phi$ and $\beta = 0.5$. Otherwise $0 \leq \beta \leq 0.5$ or $0.5 \leq \beta \leq 1.0$. In most one electron transfer cases, β has been found to lie between 0.3 and 0.7.[1]

(1) Bard, A. J.; Faulkner, L. R. *Electrochemical Methods: Fundamentals and Applications*, 2 ed.; John Wiley and Sons Inc.: Hoboken, 2001.

Appendix C
Characterization of Co-precipitated Bimetallic Precursors exhibiting undesirable SOFC characteristics

Characterization of anode precursor powders was performed prior to SOFC testing. Anode precursors that did not meet the three following criteria were not electrochemically tested.

1) Since our sintering temperature (for the majority of cells) during fuel cell fabrication was 1400°C, the melting temperatures (T_m) of the anode precursors needed to be larger than this value. High melting temperatures were also desired since they are indicative of anode stability.

2) The percentage yield of both metals needed to be within 80%, with a total metal content of 55 %w/w. The balance was oxygen and YSZ. Since co-precipitation was the main synthesis strategy and electric conductivity/anode performance is directly related to the amount of metal in the anode, a predictable composition was required.

3) The metals should not show any solid state reaction with Y or Zr. Since YSZ is the ionic conductor and its phase purity is required to maintain an optimal TPB, solid state reactions between the metals and YSZ were not ideal and these samples were not tested further

Generally, all bimetallics containing a large amount of CuO exhibited low melting temperatures and were not tested for this reason. Co-precipitation of Mo with Ni yielded powders with unsatisfactory Mo compositions. Additionally, NiMo- samples that yielded a $NiMoO_4$ phase could not be sintered. During the sintering experiments the pellets expanded in diameter and resulting in a powder (as opposed to a sintered body) at high temperatures. CuMo- and CoMo- samples did not result in predictable Mo yields. CuCo- samples resulted in low melting temperatures, even at high Co concentrations.

Table1. Powder Characterization of Co-precipitated bimetallic SOFC anode precursors.

Expected Sample Composition	Real Sample Composition (XRF)	Precursor Phases (XRD)	T_m (°C)
39Ni-16Cu	33Ni-23Cu	NiO, CuO	>1400
31Ni-24Cu	25Ni-33Cu	NiO, CuO	1350

23Ni-32Cu	18Ni-41Cu	NiO, CuO	1200
15Ni-40Cu	11Ni-47Cu	NiO, CuO	1200
7Ni-48Cu	6Ni-53Cu	NiO, CuO	1050
4Ni-51Cu	3Ni-57Cu	NiO, CuO	1050
31Ni-24Co	29Ni-24Co	NiO, Co_3O_4	>1400
23Ni-32Co	21Ni-32Co	NiO, Co_3O_4	>1400
15Ni-40Co	14Ni-32Co	NiO, Co_3O_4	>1400
7Ni-48Co	7Ni-47Co	NiO, Co_3O_4	>1400
4Ni-51Co	3Ni-50Co	NiO, Co_3O_4	>1400
51Cu-4Co	55Cu-4Co	CuO, Co_3O_4	1050
47Cu-8Co	51Cu-7Co	CuO, Co_3O_4	1050
40Cu-15Co	43Cu-15Co	CuO, Co_3O_4	1050
31Cu-24Co	34Cu-22Co	CuO, Co_3O_4	1100
23Cu-32Co	25Cu-30Co	CuO, Co_3O_4	1150
15Cu-40Co	16Cu-38Co	CuO, Co_3O_4	1350
7Cu-48Co	8Cu-46Co	CuO, Co_3O_4	1350
4Cu-51Co	not performed	CuO, Co_3O_4	1400
51Ni-4Mo	58Ni-1Mo	NiO	>1400
47Ni-8Mo	56Ni-2Mo	NiO	>1400
40Ni-15Mo	47Ni-8Mo	NiO, $NiMoO_4$	n/a
31Ni-24Mo	40Ni-11Mo	NiO, $YMoO_4$	n/a
23Ni-32Mo	31Ni-16Mo	NiO, $NiMoO_4$	n/a
15Ni-40Mo	22Ni-21Mo	NiO, $NiMoO_4$	n/a
7Ni-48Mo	14Ni-17Mo	NiO, $NiMoO_4$	n/a
4Ni-51Mo	7Ni-30Mo	$NiMoO_4$	n/a
51Cu-4Mo	59Cu-0Mo	CuO	1100
47Cu-8Mo	59Cu-0Mo	CuO	1100
40Cu-15Mo	56Cu-0Mo	CuO	1100
31Cu-24Mo	52Cu-0Mo	CuO	1200
23Cu-32Mo	46Cu-0Mo	CuO	>1400
15Cu-40Mo	39Cu-0Mo	CuO	>1400
7Cu-48Mo	25Cu-6Mo	CuO	>1400
4Cu-51Mo	14Cu-7Mo	CuO	>1400
51Co-4Mo	52Co-1Mo	Co_3O_4	>1400
47Co-8Mo	50Co-2Mo	Co_3O_4	>1400
40Co-15Mo	42Co-6Mo	Co_3O_4, $CoMoO_4$	>1400
31Co-24Mo	37Co-11Mo	Co_3O_4, $CoMoO_4$	>1400
23Co-32Mo	36Co-3Mo	Co_3O_4	>1400
15Co-40Mo	22Co-15Mo	Co_3O_4, $CoMoO_4$	1100

7Co-48Mo	10Co-28Mo	$CoMoO_4$, $YMoO_4$	Not completed
4Co-51Mo	6Co-32Mo	$CoMoO_4$, $YMoO_4$	1000